5-23-2016

Analysis and Control of Thermoacoustic Instability: A Time Delay Systems Approach

Umut Zalluhoglu
umut.zalluhoglu@uconn.edu

Analysis and Control of Thermoacoustic Instability: A Time Delay Systems Approach

Umut Zalluhoglu, Ph.D.

University of Connecticut, 2016

Thermoacoustic instability arises from the interaction between unsteady heat release and pressure perturbations in an acoustic enclosure. The pressure oscillations grow and lead to excessive stress reversals in the structure, raising fatigue concerns and mechanical failures. This common phenomenon in the realistic combustors and rocket engines has been broadly studied over a simplistic laboratory abstraction called the Rijke tube. This simple set-up offers a convenient platform to elucidate the fundamental physics of thermoacoustic instabilities. As evident from the most recent literature, there are numerous aspects of this phenomenon even in the Rijke tube setting that are not fully understood and explored. The current work addresses some of them by forming a bridge between thermoacoustics research and time delay systems stability theory.

Under certain conditions, this phenomenon can be modeled as a linear time-invariant dynamics which is affected by multiple time delays. Moreover it falls into the "neutral" time delay systems sub-class, stability analysis of which is notoriously challenging. In order to assess its stability, a recent mathematical paradigm called the Cluster Treatment of Characteristic Roots (CTCR) is used throughout this work. This combination forms the key contributions of this doctoral study, which are summarized as:

(i) Analytical prediction of thermoacoustic instability in Rijke tube in the parametric space of the system.

(ii) Introduction of a time-delayed integral controller. This approach leads to novel frontiers for feedback stabilization of thermoacoustic oscillations via a holistic analysis.

(iii) Parametric assessment of passive control of thermoacoustic instability using Helmholtz resonator. Specifically geometric characteristics are investigated to stabilize an unstable operation.

(iv) Introduction of active-passive stabilization methods, combining a Helmholtz resonator and a feedback loop over a Rijke tube. A new capability is developed to predict control-induced instabilities over this setting.

All of these analytically-discovered features are verified with experiments performed in the Advanced Laboratory for Automation, Robotics and Manufacturing. This unique approach is expected to improve the initial design efforts of real-world combustors.

Analysis and Control of Thermoacoustic Instability: A Time Delay Systems Approach

Umut Zalluhoglu

B.S., Middle East Technical University, 2012

A Dissertation

Submitted in Partial Fulfillment of the

Requirements for the Degree of

Doctor of Philosophy

at the

University of Connecticut

2016

APPROVAL PAGE

Doctor of Philosophy Dissertation

Analysis and Control of Thermoacoustic Instability: A Time Delay Systems Approach

Presented by

Umut Zalluhoglu, B.S.

Major Advisor _____
Nejat Olgac

Associate Advisor _____
Jiong Tang

Associate Advisor _____
Chengyu Cao

Associate Advisor _____
Xu Chen

University of Connecticut
2016

Acknowledgments

I believe completion of my doctorate degree has been one of the most beneficial undertakings in my life so far. Thus it is my great pleasure to thank people who have helped me throughout this journey. This achievement would not have happened without their motivation and support.

I would like to start with the best advisor I could have asked for, Professor Nejat Olgac, who welcomed me to the ALARM research group at UConn four years ago. Thank you for showing great faith and devoting incredible time of yours in me each and every day. Your exceptional support, guidance and encouragement have made this work exist. You have not only been a great academic advisor, but more importantly also a role model for me in life.

I am also thankful to the members of my advisory committee, Professors Jiong Tang, Chengyu Cao and Xu Chen, for their supervision and invaluable time through my entire Ph.D. journey.

I enjoyed each day at ALARM thanks to my colleagues Ayhan Kammer and Dr. Qingbin Gao. They have shared their knowledge and experience with me throughout my four years of stay at the laboratory, which is full of great memories. I would like to thank an ALARM alumnus, Dr. Rudy Cepeda-Gomez, for preparing informative introductory reports on thermoacoustics research prior to his graduation, which facilitated the outcome of this thesis. I also wish to thank Ayhan specifically for devoting a lot of his time to this work at its early stages. His valuable contributions have boosted the speed and productivity of this project.

Special thanks go to my parents Nihat and Candan Zalluhoglu and my brother Onurcan Zalluhoglu, for their motivational, emotional and financial support from overseas. Lastly but most importantly, I owe the completion of this work to a very special person, Fulya Sudur (and very recently) Zalluhoglu. Having my wife beside me has been the greatest encouragement for me to complete my doctorate degree.

Table of Contents

List of Figures

List of Tables

Chapter 1 Introduction

1.1 Background and Motivation

Thermoacoustics refers to the dynamic interaction between the variations in heat release and pressure. When heat is released into an acoustic enclosure, thermal and acoustic dynamics get coupled and can lead to *thermoacoustic instability*. Regionally confined heat release drives the acoustic waves which propagate within the enclosure and partially reflect from the boundaries [40]. As they arrive back at the heat source, they interact with the unsteady heat release disturbances again after some acoustic time delays. If the acoustic perturbations and the perturbations caused by the heat release synchronize, they grow in amplitude until limited by nonlinear effects. This is the key regenerative mechanism behind the thermoacoustic instabilities.

Thermoacoustic instabilities are often dangerous, since large fluctuations in pressure lead to excessive vibrations in the structure, raising fatigue concerns and mechanical failures. Solid and liquid propellant rocket engines [12], jet engines [10] and industrial gas turbines [6] are practical examples in which thermoacoustic instabilities are unwanted. On the other hand, some applications take advantage of these instabilities, such as thermoacoustic engines [66], ramjets and pulsed combustors [81], which inherently depend on the presence of sustained oscillations.

In order to suppress the damaging instabilities in the thermoacoustic systems, passive and active control techniques are sought. Both control methods aim to break the unstable coupling and are heavily used to abate the thermoacoustic oscillations in the industry [67]. The passive approach aims to add acoustic damping to the system in order to dissipate the energy, for instance, with the aid of Helmholtz resonators, acoustic liners and alike [79]. In active control, an external perturbation is introduced to the system via an actuator, which manipulates the acoustic field or the heat injection rate [14], [42]. If the control is closed-

loop, this external perturbation feeds some sensor measurements back to the system with a certain control law. In such feedback loops, loudspeakers and fuel valves are used as actuators, whereas microphones and photomultipliers are used as sensors.

More than one-and-a-half century before the industry experienced it, thermoacoustic instability was first observed by Higgins in 1777. He was able to generate a characteristic sound wave by placing a hydrogen diffusion flame into a tube [33]. Later in 1859, Rijke reported that he sustained a loud sound by inserting a flame heated wire of gauze in the lower half of an open-ended vertical glass tube [62]. Then he successfully repeated his experiments by replacing the gauze with an electrical heater. This experiment, the *Rijke tube*, became a canonical example for studying the thermoacoustic instability phenomenon [60].

In 1878, Rayleigh was the first to explain physically why self-excited oscillations occur in the Rijke tube and other thermoacoustic systems [40]:

"If heat be given to the air at the moment of greatest condensation, or be taken from it at the moment of greatest rarefaction, the vibration is encouraged. On the other hand, if heat be given at the moment of greatest rarefaction, or abstracted at the moment of greatest condensation, the vibration is discouraged."

His phenomenological criterion provides an insightful perspective to how thermoacoustic instability is driven. Nevertheless, without the crisp knowledge of dissipative components in the system, this criterion does not provide a necessary and sufficient condition for thermoacoustic instability. As the exact quantification of the dissipative effects is not straightforward and it depends on the system, a more elaborate systematic approach is required to predict and control the growing oscillations.

To enable a system-wide stability analysis, a mathematical representation of the system dynamics that carries the driving mechanisms behind the instabilities is required. However, practical complexities in modern-day combustors such as turbulence, diffusion flames and swirling flow prevent one from deriving a representative mathematical model. Therefore many researchers prefer to study simpler thermoacoustic

systems, such as a Rijke tube [19], [21], [31], [41], [43] to better understand the thermoacoustic instability phenomenon. As the consensus among these studies, following two remarks can be made:

Remark 1.1: Thermoacoustic instability starts with linear disturbances which grow rapidly until limited by nonlinear effects.

Remark 1.2: The analytical representation of the system entails inherent time delays due to acoustic wave propagation, thermal convection, etc.

The evolution of pressure oscillations during thermoacoustic instability is provided in Figure 1.1, which depicts the statement in Remark 1.1. The dynamics behave linearly at the onset of instabilities and the oscillations grow exponentially in amplitude [59]. At large amplitudes, when the nonlinear dynamics become dominant, limit cycle sets in. This evolution shows that linear stability analysis is essential to predict the onset of thermoacoustic instabilities.

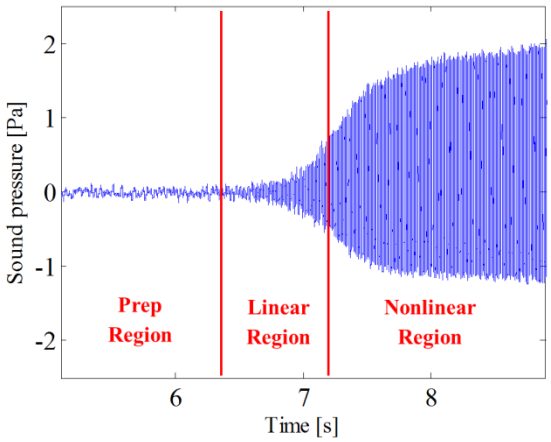

Figure 1.1 Evolution of pressure oscillations at the onset of thermoacoustic instability.

While Remark 1.1 points out the necessity of linear stability analysis to predict the onset of thermoacoustic instabilities, Remark 1.2 brings the infinite dimensional nature of time delay systems to the problem. In light of these two remarks, the mathematical model of Rijke tube dynamics under small

perturbations can be represented as a linear time-invariant multiple time delay system of neutral type (LTI-NMTDS) [13], [14], [45].

The regenerative time delay effect in LTI-NMTDS prevents one from using a vast variety of the linear stability analysis tools in the literature. This generally forces researchers to seek numerical and experimental approaches to predict and eliminate thermoacoustic instabilities [16], [46]. As far as the conventional linear stability analysis tools are concerned, Nyquist theorem is still applicable to such systems [13], [14], [38]; however it has two major limitations: First, it is applicable if all the system parameters are predetermined and fixed (i.e., it is a pointwise method). When the stability of the system is of question over broad range of operational parameters, pointwise methods consume a prohibitively high computational effort. Second, it is a geometric methodology and often yields obscurity as to the counts of encirclements around a particular point [14].

On the other hand, the systems and mathematics literature has strong evidence of an increasing intensity of research on delay differential equations and their stability [4], [47]. Various approaches have been developed over the past two decades in the time delay systems literature to address the stability of LTI-NMTDS [39], [61]. Among those, a unique paradigm stands out, which can perform stability analysis of such systems exhaustively and non-conservatively. This paradigm is called the Cluster Treatment of Characteristic Roots (CTCR) and has left its footprint in the scientific community over the last decade [49], [54].

1.2 Scope of the thesis

This dissertation constructs a bridge between two research topics: *thermoacoustic instability* and *time-delayed system mathematics*. The recent advances in the TDS stability have the potential to aid thermoacoustic instability research, but they have never been explored to date. The main aim of this work is to fill this gap by developing several analytical capabilities via the CTCR paradigm to address various

issues regarding thermoacoustic instability in Rijke tube. These capabilities are laid out in Chapters 3, 4, 5 and 6, which altogether form the main contributions of this study. Ultimately, the proposed theoretical findings are expected to aid the preliminary designs of thermal devices where thermoacoustic instability is a concern.

Specifically, Chapter 2 presents a brief review of the time-delayed system mathematics to prepare the reader for the following chapters. Two well-known theorems for stability of LTI-NMTDS are provided. Then, highlights of the CTCR paradigm are presented, which is frequently utilized in the following chapters to make an exact stability analysis over the infinite dimensional system dynamics.

Chapter 3 starts with the derivation of LTI-NMTDS representation of the Rijke tube dynamics. Then, an analytical mechanism is developed for prediction of thermoacoustic instability in the space of Rijke tube length and heater location. The analytical findings are verified via a series of experimental results from a laboratory scale Rijke tube.

Chapter 4 proposes an active control method for suppressing thermoacoustic instability. First, an infinite dimensional state-space representation of the feedback controlled Rijke tube dynamics is developed. Then, a feedback controller with time-delayed integral control logic is synthesized to stabilize an unstable operating Rijke tube. The controller is designed with a holistic analytical treatment via the CTCR paradigm. Moreover, the control performance is investigated over various controller parameter selections. All the analytical findings are compared with experimental results.

In Chapter 5, passive control of thermoacoustic instability is studied via a Helmholtz resonator. The Helmholtz resonator dynamics and its effect on the Rijke tube dynamics is presented first. A state space representation of the resonator mounted Rijke tube dynamics is derived. Then, a guideline to determine the placement of the resonator on the Rijke tube is proposed to stabilize the unstable thermoacoustic dynamics. These results are also verified with experimental findings.

In Chapter 6, control-induced instabilities caused by excitation of secondary dynamic modes are investigated. First, mathematical model of a Rijke tube with both a Helmholtz resonator and a feedback control loop is derived. On this complex infinite dimensional model, it is analytically shown that for high controller gain selections the secondary dynamic modes may rise to prominence although the initial unstable mode is suppressed. Experimental tests are conducted to verify the results of this analytical prediction mechanism.

Finally, some concluding remarks are made in Chapter 7 along with a brief discussion on the future research directions.

Chapter 2 Stability of Time Delay Systems

This chapter aims to prepare the reader to time delay system treatment that is followed in the rest of the chapters. Starting with an introduction to time delay systems in general, the focus later shifts to neutral type TDS that is of interest in the current work. The necessary tools to analyze the stability of such systems are introduced, which lead to the main contributions of this thesis.

Time delays have been used to model various practical engineering systems including combustors [13], machining processes [51], bladed rotors [55] and networks with communication delays [27]. Even if the delays are not inherently in the system dynamics, it is a common practice to introduce time delays in feedback control action to achieve various objectives, such as tuning active vibration absorbers [50] and designing control laws [27]. These have motivated an increasing intensity of research on time-delay systems in systems and mathematics literature throughout the last half-century [4], [30], [47].

Time delay systems (TDS) can be described by functional differential equations. Many of the aforementioned applications can be modeled as a subclass of TDS: linear time-invariant multiple time-delay system (LTI-MTDS). Such systems can be represented by a set of differential difference equations (DDEs) such as

$$\frac{d}{dt}\left(\mathbf{x}(t)-\sum_{k=1}^{m}\mathbf{A}_k\mathbf{x}(t-\tau_k)\right)=\mathbf{B}_0\mathbf{x}(t)+\sum_{k=1}^{m}\mathbf{B}_k\mathbf{x}(t-\tau_k) \tag{2.1}$$

where d/dt represents the time derivative, $\mathbf{x}(t)\in\Re^n$ is the state variable vector, $\mathbf{A}_k\in\Re^{n\times n}$, $\mathbf{B}_0\in\Re^{n\times n}$ and $\mathbf{B}_k\in\Re^{n\times n}$ are real matrices, $\boldsymbol{\tau}=(\tau_1,...,\tau_m)\in\Re^{m+}$ represents the time delay vector and m denotes the number of delays in $\boldsymbol{\tau}$.

If all $\mathbf{A}_k \in \Re^{n\times n}$, $k=1,2,...,m$ are zero matrices, then (2.1) is called an LTI-MTDS of *retarded* type. In retarded TDS, the derivative of the state variable, $\dot{\mathbf{x}}(t) \equiv d\,\mathbf{x}(t)/dt$, at time t depends only on the current and past values of the state variable [$\mathbf{x}(t)$ and $\mathbf{x}(t-\tau_k)$ respectively]. If there is a non-zero $\mathbf{A}_k \in \Re^{n\times n}$, $k=1,2,...,m$ matrix, however, (2.1) is called an LTI-MTDS of *neutral* type (or LTI-NMTDS). In neutral TDS, $\dot{\mathbf{x}}(t)$ at time t not only depends on $\mathbf{x}(t-\tau_k)$, but also on its derivative $\dot{\mathbf{x}}(t-\tau_k)$.

Regardless of its type (retarded or neutral), stability of LTI-MTDS in (2.1) is dictated by its characteristic equation,

$$CE(s,\boldsymbol{\tau}) = \det\left[s\left(\mathbf{I} - \sum_{k=1}^{m} \mathbf{A}_k \mathrm{e}^{-\tau_k s} \right) - \mathbf{B}_0 - \sum_{k=1}^{m} \mathbf{B}_k \mathrm{e}^{-\tau_k s} \right] = 0 \tag{2.2}$$

which brings about a quasi-polynomial that has infinitely many roots due to the transcendental terms $\mathrm{e}^{-\tau_k s}$. The distribution of the infinitely many roots of (2.2) over the complex plane $\mathbf{C}$ plays a key role in the stability characteristics of (2.1).

If (2.1) is of retarded type, a small variation in a parameter of (2.2) would yield only a small variation in the characteristic roots, which is known as the *root continuity argument* [49]. It is well known in the literature that this property does not hold for neutral TDS, since arbitrarily small changes may cause discontinuous movement of the characteristic roots over $\mathbf{C}$. This is essentially caused by the occurrence of so-called infinite root chains, sequences of roots whose imaginary parts grow unbounded, while their real parts have finite limit [44]. As the spectral properties differ in retarded and neutral type TDS, so does their stability characteristics.

As will be derived in the following chapters of this work, the mathematical model of thermoacoustic dynamics in Rijke tube falls into the LTI-NMTDS class. Therefore the focus will be on the stability analysis of neutral class TDS in the rest of the current work.

2.1 Neutral TDS Stability

The difference equation imbedded in the left hand side of the neutral DDE (2.1)

$$\mathbf{x}(t) - \sum_{k=1}^{m} \mathbf{A}_k \mathbf{x}(t - \tau_k) = 0 \tag{2.3}$$

is known as the associated difference equation (i.e., neutral operator) [29]. The distribution of the zeros of its characteristic quasi-polynomial

$$D(s, \boldsymbol{\tau}) = \det\left(\mathbf{I} - \sum_{k=1}^{m} \mathbf{A}_k \mathrm{e}^{-\tau_k s} \right) = 0 \tag{2.4}$$

over $\mathbf{C}$ is critical for the stability of the LTI-NMTDS in (2.1). Following these definitions two important theorems for the exponential stability of LTI-NMTDS are presented next from earlier mathematical studies, leaving the proofs to the cited references.

Theorem 2.1 [29]: The LTI-NMTDS (2.1) is exponentially stable if and only if all the roots of its characteristic equation (2.2) (i) lie in the left-half plane, $\mathbf{C}^-$ (ii) and are bounded away from the imaginary axis $\mathbf{C}^0$.

Remark 2.1 For neutral TDS, exponential stability implies asymptotic stability; however, the converse may not hold [68].

Theorem 2.2 [29]: The exponential stability of the neutral operator (2.3) is a necessary for the stability of the LTI-NMTDS (2.1). Accordingly, all the roots of characteristic equation associated with the neutral operator (2.4) should lie in the left-half plane, $\mathbf{C}^-$.

Corollary 2.1 [29]: Consider a neutral system with the following characteristic equation

$$1+\sum_{k=1}^{m} a_k e^{-\tau_k s} = 0 . \tag{2.5}$$

If $\tau_1,...,\tau_m$ are rationally independent and $a_1,...,a_m$ are scalar, (2.5) is exponentially stable if and only if

$$\sum_{k=1}^{m} |a_k| < 1 \tag{2.6}$$ ■

Remark 2.2 The condition (ii) in Theorem 2.1 can be guaranteed by the Theorem 2.2. Therefore Theorem 2.2 is a precondition to Theorem 2.1.

In light of Remark 2.2, if Theorem 2.2 is satisfied, the exponential stability of LTI-NMTDS (2.1) can be analyzed by checking condition (i) in Theorem 2.1. This can be achieved via various methods that exist in the TDS literature [47], [39], [61].

Several numerical routines are developed over the last two decades, which approximate the dominant characteristic roots of TDS for a specific set of delays. DDE-BIFTOOL [18], TRACE-DDE [7] and Quasi-Polynomial mapping-based Rootfinder (QPmR) [69] are among the well-known numerical tools. They declare the stability in a pointwise fashion only (i.e., for a fixed set of delays). This is the shortfall of these methods, that the computational demand becomes prohibitive very quickly. Lyapunov–Krasovskii approaches are also developed for the stability determination of TDS [28]. These methods, however, provide only conservative results and are strongly dependent on the particular selection of the Lyapunov-Krasovskii functionals.

The cluster treatment of characteristic roots (CTCR) paradigm emerges among the TDS stability analysis methodologies as a unique tool to remedy such shortfalls [49]. It can assess the stability of such systems in the broad space of system parameters (e.g., delays) exhaustively and non-conservatively. It is adopted as the main stability analysis tool in this work, and its highlights are explained in the next section.

2.2 Highlights of CTCR Paradigm

For an LTI-TDS represented by (2.1) the stability posture can be switched only if the roots of its characteristic polynomial (2.2) cross $\mathbf{C}^0$ (i.e., the imaginary axis), say at $s = \pm\omega\mathrm{i}$, $\omega \in \Re$, for some $\boldsymbol{\tau} = \bar{\boldsymbol{\tau}}$, $\bar{\boldsymbol{\tau}} \in \Re^{m+}$. When such a crossing occurs, the causal correspondence between $\bar{\boldsymbol{\tau}} \in \Re^{m+}$ and $\omega \in \Re$ is denoted by $\langle \bar{\boldsymbol{\tau}}, \omega \rangle$. To assess the stability of the system, all such $\langle \bar{\boldsymbol{\tau}}, \omega \rangle$ should be determined exhaustively. The complete set of corresponding imaginary root frequencies are represented by

$$\boldsymbol{\Omega} = \left\{ \omega \,\middle|\, CE(s = \pm\omega\mathrm{i}, \bar{\boldsymbol{\tau}}) = 0, \boldsymbol{\tau} \in \Re^{m+}, \omega \in \Re \right\} \tag{2.7}$$

and the root set with

$$\mathbf{S}_{\Omega} = \left\{ s = \pm\omega\mathrm{i} \,\middle|\, \omega \in \boldsymbol{\Omega} \right\} \tag{2.8}$$

It can be observed from (2.2) that, for any $\langle \bar{\boldsymbol{\tau}}, \omega \rangle$ correspondence, there exists infinitely many others that share the identical $\omega \in \boldsymbol{\Omega}$. They can be expressed as

$$\left\langle \bar{\boldsymbol{\tau}} + \mathbf{p}\frac{2\pi}{\omega},\ \omega \right\rangle, \quad \mathbf{p} = [p_1, ..., p_m] \in \mathbf{N}^m \tag{2.9}$$

where $\mathbf{N}$ denotes the natural numbers. Therefore, one can detect infinitely many hypersurfaces in $\boldsymbol{\tau} \in \Re^{m+}$ that share the same $\boldsymbol{\Omega}$ set. These hypersurfaces continuously partition the $\boldsymbol{\tau} \in \Re^{m+}$ domain into infinitely many encapsulated regions in which the *number of unstable roots* (*NU*) remains fixed. The stability assessment of (2.1) boils down to revealing the regions in which $NU = 0$. This complex formation of geometry can be overcome by grouping $\langle \bar{\boldsymbol{\tau}}, \omega \rangle$ correspondence into clusters, which brings us to the CTCR paradigm. The following two propositions establish a discipline to this chaotic looking picture, and form the skeleton of the CTCR paradigm.

Proposition 1 [64] There is only a manageably small number of hypersurfaces in $\boldsymbol{\tau} \in \Re^{m+}$ space which characterizes the complete set of $\boldsymbol{\Omega}$. They are called the *kernel hypersurfaces* and are denoted by

$$\wp_0 = \left\{ \bar{\boldsymbol{\tau}} \,\middle|\, \langle \bar{\boldsymbol{\tau}}, \omega \rangle,\ \bar{\boldsymbol{\tau}} \in \Re^{m+},\ \omega \in \boldsymbol{\Omega},\ 0 \le \tau_k \le \frac{2\pi}{\omega},\ k = 1, ..., m \right\} \tag{2.10}$$

■

Notice that $\wp_0$ represents the loci of the smallest $\bar{\boldsymbol{\tau}} \in \Re^{m+}$ combinations that satisfies the $\langle \bar{\boldsymbol{\tau}}, \omega \rangle$ correspondence. From each point on $\wp_0$ one can create infinitely many offspring points corresponding to $\mathbf{p} = [p_1, ..., p_m] \in \mathbf{N}^m$ in (2.9), where $\sum_{k=1}^{m} p_k > 0$. The loci of such points are called the offspring hypersurfaces and denoted by $\wp_{\mathbf{p}}$. The union of kernel and offspring hypersurfaces,

$$\wp = \wp_0 \cup \bigcup_{p_1=0}^{\infty} \bigcup_{p_2=0}^{\infty} \cdots \bigcup_{p_m=0}^{\infty} \wp_{\mathbf{p}} \qquad p_1 + p_2 + \ldots + p_k > 0 \tag{2.11}$$

constitutes the complete and exhaustive set of delay values $\bar{\boldsymbol{\tau}} \in \Re^{m+}$ in $\boldsymbol{\tau} \in \Re^{m+}$ space where (2.2) has at least a pair of imaginary roots $s = \pm \omega \mathrm{i}$.

In order to reveal the stable regions in $\boldsymbol{\tau} \in \Re^{m+}$, *NU* should be calculated in each region, so as one traverses through a hypersurface, the crossing direction of imaginary roots through $\mathbf{C}^0$ is needed. For this purpose the *root tendency* (*RT*) is defined for an imaginary characteristic root $s = \pm \omega \mathrm{i}$, along any one of the delay axes τ_k in $\bar{\boldsymbol{\tau}} \in \Re^{m+}$ as

$$RT\big|_{s=\omega \mathrm{i}}^{\tau_k} = \mathrm{sgn}\left[\mathrm{Re}\left(\frac{\partial s}{\partial \tau_k} \right)\Big|_{s=\omega \mathrm{i}} \right] \tag{2.12}$$

Proposition 2 [64] For $s \in \mathbf{S}_\Omega$, as any delay τ_k in $\bar{\boldsymbol{\tau}} \in \Re^{m+}$ on the kernel and on its corresponding offspring infinitesimally increases, the root tendency $RT\big|_{s=\omega i}^{\tau_k}$ remains invariant so long as the set of other delays $\{\bar{\boldsymbol{\tau}} - \tau_k\}$ are kept fixed. ■

The implementation of the CTCR paradigm starts with the determination of kernel hypersurfaces, $\wp_0$. There are various methodologies in the literature that serve this purpose, such as Rekasius substitution [64], Spectral Delay Space (SDS) [22], and Kronecker summation [20]. Then the offspring hypersurfaces, $\wp_{\mathbf{p}}$, can be obtained using the pointwise nonlinear transformation in (2.9). Using the complete set of hypersurfaces, $\wp$, one can partition $\boldsymbol{\tau} \in \Re^{m+}$ domain into regions in which NU remains unchanged. Proposition 2 then exhaustively declares NU for each region in $\boldsymbol{\tau} \in \Re^{m+}$. This effort results in the complete description of all stable regions in $\boldsymbol{\tau} \in \Re^{m+}$ where $NU = 0$. The resulting stability outlook is called as the *stability map* of the system.

Chapter 3 Prediction of Thermoacoustic Instability in Rijke Tube

Thermoacoustic instabilities in modern combustors motivated many researchers to develop a prediction capability for this undesired phenomenon [9]. However, due to the complex dynamics of the practical combustors, these attempts have been limited to experimental or computational approaches [10]. To better understand this phenomenon, many researchers focused on a simple thermoacoustic device called Rijke tube [21], [31], [41]. The injection of heat into the air within the Rijke tube resembles the injection of fuel to the upcoming air that causes combustion in the aero-engine's (similarly, in the gas turbine's) combustor chambers (see Figure 3.1a). The interaction of this heat release with the combustor or tube acoustics causes thermoacoustic instability in both systems.

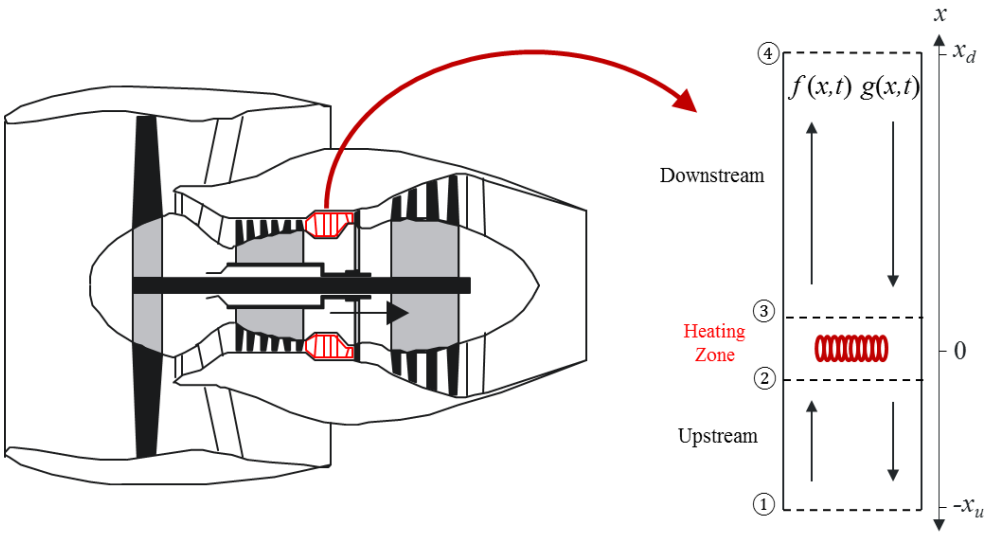

Figure 3.1 (a) Cross-sectional view of an aero-engine and its combustor, (b) depiction of Rijke tube and the acoustic waves therein.

As shown in Figure 3.1b a Rijke tube simply consists of an open-ended slender tube and a heating element [62]. The released heat at the heating zone drives pressure waves which propagate to both ends of the tube. The open ends of the tube act as acoustic walls that partially reflect the waves. Once the pressure waves arrive back at the heating zone after some transport delays, they meet the heat release again. This results in a regenerative dynamics, which, under certain circumstances, can cause self-excited oscillations in pressure and heat release. This chapter focuses on identifying the conditions that lead to these oscillations (i.e., thermoacoustic instability).

Different analytical tools are deployed for stability analysis of the Rijke tube [21], [42]. For instance, the effect of "non-normal" behavior on thermoacoustic interactions and its stability repercussions are considered in [2]. To study further on this concept, "non-modal" analysis tools are explored in [35], [63]. From a nonlinear systems perspective, some researchers also investigate bifurcation characteristics of thermoacoustic instability and make relevant stability assertions for the system [2], [65]. These pathways have two key commonalities:

(i) The acoustical modes, which bring the infinite-dimensional characteristics to the problem, are handled using Galerkin expansion. That introduces modal confinement due to the limited number of modes selected in the expansion.

(ii) The only pure time delay in the dynamics appears due to modified King's Law [32] at the heat release transfer function.

Another group of researchers proceed to linearize the governing physics of thermoacoustic dynamics and study the stability of the system under certain assumptions [21]. In [13], [14] thermoacoustic system model is reduced to a simpler form, where the underlying dynamics is linear time-invariant and it involves multiple independent time delays. The resulting time-delayed system is of neutral type, which is a mathematical feature that increases the complexity even further. This approach, which is followed throughout this work, preserves the infinite dimensional nature of the dynamics and therefore provides

more reliable results. This chapter deploys the CTCR paradigm on this LTI-NMTDS dynamics for analytical prediction of thermoacoustic instability and its experimental validation.

First, mathematical model of the Rijke tube dynamics is derived in LTI-NMTDS form. Then the operating conditions that result in thermoacoustic instability are analytically predicted using the CTCR paradigm. Finally, the analytical findings are verified with experimental results from a laboratory scale Rijke tube.

3.1 Rijke Tube Dynamics

The mathematical model constructed in this section carries the underpinning physics of the thermoacoustic dynamics in a Rijke tube. The depiction of the Rijke tube model is provided in Figure 3.1b. The dynamic model is inspired by earlier investigations in the literature [13], [14]. To start with, a series of common assumptions are applied:

(i) The airflow is induced by natural buoyancy, therefore has low velocity and negligibly small Mach number.

(ii) The flow is inviscid and air is considered as an ideal gas.

(iii) The heating zone is infinitesimally thin compared to the tube length.

(iv) The acoustic wave propagation is taken as a one-dimensional event.

(v) Except for the heating zone the flow is isentropic.

3.1.1 Acoustic dynamics

The acoustic dynamics in the absence of a heat source is governed by the first principles of conservation of mass, momentum and energy, which are nonlinear partial differential equations [9]

$$
\begin{aligned}
&-\textit{Conservation of Mass} && \frac{\partial \rho}{\partial t}+\frac{\partial(\rho u)}{\partial x}=0 \\
&-\textit{Conservation of Momentum} && \frac{\partial(\rho u)}{\partial t}+\frac{\partial(\rho u^2+p)}{\partial x}=0 \\
&-\textit{Conservation of Energy} && \frac{\partial(\rho E)}{\partial t}+\frac{\partial(\rho E u+p u)}{\partial x}=0
\end{aligned}
\tag{3.1}
$$

where ρ is density, u velocity and p pressure. $E=e+0.5u^2$ is the total energy, sum of internal and kinetic energy respectively. In (3.1), x and t denote the position along the tube and time. The ideal gas law and other property relations that assist the governing equations are

$$
p=\rho R_s T,\quad \frac{c_p}{c_v}=\gamma,\quad c_p-c_v=R_s,\quad c_p=\frac{\gamma}{\gamma-1}R_s,\quad e=c_v T \tag{3.2}
$$

where T is temperature, R_s is the specific gas constant, c_v and c_p denote the specific heat capacities at constant volume and pressure and γ is the heat capacity ratio. The nonlinear dynamics in (3.1) can be linearized under small perturbations by

$$
\psi(x,t)=\overline{\psi}(x)+\tilde{\psi}(x,t),\qquad \psi\in(\rho,u,p) \tag{3.3}
$$

where the variables describing the gas dynamics are separated into a stationary equilibrium field (denoted by $\bar{\bullet}$) and much smaller time-dependent perturbation (denoted by $\tilde{\bullet}$). Following linearization and algebraic manipulations of the conservation equations in (3.1), one obtains the convected wave equation [15]

$$
\frac{\partial^2 \tilde{p}}{\partial t^2}+(\bar{u}^2-\bar{c}^2)\frac{\partial^2 \tilde{p}}{\partial x^2}+2\bar{u}\frac{\partial^2 \tilde{p}}{\partial t\partial x}=0 \tag{3.4}
$$

where $\bar{c}$ is the speed of sound. Under the listed assumptions, considering $\bar{u}<<\bar{c}$, (3.4) can be simplified to the classical wave equation

$$\frac{\partial^2 \tilde{p}}{\partial t^2} - \bar{c}^2 \frac{\partial^2 \tilde{p}}{\partial x^2} = 0 \tag{3.5}$$

Following the d'Alembert's solution of the linear wave equation [14], the pressure fluctuations, $\tilde{p}(x,t)$, can be expressed as some superposition of the two linearly independent acoustic waves, $f(x,t)$ and $g(x,t)$, which travel along the tube in the downstream and upstream directions, respectively (see Figure 3.1b)

$$\tilde{p}(x,t) = f(t - x/\bar{c}_i) + g(t + x/\bar{c}_i)\ , \quad i = \begin{cases} u, & for\ -x_u < x < 0 \\ d, & for\ \ 0 < x < x_d \end{cases} \tag{3.6}$$

Substituting (3.6) in the linearized version of the momentum conservation equation in (3.1), the velocity fluctuations $\tilde{u}(x,t)$ can also be expressed in terms of $f(x,t)$ and $g(x,t)$ as

$$\tilde{u}(x,t) = [f(t - x/\bar{c}_i) - g(t + x/\bar{c}_i)]/\bar{\rho}_i \bar{c}_i\ , \quad i = \begin{cases} u, & for\ -x_u < x < 0 \\ d, & for\ \ 0 < x < x_d \end{cases} \tag{3.7}$$

A similar expression for the density fluctuations $\tilde{\rho}(x,t)$ can be obtained by substituting (3.6) in the property relations (3.2) as well. In both (3.6) and (3.7) the subscript $i = u, d$ represents the upstream and downstream sides of the heater. Notice that in Figure 3.1b, the heat release takes place at $x = 0$ and x_u, x_d denote the upstream and downstream distances between ①-② and ③-④ respectively.

In Figure 3.2a, acoustic waves are represented by $f_i(t) = f(x_i, t)$ and $g_i(t) = g(x_i, t)$, with the subscripts $i = 1,\ldots, 4$ denoting the locations where these functions are evaluated. This notational twist leads to a block diagram representation of the Rijke tube as shown in Figure 3.2b. In Figure 3.2b, $F_i(s)$ and $G_i(s)$, are the Laplace transforms of the corresponding wave expressions.

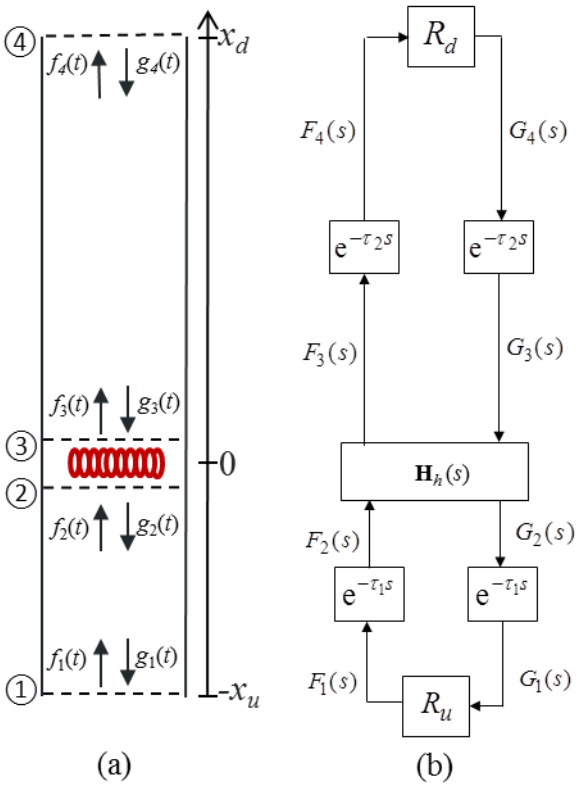

Figure 3.2 (a) Functional sketch of a Rijke tube, (b) its block diagram representation.

3.1.2 Thermoacoustic interaction at the heating zone

The thermoacoustic coupling at the heat release zone can be derived by taking a control volume between the cross-sections ② and ③. With the assumption that this zone is infinitesimally thin (narrow), the conservation equations in (3.1) can be rewritten as jump conditions at this control volume, but with the addition of the heat source term to the energy equation. When they are combined with the property relations in (3.2), the following reduced set of equations can be obtained [13]

$$\begin{aligned} p_3 - p_2 + \rho_2 u_2 (u_3 - u_2) &= 0 \\ \frac{\gamma}{\gamma - 1}(p_3 u_3 - p_2 u_2) + \frac{1}{2}\rho_2 u_2 (u_3^2 - u_2^2) &= \frac{Q}{A} \end{aligned} \tag{3.8}$$

where Q is the heat release rate and A is the cross-sectional area at the heat release zone. Upon linearization of (3.8) and substitution of (3.6) and (3.7) in the equation set, one reaches

$$\mathbf{Z}_1\begin{pmatrix} g_2(t) \\ f_3(t) \end{pmatrix} = \mathbf{Z}_2\begin{pmatrix} f_2(t) \\ g_3(t) \end{pmatrix} + \begin{pmatrix} 0 \\ \tilde{Q}(t)/A\bar{c}_u \end{pmatrix} \tag{3.9}$$

where $\tilde{Q}(t)$ is the fluctuations in the heat release rate. $\mathbf{Z}_1$ and $\mathbf{Z}_2$ are constant matrices given by

$$\mathbf{Z}_1 = \begin{bmatrix} -1+\overline{M}_2\left(2-\dfrac{\bar{u}_3}{\bar{u}_2}\right)-\overline{M}_2^2\left(1-\dfrac{\bar{u}_3}{\bar{u}_2}\right) & 1+\overline{M}_2\dfrac{\bar{\rho}_u\bar{c}_u}{\bar{\rho}_d\bar{c}_d} \\ \overline{M}_2^2-\dfrac{\overline{M}_2^2\left(1-\overline{M}_2\right)\left(\dfrac{\bar{u}_3^2}{\bar{u}_2^2}-1\right)}{2}+\dfrac{1-\gamma\overline{M}_2}{\gamma-1} & \overline{M}_2\overline{M}_3\dfrac{\bar{\rho}_u}{\bar{\rho}_d}+\dfrac{\bar{c}_d}{\bar{c}_u}\dfrac{1+\gamma\overline{M}_3}{\gamma-1} \end{bmatrix} \tag{3.10}$$

$$\mathbf{Z}_2 = \begin{bmatrix} 1+\overline{M}_2\left(2-\dfrac{\bar{u}_3}{\bar{u}_2}\right)+\overline{M}_2^2\left(1-\dfrac{\bar{u}_3}{\bar{u}_2}\right) & -1+\overline{M}_2\dfrac{\bar{\rho}_u\bar{c}_u}{\bar{\rho}_d\bar{c}_d} \\ \overline{M}_2^2-\dfrac{\overline{M}_2^2\left(1+\overline{M}_2\right)\left(\dfrac{\bar{u}_3^2}{\bar{u}_2^2}-1\right)}{2}+\dfrac{1+\gamma\overline{M}_2}{\gamma-1} & \overline{M}_2\overline{M}_3\dfrac{\bar{\rho}_u}{\bar{\rho}_d}+\dfrac{\bar{c}_d}{\bar{c}_u}\dfrac{1-\gamma\overline{M}_3}{\gamma-1} \end{bmatrix} \tag{3.11}$$

In (3.10) and (3.11), $\overline{M}_2=\bar{u}_2/\bar{c}_u$ and $\overline{M}_3=\bar{u}_3/\bar{c}_d$ denote the Mach numbers. As noted in the listed assumptions, when $\bar{u} << \bar{c}$ both become negligibly small. Following this simplification, the thermoacoustic interaction represented by (3.9) can be written in Laplace domain as follows

$$\mathbf{Z}_1\begin{pmatrix} G_2(s) \\ F_3(s) \end{pmatrix} = \mathbf{Z}_2\begin{pmatrix} F_2(s) \\ G_3(s) \end{pmatrix} + \begin{pmatrix} 0 \\ \tilde{Q}(s)/A\bar{c}_u \end{pmatrix}, \quad \mathbf{Z}_1 = \begin{pmatrix} -1 & 1 \\ \dfrac{1}{\gamma-1} & \dfrac{\bar{c}_d}{\bar{c}_u}\dfrac{1}{\gamma-1} \end{pmatrix}, \ \mathbf{Z}_2 = \begin{pmatrix} 1 & -1 \\ \dfrac{1}{\gamma-1} & \dfrac{\bar{c}_d}{\bar{c}_u}\dfrac{1}{\gamma-1} \end{pmatrix} \tag{3.12}$$

The unsteady heat release $\tilde{Q}(t)$ is causally influenced by the velocity fluctuations just at the upstream of the heating zone, $\tilde{u}_2(t)$. This relation is commonly called as the 'flame transfer function' and represented by

$$\tilde{Q}(s)/\tilde{U}_2(s) = \phi(s) \tag{3.13}$$

in the Laplace domain. The true nature of $\phi(s)$ highly depends on the geometry and characteristics of the heat source [9]. Following many earlier investigations [23], [26], $\phi(s)$ is taken as a first order transfer function

$$\phi(s) = a/(bs+1) \tag{3.14}$$

where a is the gain of the transfer function proportional to the mean heat release rate $\overline{Q}(t)$, and b is the time constant acting as a pseudo-delay, which is affected by the geometric characteristics of the heater. For instance, [13] claims that the time constant b is a function of the radius and blockage ratio of the flame holder, if the heat source is a flame. In the case of an electrical-wire heater, on the other hand, [26] suggests a strong dependence of b on wire diameter at low frequencies. First-order dynamics approximation has shown to have reasonable agreement with response of a laminar flame in [23]. For more complex heat-release dynamics, higher-order flame transfer functions are also considered, including some time delays [13]. The general treatment here is completely transparent to the order of the complexity in the flame transfer function.

From (3.7), one can write $\tilde{U}_2(s) = \left[F_2(s) - G_2(s)\right]/\overline{\rho}_u \overline{c}_u$ in Laplace domain. Combining this expression with (3.12), (3.13) and (3.14) yields

$$\mathbf{Z}_1 \begin{pmatrix} G_2(s) \\ F_3(s) \end{pmatrix} = \mathbf{Z}_2 \begin{pmatrix} F_2(s) \\ G_3(s) \end{pmatrix} + \mathbf{J} \begin{pmatrix} F_2(s) \\ G_3(s) \end{pmatrix} - \mathbf{J} \begin{pmatrix} G_2(s) \\ F_3(s) \end{pmatrix}, \qquad \mathbf{J} = \begin{pmatrix} 0 & 0 \\ \dfrac{a/Ab\overline{\rho}_u \overline{c}_u{}^2}{s+1/b} & 0 \end{pmatrix} \tag{3.15}$$

Introducing two new operational matrices $\hat{\mathbf{Z}}_1 = \mathbf{Z}_1 + \mathbf{J}$ and $\hat{\mathbf{Z}}_2 = \mathbf{Z}_2 + \mathbf{J}$, one can restate (3.15) as

$$\begin{pmatrix} G_2(s) \\ F_3(s) \end{pmatrix} = \mathbf{H}_h \begin{pmatrix} F_2(s) \\ G_3(s) \end{pmatrix}, \qquad \mathbf{H}_h = \hat{\mathbf{Z}}_1{}^{-1} \hat{\mathbf{Z}}_2 \tag{3.16}$$

where $\mathbf{H}_h$ is the transfer matrix relating $[F_2(s) \quad G_3(s)]^{\mathrm{T}}$ to $[G_2(s) \quad F_3(s)]^{\mathrm{T}}$ in Figure 3.2b.

3.1.3 Boundary conditions and acoustic transport delays

The boundary conditions at cross-sections ① and ④ can be characterized by the reflection coefficients R_u and R_d as

$$f_1(t) = R_u g_1(t), \quad g_4(t) = R_d f_4(t) \tag{3.17}$$

If ideal reflection is assumed at the tube ends both coefficients should be -1. In reality; however, the acoustic waves partially reflect from the open ends due to radiation losses. The amplitude of the reflection coefficients therefore take values close to but less than 1.

The acoustic transport delays, $\tau_1 = x_u / \bar{c}_u$ and $\tau_2 = x_d / \bar{c}_d$, connect the acoustic waves at different cross-sections as shown in Figure 3.2b. Utilizing these delays and the reflection coefficients in (3.17), one can write

$$f_2(t) = R_u g_2(t - 2\tau_1), \quad g_3(t) = R_d f_3(t - 2\tau_2) \tag{3.18}$$

This leads to the following relation in Laplace domain

$$\begin{pmatrix} F_2(s) \\ G_3(s) \end{pmatrix} = \mathbf{R} \begin{pmatrix} G_2(s) \\ F_3(s) \end{pmatrix}, \qquad \mathbf{R} = \begin{bmatrix} R_u \mathrm{e}^{-2\tau_1 s} & 0 \\ 0 & R_d \mathrm{e}^{-2\tau_2 s} \end{bmatrix} \tag{3.19}$$

3.1.4 Complete Rijke tube model

The overall Rijke tube dynamics can be obtained by combining (3.16) and (3.19) as

$$\begin{pmatrix} G_2(s) \\ F_3(s) \end{pmatrix} = \mathbf{H}_h \mathbf{R} \begin{pmatrix} G_2(s) \\ F_3(s) \end{pmatrix} \tag{3.20}$$

which results in

$$\mathbf{M}\begin{pmatrix} G_2(s) \\ F_3(s) \end{pmatrix} = 0, \quad \mathbf{M} = \mathbf{I}_2 - \mathbf{H}_h\mathbf{R} \tag{3.21}$$

where $\mathbf{I}_2$ is 2×2 identity matrix and $\mathbf{M}$ represents the entire system matrix. Equation (3.21) presents a classical eigenvalue problem and $\mathbf{M}$ leads to a determinant which forms the characteristic equation of the system

$$CE(s,\tau_1,\tau_2) = \det(\mathbf{M}) = 0 \tag{3.22}$$

This is a quasi-polynomial equation involving two independent time delays, which are represented by τ_1 and τ_2. The dynamics represented by the characteristic polynomial in (3.22) falls into the LTI-NMTDS class.

3.2 Prediction of Instability and Its Experimental Validation

A laboratory set-up of a Rijke tube, which is constructed at the University of Connecticut – Advanced Laboratory for Automation, Robotics and Manufacturing (ALARM), is considered as the experimental platform. A picture of the test site is given in Figure 3.3 with the description of the components in Table 3.1. Its simplified mathematical model and the respective characteristic equation are generated first. A stability chart is constructed analytically using the CTCR paradigm on this system, next. Then a series of experiments are conducted on the set-up to validate the analytical predictions.

Several glass tube lengths are tested. An electrical heating element (a Nichrome wire coil wrapped around a mica skeleton) is used as the heat source. The power is delivered into the coil using a variac. The location of the electrical heating element is manually altered via a positioning cord. To measure the amount of power delivered to the electrical resistance, a wattmeter is used.

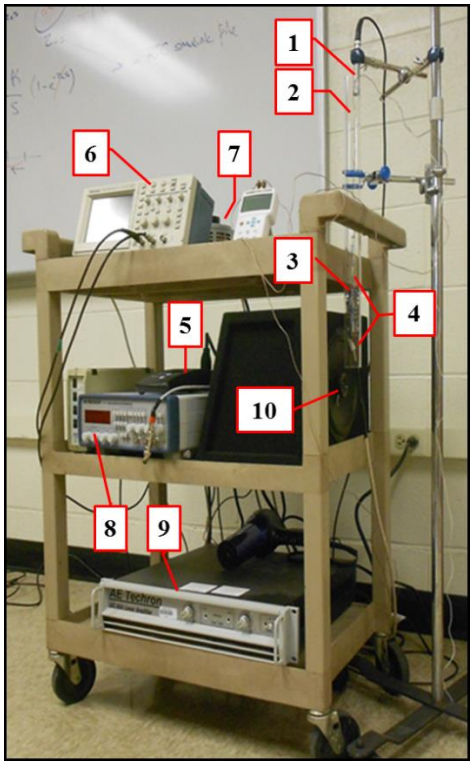

Figure 3.3 Picture of the experimental set-up.

Table 3.1 Components of the experimental set-up.

#	Instrument name	Details
1	Piezo-microphone	PCB Piezotronics Model 378B02
2	Glass tubes	3.1 cm dia., 2.1 mm thick., 50.8, 101.6 and 121.9 cm length
3	Nichrome heating element	23 Ω
4	Thermocouples	Omega 5SC-GG-K-30-100
5	Watt meter	Wattsup PRO ES
6	Digital oscilloscope	Tektronix TDS 210
7	Variac	Staco Energy Model 3PN1010B
8	Signal generator	BK Precision 4017A
9	Linear amplifier	AE Techron LVC 608
10	Loudspeaker	New Wave Audio 40 Hz – 22 kHz range

Two thermocouples are located at two ends of the heating element to monitor the temperature difference. The pressure fluctuations at the downstream end are recorded using a microphone. Furthermore, to obtain frequency response characteristics of the system, a loudspeaker (located below the tube) is used to generate sound pressure excitation.

Table 3.2 Operational parameters.

Parameter	Value	Unit
R_u	-0.93	-
R_d	-0.93	-
$\overline{Q}$	120	W
$\bar{c}_u$	340	m/s
$\bar{u}_1$	0.3	m/s
$\bar{\rho}_u$	1.2	kg/m^3
γ	1.4	-
A	0.00075	m^2
a	200	-
b	0.002	-

Several groups of experiments are performed on this set-up to extract various features of the thermoacoustic instability phenomenon. A common occurrence in all these tests is that for a given electrical power input to the heating element, a certain temperature differential between the two ends of the heater is created. This triggers natural buoyancy in the tube and thermoacoustic coupling starts. When it is unstable, an exaggerated sound pressure fluctuation is detected which is also audible as a loud humming sound. This happens only for certain placements of the heating element and does not happen for others. Next how these locations can be predicted analytically is shown.

Three sets of experiments are performed:

(i) Validation of the analytically-predicted stable and unstable operating points (generated by the CTCR paradigm) for various tube lengths and heater locations.

(ii) Comparison of the experimentally-extracted modal characteristics of the Rijke tube and those determined from the mathematical model.

(iii) Comparison of the frequency response characteristics from experiments and from the mathematical model.

3.2.1 Validation of the analytically-predicted stability map

It is recognized in the literature that speed of sound does not show a discernible variance between the two ends of the heating zone and this feature has little effect on the outcome of thermoacoustic instability [31]. With this additional assumption $(\bar{c}_u = \bar{c}_d)$, and the operational parameters listed in Table 3.2, the characteristic equation (3.22) becomes

$$\begin{aligned} CE(s,\tau_1,\tau_2) &= (1-0.865\mathrm{e}^{-2(\tau_1+\tau_2)s})\,s + 178.78\,\mathrm{e}^{-2\tau_1 s} \\ &-178.78\,\mathrm{e}^{-2\tau_2 s} - 598.71\mathrm{e}^{-2(\tau_1+\tau_2)s} + 692.23 = 0 \end{aligned} \tag{3.23}$$

In order to analyze stability of (3.23), first Theorem 2.2 should be checked. The coefficient of the highest order *s* term in (3.23) corresponds to the associated difference equation:

$$D(s,\tau_1,\tau_2) = 1 - 0.865\mathrm{e}^{-2(\tau_1+\tau_2)s} = 0 \tag{3.24}$$

which implies $|\mathrm{e}^{-2(\tau_1+\tau_2)s}| = 1.156 > 1$, meaning that all the infinitely many roots of (3.24) have $\mathrm{Re}(s) < 0$. Thus, the neutral operator in (3.24) is stable. Next, the stability map of the system with characteristic equation (3.23) is generated in Figure 3.4 by following the CTCR methodology. To facilitate visualization, the axes are transposed from (τ_1,τ_2) to $(x_u,x_d) = \bar{c}_u(\tau_1,\tau_2)$ in the figure, which are upstream and downstream distances from the heater to the tube ends. Various tube lengths are marked as 50.8, 101.6 and 121.9 centimeters corresponding to black parallel lines (represented by $x_u + x_d = \text{constant}$) on the stability map in Figure 3.4. The kernel hypercurve (red) and the offspring

hypercurves (blue) together constitute the complete set of potential stability switching boundaries. The shaded region denotes the (x_u, x_d) compositions, or the Rijke tube geometries for which the thermo-acoustic coupling is stable. In other words, all characteristic roots of (3.23) remain on the left half complex plane.

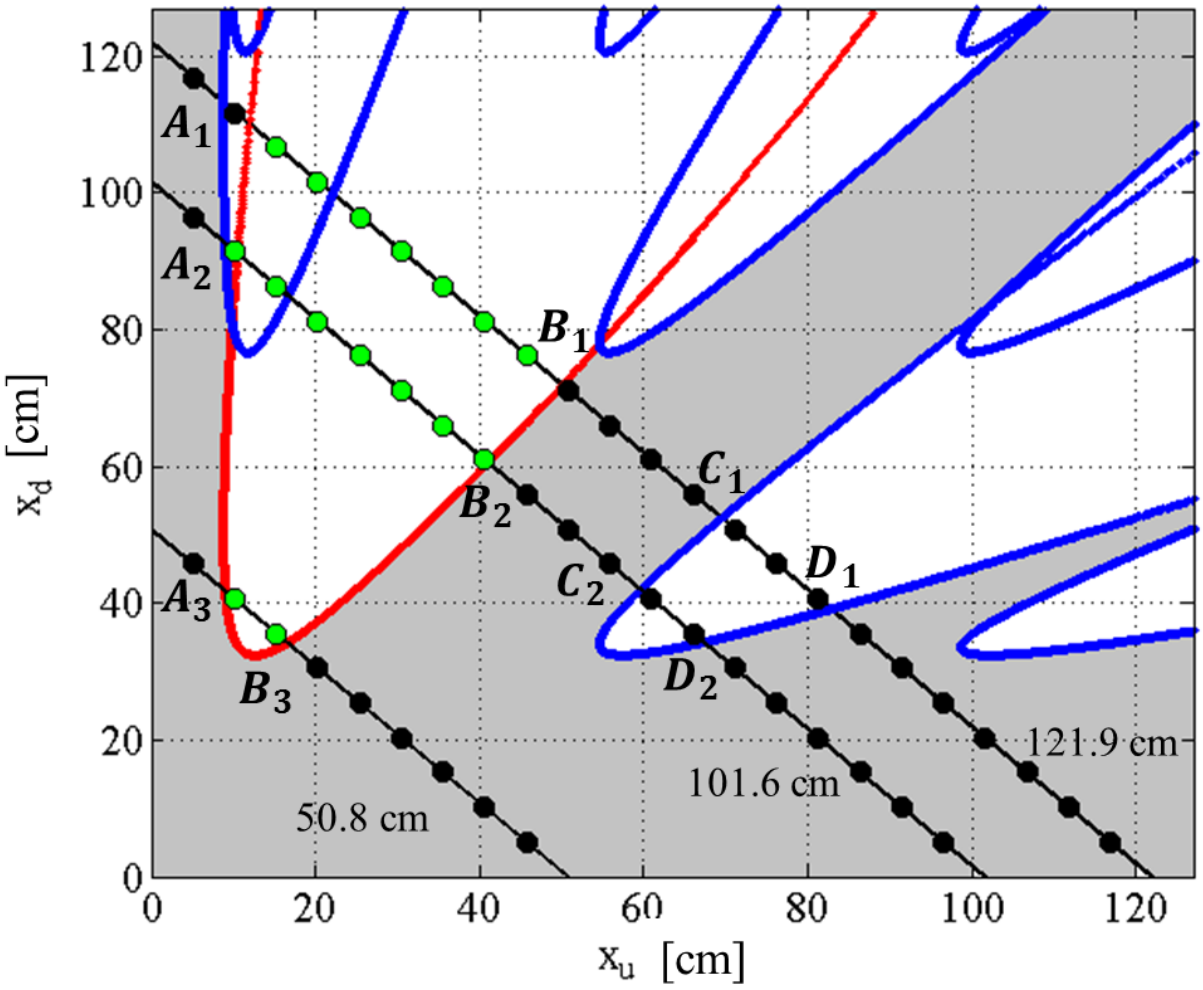

Figure 3.4 CTCR generated stability map for different tube lengths.

For the experimental validation of this stability map, the position of the heating element is changed manually and the ensuing sound pressure at the downstream end of the tube is monitored and recorded.

When the sound pressure fluctuations grow beyond a certain level, the onset of thermoacoustic instability is declared. This transition is observed as follows:

(a) The air temperature difference ΔT between the two sides of the heater builds up (from about 20 °C, to about 100-110 °C). For each repositioning of the heater the test is paused until the medium cools down to the starting value of about $\Delta T \cong 20\,°\mathrm{C}$. Then the heating element is energized and the amplitude of the pressure fluctuations Δp is monitored to increase.

(b) Until ΔT is built-up to a sufficient level to trigger the regenerative mechanism, Δp remains small, and then either stable or unstable dynamics follows. If ΔT increases significantly, but Δp remains very small with respect to background noise, the operation is declared stable. Such stable test points are marked with ● black in Figure 3.4.

(c) If the dynamics is unstable, on the other hand, ΔT again builds up to 100-110 °C, but this time the growth is also noticeable in Δp. These unstable test points are marked with ● green in Figure 3.4. Three different phases in the evolution of the sound pressure are noticed for an unstable test point:

  (c.1) Initial phase of ΔT build-up (no noticeable increase in Δp yet), which is the same behavior as in (a) above.

  (c.2) After ΔT reaches a certain level, an exponential growth in Δp takes place. This is an indicator that the regeneration mechanism is taking place with sufficient strength to trigger instability.

  (c.3) Steady ΔT and saturated pressure fluctuations Δp. This is a typical indication of nonlinearity dominating the dynamics, ultimately bringing nonlinear dissipative elements into action to force saturated pressure fluctuations in a limit cycle.

The tests are repeated for 50.8, 101.6 and 121.9 cm tube lengths. The correspondence between the experimental thermoacoustic instability detection overlaid on the analytically obtained stability chart of CTCR (Figure 3.4) is remarkable. A few minor disagreements are noticed: (*a*) Close to a stability border,

for instance near point A_1 for 121.9 cm tube length. Such discrepancies close to the theoretical stability boundaries are attributed to modeling deficiencies and are commonly encountered in occasions where complex physical phenomena are mathematically represented. (*b*) Missing segment of instability at C_1D_1 (for 121.9 cm tube) and C_2D_2 (for 101.6 cm) intervals. The expected but unobserved instability at these segments correspond to heater locations in the upper half of the tube. It is also reported in the literature [41], [60] that the instability of the Rijke tube at such locations is created by the higher modes of the dynamics, rather than the fundamental (1st) mode. In contrast to the almost complete concurrence in the lower half of the tube ($x_u < x_d$), the mismatch in the upper half ($x_u > x_d$) can be explained by the lack of nonlinear damping features in our mathematical model. For instance, [41] reports frequency dependence in acoustic reflection coefficients which invite nonlinearities allegedly forcing losses at higher levels than foreseen in our model in higher modes. Such discrepancies are again a natural consequence of using simplified models of complex dynamics which provide the only forum for effective analytical solutions.

The reported literature [41], our experiments and analytical predictions in Figure 3.4 have complete agreement in that it is not possible to destabilize any length of tube when the heat source is in the vicinity of the midpoint of the tube ($x_u = x_d$) and when it is very close to the open ends.

Referring to the discussions on the CTCR paradigm in Chapter 2, an important point to remember is that corresponding imaginary axis crossings $s = \pm\omega \mathrm{i}$ are declared in addition to the geometric compositions (x_u, x_d) at the stability boundaries in Figure 3.4. They correspond to the frequencies of resonance. These frequencies are displayed in Figure 3.5 for 50.8 cm and 101.6 cm tube lengths, additionally color-coded on the kernel hypercurve.

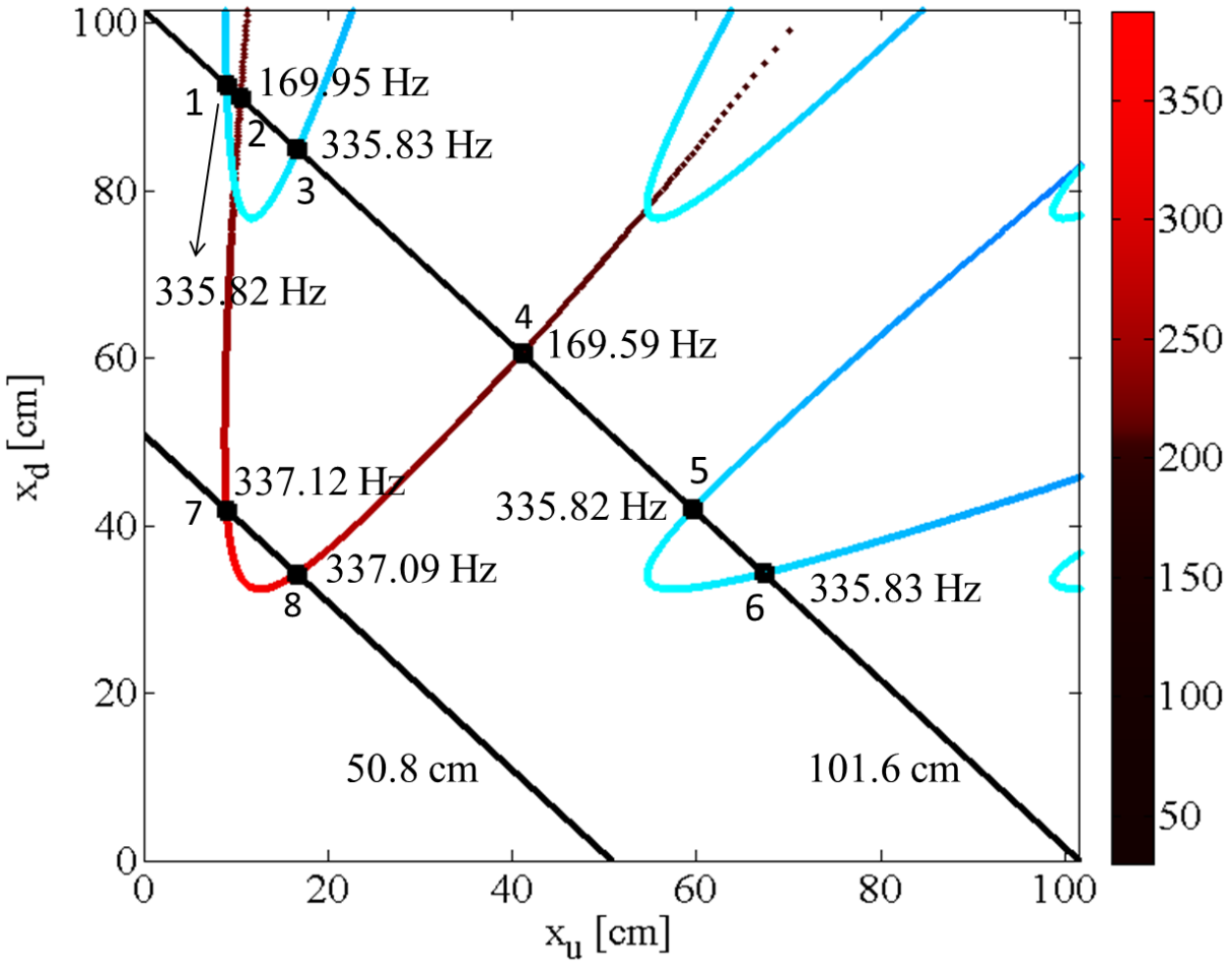

Figure 3.5 Frequency information on the CTCR-generated stability map.

Some further observations can be reported along this line. Considering the 101.6 cm-long tube, points 2 and 4 on the kernel are close to 169 Hz, whereas points 1, 3, 5 and 6 on the offspring are around 335 Hz. It is interesting to observe that these frequencies are very close to the first and second acoustic modes of the 101.6 cm long tube, which are calculated as $\omega_1 = \bar{c}/2L = 167.32\,\text{Hz}$ and $\omega_2 = 2\omega_1 = 334.64$ Hz. Similar features are observed for the 50.8 cm long tube. At points 7 and 8 the frequencies 337.12 Hz and 337.09 Hz are noticeably close to the 1st acoustic mode of this tube, (334.64 Hz). These observations imply the dominance of acoustic influence on the thermoacoustic instability phenomenon over thermal

effects for this experiment. In other words, the frequencies at the stability boundaries are primarily dictated by the acoustic modes of the tube, but slightly modulated by the thermal effects.

3.2.2 Comparison of modal characteristics at the onset of instability

At the heater locations where instability occurs, it is observed that the pressure fluctuations grow in amplitude. A typical sound pressure evolution was already shown in Figure 1.1 from experiments (on a 121.9 cm tube at x_u = 30.5 cm). Earlier mentioned phases of this transition (c.1, c.2, c.3) are distinctly marked on this figure. During the onset of instability (in the middle interval) the exponential growth of Δp is visible. This implies that when the amplitudes of the oscillations are small, the system behaves like a linear system, as exponential growth is reflective of a linear property. This feature is also recognized in the literature (e.g. [5] and [59]). When the Δp amplitude grows beyond the bounds of linearity, however, the small fluctuation assumption does not hold anymore for the dynamic models and the behavior moves into nonlinear domain. Many nonlinear dissipative mechanisms may appear after this stage, which were unaccounted for in the mathematical model. System behavior grows into a limit cycle with relatively steady Δp oscillations. This is visible in the last phase (nonlinear region) of Figure 1.1. These observations agree with the notion that the inception of thermoacoustic instability occurs in linear sense. For the prediction of instability linearized dynamic representation would be sufficient, and earlier discussed preconditions, rules and propositions of CTCR hold.

Another test to verify the analytical predictions with the experiments is to compare the spectral characteristics of the unstable transitions. In order to achieve this, two operating points are selected where thermoacoustic instability is expected on the stability map in Figure 3.4. Pressure fluctuations are recorded during the linear unstable growth phase for the corresponding Rijke tube settings (i.e., the tube length and heater location) with the microphone at the downstream end. Then a fast Fourier transformation (FFT) is performed on the sound pressure recording to determine the spectral distribution

of energy. The detected frequencies are then compared with the numerically-determined frequencies from the linear model. The root locations of the characteristic quasi-polynomial are found using a mathematical procedure called Quasi-Polynomial Mapping based Root-finder (QPmR) [69]. QPmR is an approximate root finding routine which declares as many characteristic roots of quasi-polynomial in (3.23) as desired, with a selected level of precision. A relative error tolerance of 10^{-6} is used in this study.

For the 121.9-cm-long tube the test results as well as the characteristic root distributions are presented in Figure 3.6 and Figure 3.7 when the heating element is at x_u = 20.3 cm and 40.6 cm, respectively. All FFT analyses here are performed with a frequency resolution of 1.25 Hz.

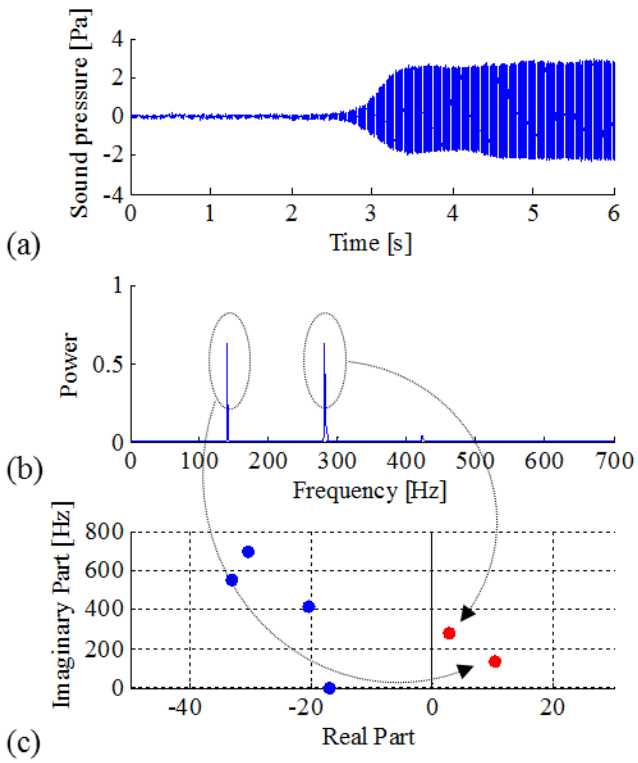

Figure 3.6 (a) Sound pressure fluctuation data, (b) power spectral density and (c) respective QPmR-generated dominant poles at (x_u, x_d) = (20.3, 101.6) cm.

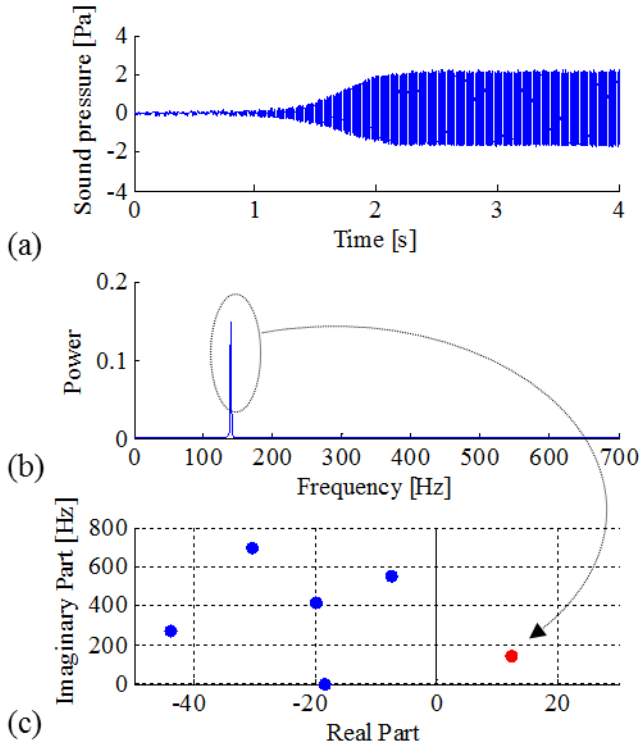

Figure 3.7 (a) Sound pressure fluctuation data, (b) power spectral density and (c) respective QPmR-generated dominant poles at (x_u, x_d) = (40.6, 81.3) cm.

Table 3.3 Experimental vs. predicted frequencies in Figure 3.6 and Figure 3.7.

x_u	Experimental	QPMR	Error %
20.3 cm	141.3 Hz	143.3 Hz	1.42
	282.5 Hz	280.3 Hz	0.78
40.6 cm	140.0 Hz	143.4 Hz	2.43

The unstable roots are marked with red in panes (c) and their imaginary parts (which correspond to the frequencies of the respective modes) agree very well with the experimentally obtained frequencies (see Table 3.3). It is a clear indication that the linearized model is indeed a valid representation of the Rijke tube behavior in the linear region (even for the unstable structure).

3.2.3 Frequency response tests

The objective in this group of tests is to investigate sensitive frequencies of the Rijke tube. These frequencies are extracted from frequency response-based experiments. They are then compared with the dominant root frequencies obtained from the mathematical model. The entire set of experiments in this section requires the Rijke tube to operate in stable mode, as the frequency response of an unstable system would be scientifically inconclusive. Similar to the previous section, QPmR is used to obtain the dominant roots, imaginary parts of which declare the approximate sensitive frequencies.

For this purpose the Rijke tube is excited using a loudspeaker at the upstream end with monotonically increasing frequencies at a sweep rate of 40 Hz/sec. All the dominant modes are expected to be observed in the form of exaggerated Δp amplitudes, as the excitation frequency is swept. The heating element location along the 121.9-cm long tube is adjusted to four distinct settings for this purpose (x_u = 10.2 cm, 50.8 cm, 76.2 cm and 86.4 cm). For each of these four settings, the heating element is powered and the resulting downstream pressure fluctuations are recorded. In the absence of the loudspeaker, even when the temperature differential across the heating element exceeds the earlier discussed threshold value, a discernible increase in Δp does not appear, because the system is stable. However when these stable dynamics are harmonically excited at single tone but sweeping frequencies, the sound pressure fluctuation at the downstream end of the tube starts to display high sensitivities at certain excitation frequencies. Those high-sensitivity points are captured with this set of experiments and are then compared with their analytical predictions.

The data acquisition is performed at 8000 Hz sampling rate through a dSpace DS1103 MicroAutoBox. The frequency sweeping operation is carried out in the range of 100-1100 Hz with a total duration of 25 seconds (40 Hz/sec sweep rate). The recorded data is processed off-line using their FFT on varying data segments with a shifting window of 300 msec length. This window length provides a frequency resolution of 3.33 Hz.

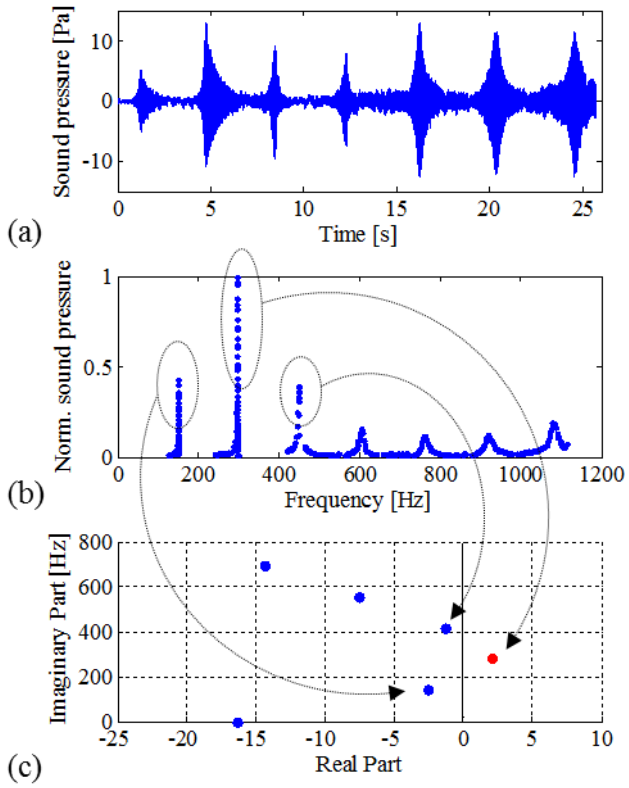

Figure 3.8 Sound pressure fluctuations (a), FFTs of the shifting window (b), approximate root locations (c) for x_u=10.2 cm.

The findings of four separate tests are displayed in Figure 3.8 to Figure 3.11. In panes (a), sound pressure fluctuations are shown. Panes (b) display the FFT of the shifting window data segments (as explained above). Finally, panes (c) present the dominant roots of the mathematical model obtained via QPmR. The sensitive frequencies from these experiments match those of the dominant characteristic modes considerably well (see Table 3.4).

Notice that the tests for Figure 3.8 and Figure 3.10 (for x_u = 10.2 cm and 76.2 cm, respectively) are performed at heater locations where the CTCR declares instability according to Figure 3.4. Experimentally, however, these instabilities were not observed. Nevertheless, the most sensitive

frequencies as revealed by these tests are observed at values that were anticipated as the resonant frequencies of the expected unstable modes. In both cases these sensitive frequencies exhibit high-Q factors. Therefore one can claim that they represent a system very close to resonance conditions, if not in resonance. This observation is interesting from a system identification point of view and it provides another tool for validating the linearized system model that is processed through the CTCR paradigm.

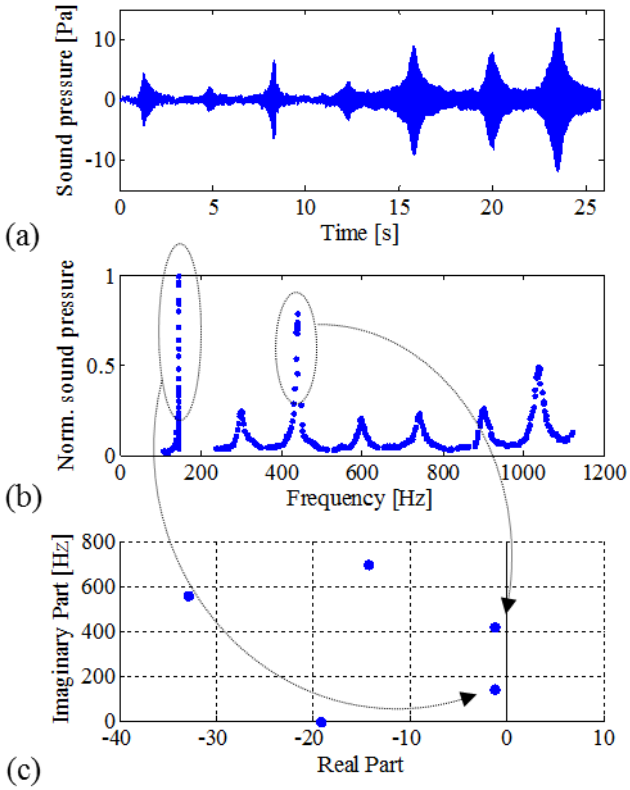

Figure 3.9 Sound pressure fluctuations (a), FFTs of the shifting window (b), approximate root locations (c) for x_u=50.8 cm.

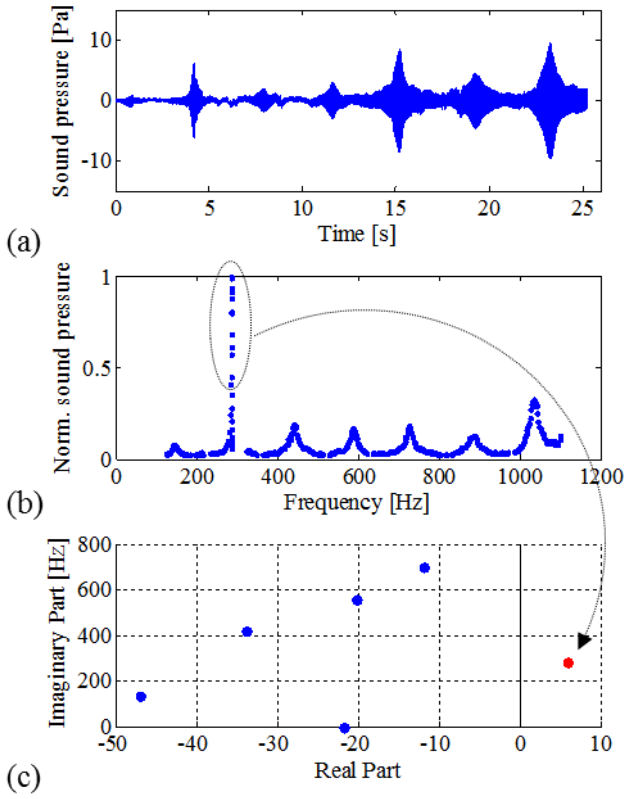

Figure 3.10 Sound pressure fluctuations (a), FFTs of the shifting window (b), approximate root locations (c) for x_u=76.2 cm.

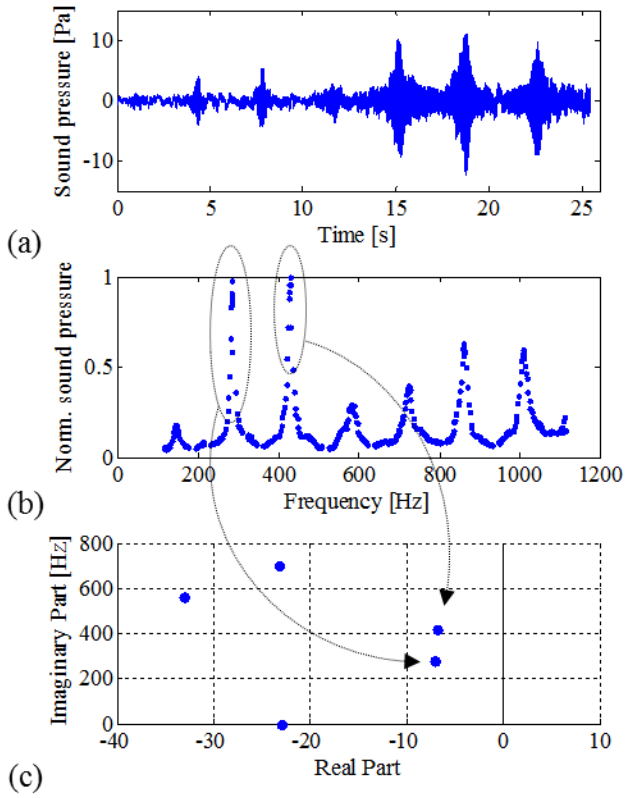

Figure 3.11 Sound pressure fluctuations (a), FFTs of the shifting window (b), approximate root locations (c) for x_u=86.4 cm.

Table 3.4 Experimental and theoretical sensitive frequencies.

x_u	Experimental	QPMR	Error %
10.2 cm	151.7 Hz	141.5 Hz	6.35
	298.3 Hz	280.3 Hz	6.03
	450.0 Hz	419.1 Hz	6.86
50.8 cm	145.0 Hz	141.8 Hz	2.21
	438.3 Hz	419.1 Hz	4.38
76.2 cm	285.0 Hz	280.5 Hz	1.58
86.4 cm	283.3 Hz	279.6 Hz	1.31
	428.3 Hz	418.9 Hz	2.19

Chapter 4 Active Control of Thermoacoustic Instability

Thermoacoustic instabilities yield growing pressure oscillations which are detrimental to the combustor-like structures [9]. They cause excessive vibrations leading to fatigue failures and unacceptable levels of acoustic noise. These motivated many researchers to seek ways to suppress these pressure oscillations and, better yet, to prevent the onset of instabilities [3], [14].

Among the active and passive approaches to abate thermoacoustic oscillations, the former is more favored if there is need to respond to dynamic variations in the operating conditions, as the latter is usually effective only over a narrow frequency range [79]. Active control of the acoustic oscillations is usually implemented as direct modulations in acoustic pressure or fuel injection flow rates. A representative signal of the unstable dynamics in the combustor is observed, either through pressure transducers or heat-release sensors. These measurements are then fed back to the system for stabilizing the thermoacoustic coupling. Loudspeakers are used as actuators to create the controlled pressure field, while fuel valves are used for fuel modulation [8].

One of the traditional control strategies to stabilize the combustor is *phase-shift control*. Many implementations of this strategy have been reported in recent decades, for which the controller parameters are typically determined using empirical methods. The exercise potentially suppresses one unstable mode (see [14] and references therein). It brings in, however, the risk of instabilities at secondary frequencies corresponding to other dynamic modes. Other linear control strategies such as H_∞ , LQG [1], adaptive approaches like self-tuning regulators [21] and online tuning via extremum seeking [3] have also been suggested for the control of thermoacoustic instabilities with various levels of demonstrable success.

In this chapter time-delayed integral (TDI) control is used as the feedback control law to suppress the thermoacoustic instabilities in Rijke tube. Time delays are generally considered to be undesirable entities in a control setting. When they are carefully tuned, however, evidence supports the possibility that the

closed-loop performance may improve considerably [53]. Another aspect of control laws with delay is their apparent practicality, as the sensed pressure variations can be easily delayed in the feedback loop.

In this chapter, first an LTI-NMTDS model is developed in the state-space for the controlled thermoacoustic dynamics in the Rijke tube. For unstable operating conditions, a stabilizing TDI control logic is synthesized for this system using a completely analytical and holistic procedure, the CTCR paradigm. This method is shown to avoid the aforementioned issues vis-à-vis the empirical nature of the design of the phase-shift controllers. An analytical performance evaluation is also conducted for the controller over a wide range of controller parameters. These analytical findings are compared with experimental results from a Rijke tube set-up throughout the chapter.

4.1 Rijke Tube with Feedback Control: A State-space Approach

The mathematical model of uncontrolled Rijke tube was derived previously in Chapter 3. Here, this model is extended with the addition of a feedback loop to the system dynamics as shown with blue in Figure 4.1a. If the dynamics in the Rijke tube is unstable, this feedback-control loop can be synthesized to stabilize it. The feedback loop consists of a microphone as a sensor and a loudspeaker as an actuator. The microphone measures the pressure oscillations $\tilde{p}(x_m,t)$ at the microphone location $x=x_m$, and sends them to the controller. The control signal is then fed back to the system via the loudspeaker, in the form of a pressure wave, $w(t)$.

Similar to the development in Chapter 3, the dynamics in Figure 4.1a translates to the block diagram in Figure 4.1b in Laplace domain. The pressure waves along the Rijke tube are declared as $F_i(s)$ and $G_i(s)$ at different locations $i=1,\ldots,5$. They are the Laplace domain representations of the acoustic wave expressions $f_i(t)=f(x_i,t)$ and $g_i(t)=g(x_i,t)$ with the subscripts $i=1,\ldots,5$ denoting the locations in Figure 4.1a where these functions are evaluated. Accordingly $\tilde{P}_4(s)$ and $W(s)$ are the Laplace

transforms of $\tilde{p}(x_m,t)$ and $w(t)$. Next, state-space representations of both uncontrolled and feedback-controlled Rijke tube dynamics are derived.

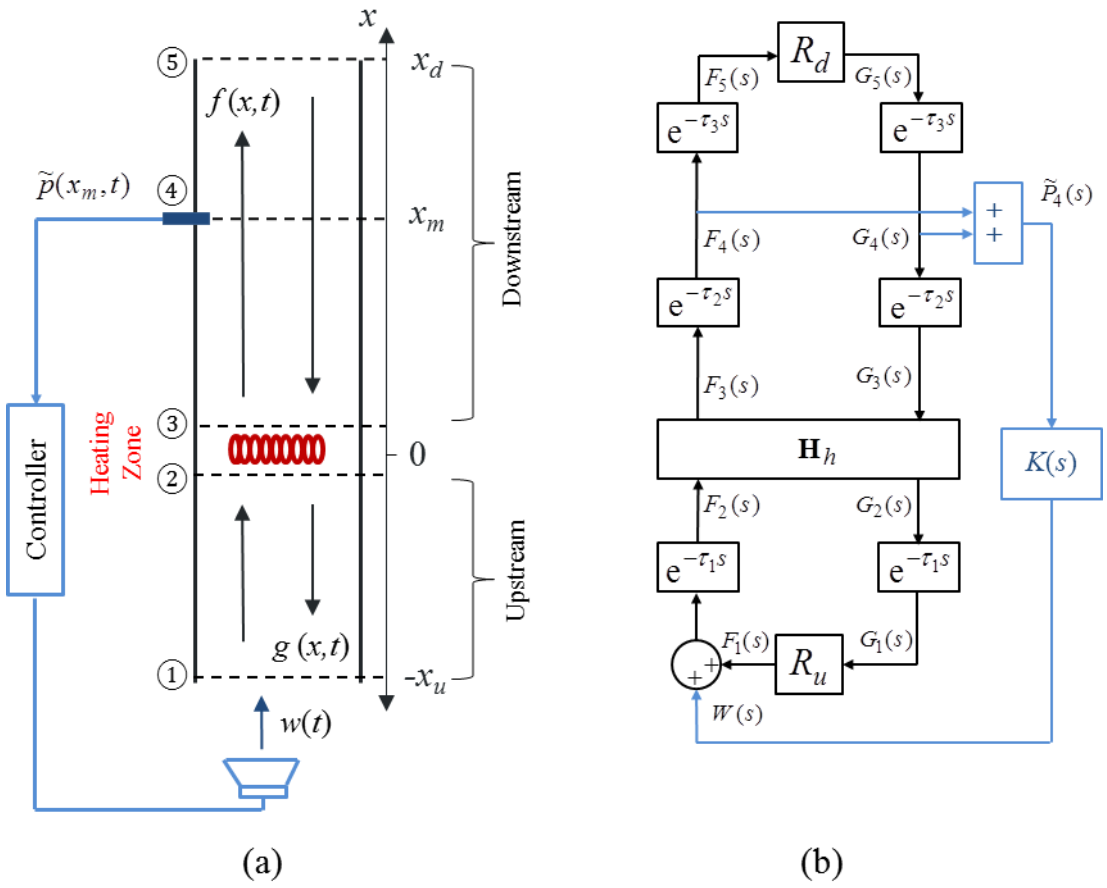

Figure 4.1 The schematic of the controlled Rijke tube and (b) the block diagram representation of the dynamic interactions.

4.1.1 Uncontrolled dynamics

The uncontrolled thermoacoustic dynamics in the Rijke tube was studied in Chapter 3. Here, a state-space realization of this dynamics is developed. Starting with the heating zone between cross-sections ② and ③, a conventional state-space realization of the transfer matrix $\mathbf{H}_h$ [see Equation (3.16)] can be written as

$$\begin{aligned}\dot{\mathbf{x}}(t) &= \mathbf{A}\mathbf{x}(t) + \mathbf{B}\mathbf{v}(t)\\ \mathbf{y}(t) &= \mathbf{C}\mathbf{x}(t) + \mathbf{D}\mathbf{v}(t)\end{aligned} \tag{4.1}$$

where $\mathbf{v}(t) = [\, f_2(t) \;\; g_3(t)]^{\mathrm{T}}$ and $\mathbf{y}(t) = [g_2(t) \;\; f_3(t)]^{\mathrm{T}}$. Note that $\mathbf{v}(t)$ is not the commonly known control action, but the input to the transfer operation in (4.1) that creates the output $\mathbf{y}(t)$. The dynamics is uncontrolled in the classical control theoretic sense. $\mathbf{x}(t)$ is the internal state vector that represents the state of the thermoacoustic coupling dynamics, $\mathbf{H}_h$. Because infinitely many state space representations for $\mathbf{H}_h$ can be obtained, $\mathbf{x}(t)$ is non-unique [48]. Depending on the form of the flame transfer function, $\phi(s)$, the dimension of the coefficient matrices in (4.1) may vary. For the case when $\phi(s)$ is a first-order transfer function as in (3.14), $\mathbf{x}(t)$ is 2×1 and the matrices **A**, **B**, **C** and **D** are all 2×2. The derivation of the particular form of (4.1) is possible through decomposition of $\mathbf{H}_h$ matrix as follows

$$\mathbf{H}_h = \begin{bmatrix} d_{11} & d_{12} \\ d_{21} & d_{22} \end{bmatrix} + \frac{1}{s + a_0}\begin{bmatrix} b_{11} & b_{12} \\ b_{21} & b_{22} \end{bmatrix} \tag{4.2}$$

where the coefficients a_0, d_{ij}, b_{ij} $\; i, j = 1,2$ contain the system parameters such as ($\bar{c}_u$, $\bar{c}_d$, γ, …). Defining an internal state vector as $\mathbf{x}(t) = [x_1(t) \;\; x_2(t)]^{\mathrm{T}}$ the state-space representation in (4.1) can be obtained by picking the **A**, **B**, **C** and **D** matrices as

$$\mathbf{A} = \begin{bmatrix} -a_0 & 0 \\ 0 & -a_0 \end{bmatrix},\; \mathbf{B} = \begin{bmatrix} b_{11} & b_{12} \\ b_{21} & b_{22} \end{bmatrix},\; \mathbf{C} = \begin{bmatrix} 1 & 0 \\ 0 & 1 \end{bmatrix},\; \mathbf{D} = \begin{bmatrix} d_{11} & d_{12} \\ d_{21} & d_{22} \end{bmatrix} \tag{4.3}$$

Notice that **C** is taken as an identity matrix and therefore omitted from expressions in the remainder of the chapter.

For the uncontrolled dynamics, following the functional causality described by Figure 4.1b, $\mathbf{v}(t) = [\, f_2(t) \;\; g_3(t)]^{\mathrm{T}}$ is connected to $\mathbf{y}(t) = [g_2(t) \;\; f_3(t)]^{\mathrm{T}}$ through some time delays $\tau_1 = x_u / \bar{c}_u$, $\tau_2 = x_m / \bar{c}_d$, $\tau_3 = (x_d - x_m)/\bar{c}_d$ and the boundary conditions R_u and R_d at cross-sections ① and ⑤.

Different from Chapter 3, the delay in the downstream section is split into τ_2 and τ_3, although there is no such separation for the uncontrolled system. This feature only appears when a feedback control is implemented using a microphone. Then one can write an additional relation between the input $\mathbf{v}(t) = [\, f_2(t) \;\; g_3(t)]^{\mathrm{T}}$ and the output $\mathbf{y}(t) = [g_2(t) \;\; f_3(t)]^{\mathrm{T}}$ using

$$\begin{aligned} f_2(t) &= R_u g_2(t - 2\tau_1) \\ g_3(t) &= R_d f_3(t - 2\tau_2 - 2\tau_3) \end{aligned} \tag{4.4}$$

as

$$\mathbf{v}(t) = \mathbf{R}_1 \mathbf{y}(t - 2\tau_1) + \mathbf{R}_2 \mathbf{y}(t - 2\tau_2 - 2\tau_3), \qquad \mathbf{R}_1 = \begin{pmatrix} R_u & 0 \\ 0 & 0 \end{pmatrix}, \; \mathbf{R}_2 = \begin{pmatrix} 0 & 0 \\ 0 & R_d \end{pmatrix} \tag{4.5}$$

By substituting (4.5) in (4.1), one obtains

$$\begin{aligned} \dot{\mathbf{x}}(t) &= \mathbf{A}\mathbf{x}(t) + \mathbf{B}\mathbf{R}_1 \mathbf{y}(t - 2\tau_1) + \mathbf{B}\mathbf{R}_2 \mathbf{y}(t - 2\tau_2 - 2\tau_3) \\ \mathbf{y}(t) &= \mathbf{x}(t) + \mathbf{D}\mathbf{R}_1 \mathbf{y}(t - 2\tau_1) + \mathbf{D}\mathbf{R}_2 \mathbf{y}(t - 2\tau_2 - 2\tau_3) \end{aligned} \tag{4.6}$$

Solving $\mathbf{x}(t)$ from the second equation in (4.6) and substituting it in the first, one obtains

$$\dot{\mathbf{y}}(t) + \overline{\mathbf{A}}\dot{\mathbf{y}}(t - 2\tau_1) + \overline{\mathbf{B}}\dot{\mathbf{y}}(t - 2\tau_2 - 2\tau_3) = \overline{\mathbf{C}}\mathbf{y}(t) + \overline{\mathbf{D}}\mathbf{y}(t - 2\tau_1) + \overline{\mathbf{E}}\mathbf{y}(t - 2\tau_2 - 2\tau_3) \tag{4.7}$$

where $\overline{\mathbf{A}} = -\mathbf{D}\mathbf{R}_1$, $\overline{\mathbf{B}} = -\mathbf{D}\mathbf{R}_2$, $\overline{\mathbf{C}} = \mathbf{A}$, $\overline{\mathbf{D}} = [\mathbf{B} - \mathbf{A}\mathbf{D}]\mathbf{R}_1$, $\overline{\mathbf{E}} = [\mathbf{B} - \mathbf{A}\mathbf{D}]\mathbf{R}_2$ are all 2×2 matrices. This equation represents the uncontrolled thermoacoustic dynamics in the Rijke tube. Notice that $\mathbf{y}(t) = [g_2(t) \;\; f_3(t)]^{\mathrm{T}}$ acts as the state-variable vector in this representation.

4.1.2 Feedback-controlled Rijke tube and time-delayed integral control

Next the feedback control loop is incorporated in the system dynamics. In Figure 4.1b, recorded pressure oscillations by the microphone and the control-pressure waves generated by the loudspeaker are denoted by $\tilde{P}_4(s)$ and $W(s)$, respectively. They are related through a transfer function $K(s)$ as

$$W(s) = K(s)\tilde{P}_4(s) \tag{4.8}$$

The sensor dynamics, the control logic, and the actuator dynamics are all embedded within $K(s)$. In this study, both the actuator (the loudspeaker) and the sensor (the microphone) are considered to be components with a flat frequency response within the frequency range of interest. This is a common assumption in Rijke tube control studies [14]. However, different transfer functions representing the sensor/actuator variations in the system could also be included in the future, if necessary.

The loudspeaker wave engages with the system at the upstream end. This action supplements the boundary condition there as

$$f_1(t) = R_u g_1(t) + w(t) \tag{4.9}$$

With this modification the input vector $\mathbf{v}(t) = [\, f_2(t) \;\; g_3(t)]^{\mathrm{T}}$ can be rewritten similarly to (4.5) as

$$\mathbf{v}(t) = \mathbf{R}_1\mathbf{y}(t-2\tau_1) + \mathbf{R}_2\mathbf{y}(t-2\tau_2-2\tau_3) + \mathbf{w}(t-\tau_1) \tag{4.10}$$

where $\mathbf{w}(t) = [1 \;\; 0]^{\mathrm{T}} w(t)$ is the loudspeaker wave. Following the same procedure used to obtain (4.7), the system dynamics with the feedback control becomes

$$\begin{aligned} \dot{\mathbf{y}}(t) + \overline{\mathbf{A}}\dot{\mathbf{y}}(t-2\tau_1) + \overline{\mathbf{B}}\dot{\mathbf{y}}(t-2\tau_2-2\tau_3) + \overline{\mathbf{F}}\dot{\mathbf{w}}(t-\tau_1) \\ = \overline{\mathbf{C}}\mathbf{y}(t) + \overline{\mathbf{D}}\mathbf{y}(t-2\tau_1) + \overline{\mathbf{E}}\mathbf{y}(t-2\tau_2-2\tau_3) + \overline{\mathbf{G}}\mathbf{w}(t-\tau_1) \end{aligned} \tag{4.11}$$

where $\overline{\mathbf{F}} = -\mathbf{D}$ and $\overline{\mathbf{G}} = \mathbf{B} - \mathbf{AD}$. The rest of the matrices are identical to the ones in (4.7).

Next, the loudspeaker wave is expressed in terms $\mathbf{y}(t)$. From (3.6), the pressure fluctuations at cross-section ④ is written as

$$\tilde{p}_4(t) = f_4(t) + g_4(t) = [0 \quad 1]\left\{\begin{pmatrix} g_1(t) \\ f_4(t) \end{pmatrix} + \begin{pmatrix} f_1(t) \\ g_4(t) \end{pmatrix}\right\} \tag{4.12}$$

Following the state flow in Figure 4.1b, one can write

$$\begin{pmatrix} g_1(t) \\ f_4(t) \end{pmatrix} = \begin{bmatrix} 1 & 0 \\ 0 & 0 \end{bmatrix} \mathbf{y}(t-\tau_1) + \begin{bmatrix} 0 & 0 \\ 0 & 1 \end{bmatrix} \mathbf{y}(t-\tau_2) \tag{4.13}$$

and

$$\begin{pmatrix} f_1(t) \\ g_4(t) \end{pmatrix} = \begin{bmatrix} R_u & 0 \\ 0 & 0 \end{bmatrix} \mathbf{y}(t-\tau_1) + \begin{bmatrix} 0 & 0 \\ 0 & R_d \end{bmatrix} \mathbf{y}(t-\tau_1-2\tau_3) \tag{4.14}$$

Substituting (4.13) and (4.14) in (4.12) one gets

$$\tilde{p}_4(t) = [0 \quad 1]\mathbf{y}(t-\tau_2) + [0 \quad R_d]\mathbf{y}(t-\tau_2-2\tau_3) \tag{4.15}$$

In (4.8), $K(s)$ can be regarded as the feedback control law. In this study a time-delayed integral (TDI) control logic is selected with two independent parameters: a control gain K_i and artificial control delay τ_4;

$$w(t) = -\int_0^t K_i \tilde{p}_4(t-\tau_4)dt\,, \qquad K(s) = -\frac{K_i\, \mathrm{e}^{-\tau_4 s}}{s} \tag{4.16}$$

This is, in effect, a filtered $\tilde{p}_4(t)$ signal with τ_4 seconds delay. Notice that τ_4 is a pure time delay imposed on the feedback signal. In practice, this effect is implemented by *artificially increasing* the inherent measurement, computation, and actuation time buffer in the feedback line. This paradoxical play on feedback delays, when properly implemented, could restore desirable (effectively stable) system characteristics akin to a recent control logic called *delay scheduling* [25], [53].

It is worth stressing that τ_4 has nothing to do with a particular modal frequency or a particular phase angle for that frequency as in traditional delayed controllers [3], [31]. Therefore, for the proposed control law, the knowledge of a particular frequency (of the mode to be suppressed) is not needed. This brings us

to the fact that the proposed control law is *modal neutral*. It establishes the stability for the entirety of the infinite dimensional dynamics. This is a significant novelty and advantage over the state-of-the-art control applications categorized as phase-shift controllers (Table 1 in [14]).

Substituting (4.15) and (4.16) in $\mathbf{w}(t)$, one obtains

$$\mathbf{w}(t) = \overline{\mathbf{K}}_1 \int_0^t \mathbf{y}(t-\tau_2-\tau_4)dt + \overline{\mathbf{K}}_2 \int_0^t \mathbf{y}(t-\tau_2-2\tau_3-\tau_4)dt, \qquad \overline{\mathbf{K}}_1 = \begin{bmatrix} 0 & -K_i \\ 0 & 0 \end{bmatrix}, \ \overline{\mathbf{K}}_2 = \begin{bmatrix} 0 & -K_i R_d \\ 0 & 0 \end{bmatrix} \tag{4.17}$$

Defining

$$\mathbf{y}_I(t) = \int_0^t \mathbf{y}(t)dt \quad \text{or} \quad \dot{\mathbf{y}}_I(t) = \mathbf{y}(t) \tag{4.18}$$

(4.17) can be rewritten as

$$\mathbf{w}(t) = \overline{\mathbf{K}}_1 \mathbf{y}_I(t-\tau_2-\tau_4) + \overline{\mathbf{K}}_2 \mathbf{y}_I(t-\tau_2-2\tau_3-\tau_4) \tag{4.19}$$

Then, substituting (4.18) and (4.19) in (4.8) one obtains a system of equations in terms of $\mathbf{y}_I(t)$ and $\mathbf{y}(t)$ as follows:

$$\begin{aligned} \dot{\mathbf{y}}(t) + \overline{\mathbf{A}}\dot{\mathbf{y}}(t-2\tau_1) + \overline{\mathbf{B}}\dot{\mathbf{y}}(t-2\tau_2-2\tau_3) &= \overline{\mathbf{C}}\mathbf{y}(t) + \overline{\mathbf{D}}\mathbf{y}(t-2\tau_1) + \overline{\mathbf{E}}\mathbf{y}(t-2\tau_2-2\tau_3) \\ &\quad - \overline{\mathbf{F}}\overline{\mathbf{K}}_1\mathbf{y}(t-\tau_1-\tau_2-\tau_4) - \overline{\mathbf{F}}\overline{\mathbf{K}}_2\mathbf{y}(t-\tau_1-\tau_2-2\tau_3-\tau_4) \\ &\quad + \overline{\mathbf{G}}\overline{\mathbf{K}}_1\mathbf{y}_I(t-\tau_1-\tau_2-\tau_4) + \overline{\mathbf{G}}\overline{\mathbf{K}}_2\mathbf{y}_I(t-\tau_1-\tau_2-2\tau_3-\tau_4) \end{aligned} \tag{4.20}$$

The two systems of equations, (4.18) and (4.20) can be combined together and rewritten in terms of a new state vector $\mathbf{z}(t) = [\mathbf{y}_I(t) \quad \mathbf{y}(t)]^{\mathrm{T}}$ as

$$\begin{aligned} &\dot{\mathbf{z}}(t) + \mathbf{P}_{11}\dot{\mathbf{z}}(t-2\tau_1) + \mathbf{P}_{12}\dot{\mathbf{z}}(t-2\tau_2-2\tau_3) \\ &= \mathbf{P}_{20}\mathbf{z}(t) + \mathbf{P}_{21}\mathbf{z}(t-2\tau_1) + \mathbf{P}_{22}\mathbf{z}(t-2\tau_2-2\tau_3) + \mathbf{P}_{23}\mathbf{z}(t-\tau_1-\tau_2-\tau_4) + \mathbf{P}_{24}\mathbf{z}(t-\tau_1-\tau_2-2\tau_3-\tau_4) \end{aligned} \tag{4.21}$$

where $\mathbf{P}_{11}=\begin{bmatrix}\mathbf{0} & \mathbf{0}\\ \mathbf{0} & \overline{\mathbf{A}}\end{bmatrix}$, $\mathbf{P}_{12}=\begin{bmatrix}\mathbf{0} & \mathbf{0}\\ \mathbf{0} & \overline{\mathbf{B}}\end{bmatrix}$, $\mathbf{P}_{20}=\begin{bmatrix}\mathbf{0} & \mathbf{I}\\ \mathbf{0} & \overline{\mathbf{C}}\end{bmatrix}$, $\mathbf{P}_{21}=\begin{bmatrix}\mathbf{0} & \mathbf{0}\\ \mathbf{0} & \overline{\mathbf{D}}\end{bmatrix}$, $\mathbf{P}_{22}=\begin{bmatrix}\mathbf{0} & \mathbf{0}\\ \mathbf{0} & \overline{\mathbf{E}}\end{bmatrix}$,

$\mathbf{P}_{23}=\begin{bmatrix}\mathbf{0} & \mathbf{0}\\ \overline{\mathbf{GK}}_1 & -\overline{\mathbf{FK}}_1\end{bmatrix}$, and $\mathbf{P}_{24}=\begin{bmatrix}\mathbf{0} & \mathbf{0}\\ \overline{\mathbf{GK}}_2 & -\overline{\mathbf{FK}}_2\end{bmatrix}$ are all 4×4 matrices. Equation (4.21) represents the feedback-controlled thermoacoustic dynamics.

4.2 Experiments: Control of Thermoacoustic Instability and A Performance Criterion

In this section, thermoacoustic instability in the Rijke tube is analyzed under the TDI control law. CTCR-generated stability maps are used to select the controller parameters. For various controller settings, the performance and robustness of the control logic are studied both analytically and experimentally.

The experiments are performed on a simple 50.8 cm-long glass tube with an electrical heating element. The temperatures along the tube are measured by distributed thermocouples. The average temperatures in the upstream and downstream sections are then used to calculate the sound speeds at both sides. A picture of the test set-up is given in Figure 4.2. Sound pressure in the tube is recorded via a piezo-microphone, which is then is sent to a dSpace DS1103 real-time controller where the delayed-integral control law is implemented. The control sampling rate is selected as 10000 Hz. The control signal is then sent to a linear amplifier that powers the loudspeaker. The speaker is positioned at the upstream tube end (air intake port). The actuator (speaker) and sensor (microphone) dynamics are verified to display flat frequency responses within the frequency range of interest. As such they are taken as simple fixed gains, which are taken into account during the implementation of control. The operational parameters in the experiment are listed in Table 4.1. The relevant matrices in the mathematical models (4.7) and (4.21) after substitution of the operational parameters are $\overline{\mathbf{A}}=\begin{bmatrix}-0.0266 & 0\\ 0.9034 & 0\end{bmatrix}$, $\overline{\mathbf{B}}=\begin{bmatrix}0 & 0.9566\\ 0 & 0.0266\end{bmatrix}$, $\overline{\mathbf{C}}=\begin{bmatrix}-685.5618 & 0\\ 0 & -685.5618\end{bmatrix}$,

$$\overline{\mathbf{D}} = \begin{bmatrix} -159.2867 & 0 \\ -796.8592 & 0 \end{bmatrix},\ \overline{\mathbf{E}} = \begin{bmatrix} 0 & -478.2857 \\ 0 & 159.2867 \end{bmatrix},\ \overline{\mathbf{F}} = \begin{bmatrix} 0.0286 & -1.0286 \\ -0.9714 & -0.0286 \end{bmatrix},\ \overline{\mathbf{G}} = \begin{bmatrix} 171.2761 & 514.2857 \\ 856.8378 & -171.2761 \end{bmatrix},$$

$$\overline{\mathbf{K}}_1 = \begin{bmatrix} 0 & -K_i \\ 0 & 0 \end{bmatrix},\ \overline{\mathbf{K}}_2 = \begin{bmatrix} 0 & 0.93K_i \\ 0 & 0 \end{bmatrix}.$$

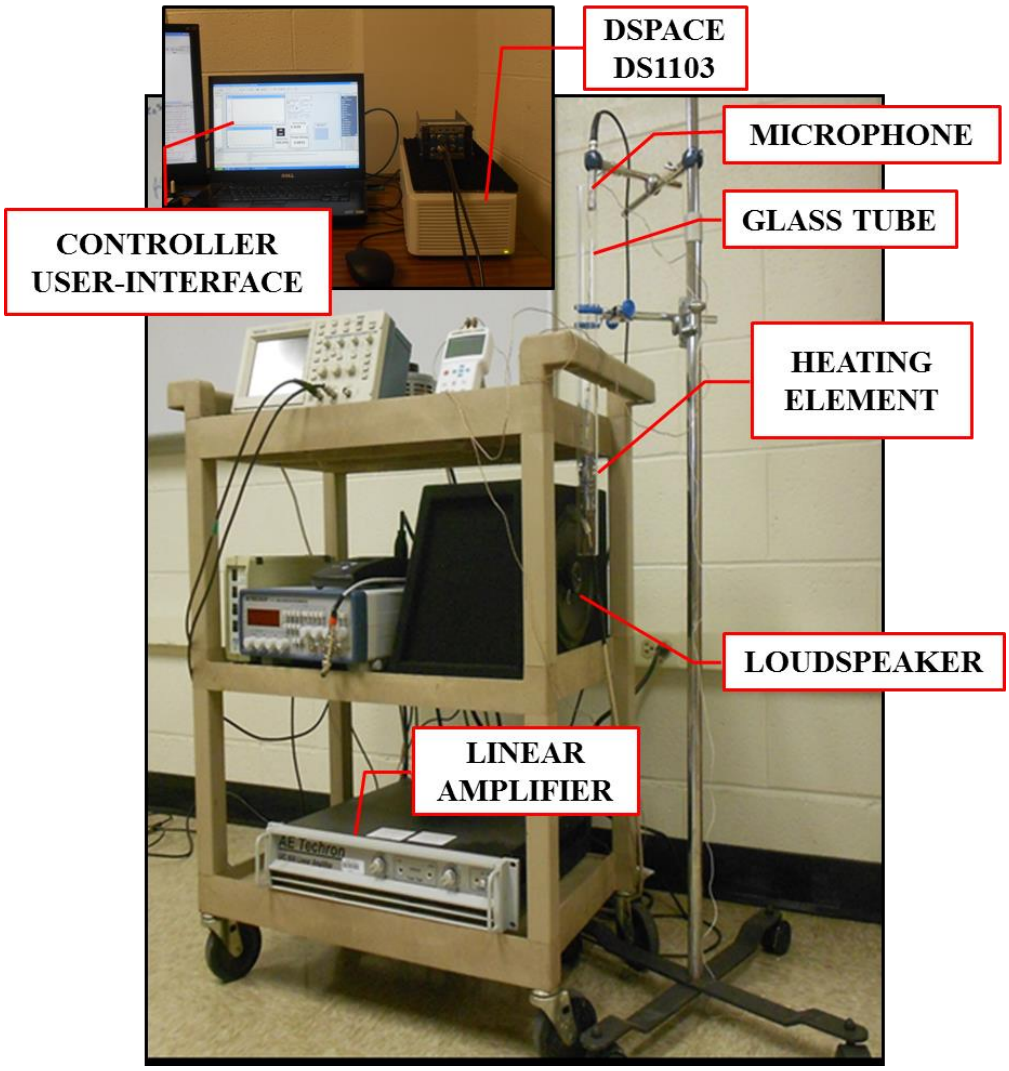

Figure 4.2 The feedback-controlled Rijke tube setup.

In the next subsection, the stability analysis of the uncontrolled Rijke tube is presented first, followed by the controller synthesis to stabilize an unstable operation, with a detailed performance analysis.

Table 4.1 Operational parameters for the feedback controlled Rijke tube experiment.

Parameter	Value	Unit
R_u	-0.93	-
R_d	-0.93	-
γ	1.4	-
A	7.55×10^{-4}	m^2
L	0.508	m
$\bar{\rho}_u$	1.2	kg/m^3
$\bar{c}_u$	340	m/s
$\bar{c}_d$	360	m/s
a	200	-
b	0.002	-

4.2.1 Instability in the uncontrolled system

The state space representation of the uncontrolled thermoacoustic dynamics is taken as in (4.7). First, the stability of its associated difference equation is checked. Defining $\boldsymbol{\tau} = (\tau_u, \tau_d) = (2\tau_1, 2\tau_2 + 2\tau_3)$, the characteristic quasi-polynomial of the associated difference equation of (4.7) is

$$D(s,\boldsymbol{\tau}) = \det(\mathbf{I} + \overline{\mathbf{A}}e^{-\tau_u s} + \overline{\mathbf{B}}e^{-\tau_d s}) = 1 - 0.03e^{-\tau_u s} + 0.03e^{-\tau_d s} - 0.87e^{-(\tau_u+\tau_d)s} = 0 \qquad (4.22)$$

According to Theorem 2.2, all the zeros of (4.22) should lie in $\mathbf{C}^-$. From Corollary 2.1, we have $0.03 + 0.03 + 0.87 < 1$, thus (4.22) is exponentially stable. Therefore Theorem 2.2 is satisfied. Next, we form the characteristic equation representing (4.7), which happens to be factorable as

$$CE(s,\boldsymbol{\tau}) = \det[s(\mathbf{I} + \overline{\mathbf{A}}e^{-\tau_u s} + \overline{\mathbf{B}}e^{-\tau_d s}) - \overline{\mathbf{C}} - \overline{\mathbf{D}}e^{-\tau_u s} - \overline{\mathbf{E}}e^{-\tau_d s}] = CE_1(s) \times CE_2(s,\boldsymbol{\tau}) = 0 \qquad (4.23)$$

where $CE_1(s) = s + 685.56 = 0$ and

$$\begin{aligned} CE_2(s,\boldsymbol{\tau}) = (1 - 0.03e^{-\tau_u s} + 0.03e^{-\tau_d s} - 0.87e^{-(\tau_u+\tau_d)s})s \\ + 685.56 + 159.29e^{-\tau_u s} - 159.29e^{-\tau_d s} - 592.94e^{-(\tau_u+\tau_d)s} = 0 \end{aligned} \qquad (4.24)$$

$CE_1(s)$ has a stationary root at $s = -685.56$, which does not affect the delay-dependent stability of the system. Nevertheless, $CE_2(s, \boldsymbol{\tau})$ is critical from the stability standpoint. CTCR paradigm is implemented on (4.24) to generate the system stability map in the $(\tau_u, \tau_d) \in \Re^{2+}$ domain similar to the treatment in Chapter 3.

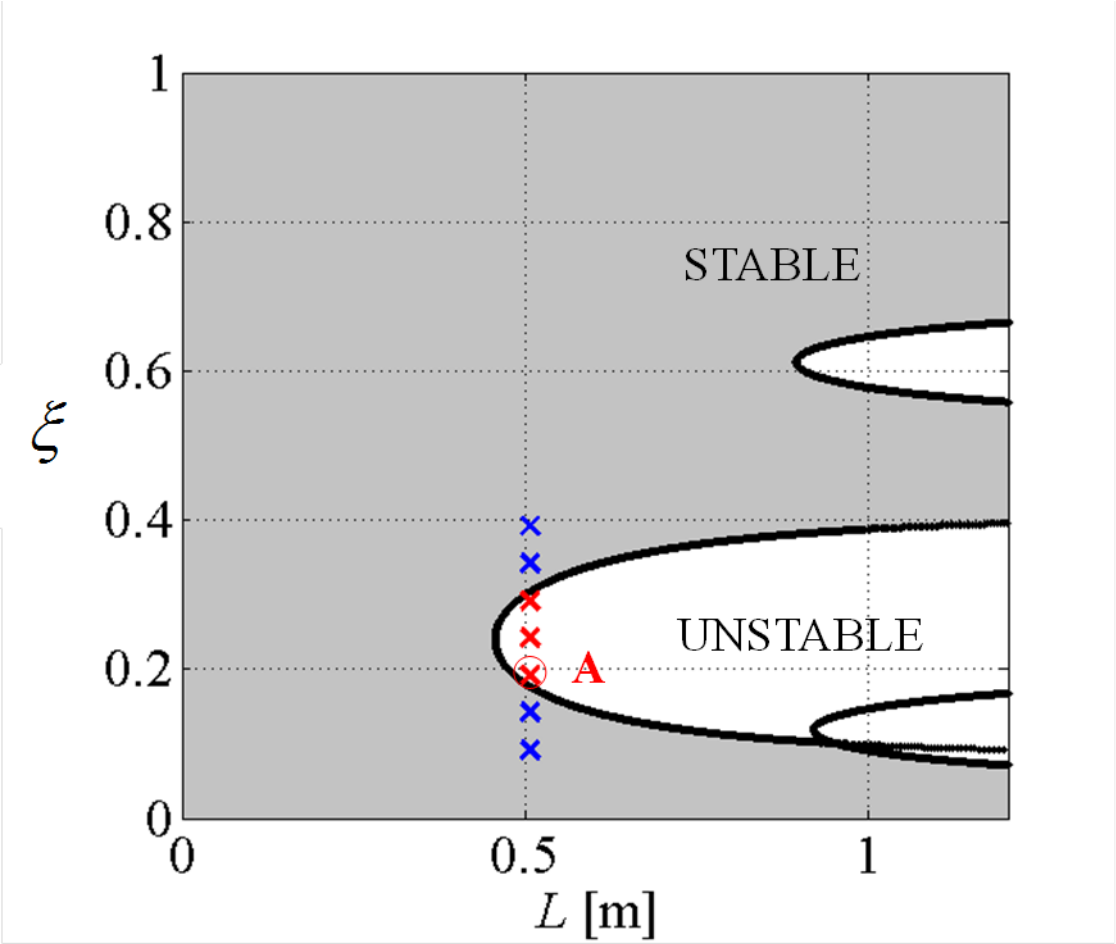

Figure 4.3 Stability map of the uncontrolled Rijke tube setup.

To facilitate visualization, the stability map is plotted in Figure 4.3 in $(L, \xi) \in \Re^{2+}$ domain, where L is the tube length and $\xi = x_u / L$ is the non-dimensional heater location along the tube. All the hypersurfaces (kernel and offspring) are drawn in black. The shaded region, where $NU = 0$, is found to be stable

analytically. The crosses represent the results of the tests that were conducted on the 0.508m length tube. The blue points represent stable operation, whereas the red points correspond to the configurations that render thermoacoustic instability. The analytical and experimental results corroborate each other very well, as displayed in the figure. They are also in accordance with the observations in the reported literature [41], [60] such that the Rijke tube is more susceptible to thermoacoustic instabilities when the heater is located within the lower half of the tube $(\xi < 0.5)$, rather than the upper half $(\xi > 0.5)$.

4.2.2 Feedback stabilization of thermoacoustic instability

Next an unstable operating point (marked with **A** in Figure 4.3) is selected, and the proposed TDI controller is implemented to stabilize the thermoacoustic dynamics. As derived in Section 4.1.2, the controlled system is represented by (4.21) in the state space. When the operational parameters in Table 4.1 are substituted in (4.21), only the controller gain and delay, K_i and τ_4, and the delays representing the duct dimensions τ_1, τ_2, τ_3 remain as the undetermined parameters. The associated difference equation for the controlled Rijke tube is recreated as

$$\begin{aligned} D(s,\boldsymbol{\tau}) &= \det[\,\mathbf{I} + \mathbf{P}_{11}\mathrm{e}^{-2\tau_1 s} + \mathbf{P}_{12}\mathrm{e}^{-(2\tau_2+2\tau_3)s}\,] \\ &= 1 - 0.03\mathrm{e}^{-2\tau_1 s} + 0.03\mathrm{e}^{-(2\tau_2+2\tau_3)s} - 0.87\mathrm{e}^{-(2\tau_1+2\tau_2+2\tau_3)s} = 0 \end{aligned} \tag{4.25}$$

Notice that (4.25) is identical to (4.22), it can also be declared as stable using Corollary 2.1, which satisfies Theorem 2.2.

The complete characteristic equation of the system given in (4.21) can be obtained as

$$\begin{aligned} CE(s,\boldsymbol{\tau}) &= \det\left[s\left(\mathbf{I} + \sum_{k=1}^{2} \mathbf{P}_{1k}\mathrm{e}^{-\tau_k s} \right) - \mathbf{P}_{20} - \sum_{k=1}^{4} \mathbf{P}_{2k}\mathrm{e}^{-\tau_k s} \right] \\ &= CE_1(s) \times CE_2(s,\boldsymbol{\tau}) = 0 \end{aligned} \tag{4.26}$$

where $\boldsymbol{\tau} = (2\tau_1,\, 2\tau_2 + 2\tau_3, \tau_1 + \tau_2 + \tau_4, \tau_1 + \tau_2 + 2\tau_3 + \tau_4)$, $CE_1(s) = s(s + 685.56) = 0$ and

$$CE_2(s,\boldsymbol{\tau}) = (1 - 0.03\mathrm{e}^{-2\tau_1 s} + 0.03\mathrm{e}^{-(2\tau_2+2\tau_3)s} - 0.87\mathrm{e}^{-(2\tau_1+2\tau_2+2\tau_3)s})s^2 + (685.56 + 159.29\mathrm{e}^{-2\tau_1 s}$$
$$- 159.29\mathrm{e}^{-(2\tau_2+2\tau_3)s} - 592.94\mathrm{e}^{-(2\tau_1+2\tau_2+2\tau_3)s} + 0.97K_i\mathrm{e}^{-(\tau_1+\tau_2+\tau_4)s} - 0.90K_i\mathrm{e}^{-(\tau_1+\tau_2+2\tau_3+\tau_4)s})s \quad (4.27)$$
$$+ 856.84K_i\mathrm{e}^{-(\tau_1+\tau_2+\tau_4)s} - 796.86K_i\mathrm{e}^{-(\tau_1+\tau_2+2\tau_3+\tau_4)s} = 0$$

$CE_1(s)$ has two stationary roots at $s = 0$ and $s = -685.56$, independent from the time delays, $\boldsymbol{\tau} \in \Re^{4+}$. Due to the stationary root at $s = 0$, however, the system can be at most marginally stable. Therefore the rest of the discussions in this section are built up on marginal stabilization of (4.26) as the aim.

Table 4.2 Dimensional settings of the Rijke tube

Parameter	Value	Unit
x_u	0.097	m
x_d	0.411	m
x_m	0.385	m

.

For the set of experiments conducted, the tube length and heater location are both fixed at $(L, \xi) = (0.508, 0.191)$. The corresponding upstream and downstream lengths and the microphone location are given in Table 4.2. Notice that this setting represents an unstable Rijke tube when it is not controlled (point **A** in Figure 4.3). Using the parameters in Table 4.1 and Table 4.2, the time delays are calculated as $\tau_1 = 0.29\,\mathrm{ms}$, $\tau_2 = 1.07\,\mathrm{ms}$, and $\tau_3 = 0.07\,\mathrm{ms}$. This leaves K_i and τ_4 as the only unknown parameters in (4.27). $CE_2(s,\boldsymbol{\tau})$ can be rewritten as

$$CE_2(s, K_i, \tau_4) = Q_0(s) + Q_1(s)K_i\mathrm{e}^{-\tau_4 s} = 0 \quad (4.28)$$

where $Q_0(s)$ and $Q_1(s)$ are quasi-polynomials containing the time delays τ_1, τ_2 and τ_3. Now the CTCR paradigm is implemented. The control parameters (K_i, τ_4) on kernel and offspring are solved by substituting $s = \omega\mathrm{i}$ in (4.28) and using the following magnitude and phase conditions:

$$\tau_4(\omega) = \frac{1}{\omega}\left[n\pi + \angle Q_1(\omega \mathrm{i}) - \angle Q_0(\omega \mathrm{i})\right], \; K_i(\omega) = \left|\frac{Q_0(\omega \mathrm{i})}{Q_1(\omega \mathrm{i})}\right|, \qquad n = 1,3,5,\ldots \quad (4.29)$$

Once $\omega \in \Re^+$ is scanned in the range of interest, hypersurfaces that partition the (K_i, τ_4) space are generated. Then, evaluating the *RT* along the kernel and using the *RT* invariance property (Proposition 2 in Chapter 2), the stability map in the space of controller parameters (K_i, τ_4) is obtained (see Figure 4.4a). The *RT* invariance property is also marked at a single point on the kernel.

The experiments start with uncontrolled setting $K_i = 0$ which is unstable (horizontal axis on Figure 4.4a and point **A** on Figure 4.3). The results of each control experiment are displayed on Figure 4.4a as a blue $\times$ for stable and a red $*$ for unstable operations. Experiments mostly agree with the analytical declarations of stability. There are some mismatches very close to the stability boundaries, which are tolerable for such complex systems. There are a couple of discrepancies at the controller selections with $K_i = 750$ and $4.00\,\mathrm{ms} < \tau_4 < 4.50\,\mathrm{ms}$. The analytical results predict failure in stabilization; however, the controller was able to stabilize the system during the experimental tests. To better understand the reason for this disagreement, a zoomed-in version of Figure 4.4a is provided in Figure 4.4b, where the resonant frequencies along the kernel hypercurve are displayed. They vary in that region between 20.6 Hz and 23.6 Hz which is extremely low. Considering the actuator and the sensor used in this study are both unreliable at such low frequencies, one should not expect to experimentally detect the stability transition behavior around this operating point. Better identification of the sensor and actuator dynamics and the resulting improvement in the instability detection capability at secondary frequencies (other than the unstable fundamental modal frequency) will be studied in Chapter 6.

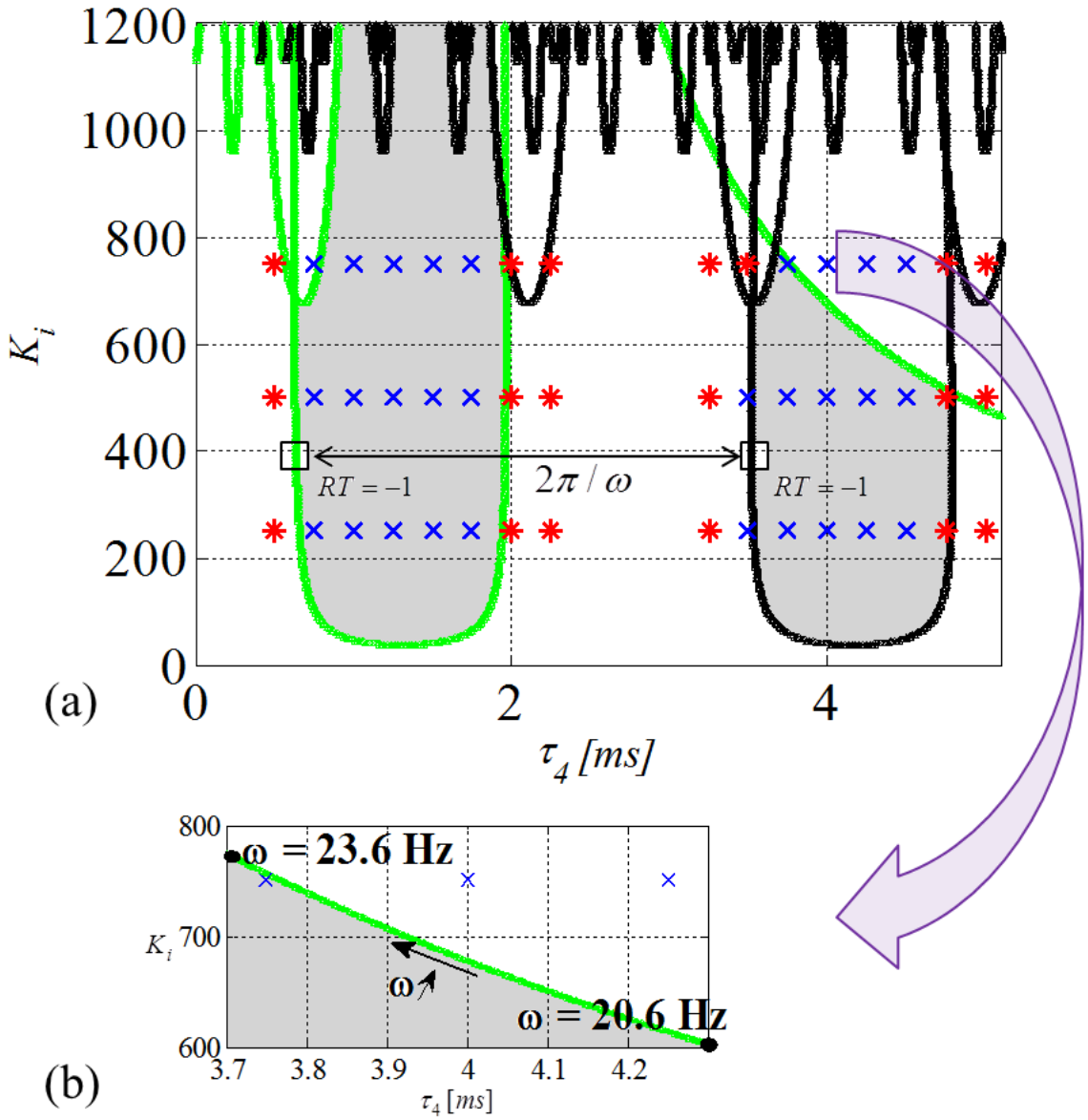

Figure 4.4 (a) Stability map of the controlled Rijke tube setup. Stable regions are shaded grey, kernel is colored green and offspring black. (b) Zoomed-in version shows the low-frequency crossing.

4.2.3 Control robustness and performance analysis

In this section, control performance is studied from a disturbance-rejection perspective for various (K_i, τ_4) compositions. Three related but different pathways are used for this purpose:

(a) To study the control performance analytically, the *relative stability* level map concept is used. First, $s = \sigma + \omega\mathrm{i}$ is substituted in (4.28) to obtain

$$CE_2(\sigma, \omega, K_i, \tau_4) = Q_0(\sigma + \omega\mathrm{i}) + Q_1(\sigma + \omega\mathrm{i}) K_i \mathrm{e}^{-\tau_4(\sigma+\omega\mathrm{i})} = 0 . \tag{4.30}$$

For a certain σ value, the relative stability curves are obtained using the phase and magnitude conditions as follows

$$\tau_4(\omega) = \frac{1}{\omega}\left[n\pi + \angle Q_1(\sigma + \omega\mathrm{i}) - \angle Q_0(\sigma + \omega\mathrm{i})\right], \quad K_i(\omega) = \left| \frac{Q_0(\sigma + \omega\mathrm{i})}{Q_1(\sigma + \omega\mathrm{i})} \mathrm{e}^{\tau_4\sigma} \right|, \quad n = 1, 3, 5, \ldots \tag{4.31}$$

In addition, to capture the effect of any real root on the relative stability analysis, we substitute $s = \sigma$ in (4.28), and solve for the control gain K_i for a given σ and τ_4 value as

$$K_i(\sigma, \tau_4) = -\frac{Q_0(\sigma)}{Q_1(\sigma)} \mathrm{e}^{\tau_4\sigma} \tag{4.32}$$

The relative stability level maps for $\sigma = -5, -12, -18, -26$ are created as shown in Figure 4.5a-d. The shaded regions represent the controller parameters where $\mathrm{Re}(s_{dom}) < \sigma$. One can observe from Figure 4.5 that the most robust control can be achieved if the controller gain K_i is selected as high as possible and if τ_4 is selected close to 1.35 ms .

The curves that are generated by (4.32) (corresponding to real root trajectories) are marked with "*r*" for each case in Figure 4.5a-d. All of these parametric trajectories clearly reside in the unstable operating zones, meaning that the real root is not the dominant one. That is, for each point along the curves *r*, the system exhibits at least a pair of unstable right-half-plane roots. Therefore none of the real roots is relevant from the stability perspective.

(b) Next, the effect of feedback control on the disturbance rejection characteristics is illustrated numerically. For this purpose, the QPmR algorithm is utilized. Implementing QPmR on (4.28) with

$(K_i, \tau_4) = (250, 1.5\,\text{ms})$ and $(K_i, \tau_4) = (500, 1.0\,\text{ms})$, the characteristic root distributions are obtained as in Figure 4.6a and b respectively. One can observe from these figures that the uncontrolled system's characteristic root in $\mathbf{C}^+$ is brought to $\mathbf{C}^-$ using feedback control. This scenario repeats itself at all the controller parameters inside the stable region in Figure 4.4a.

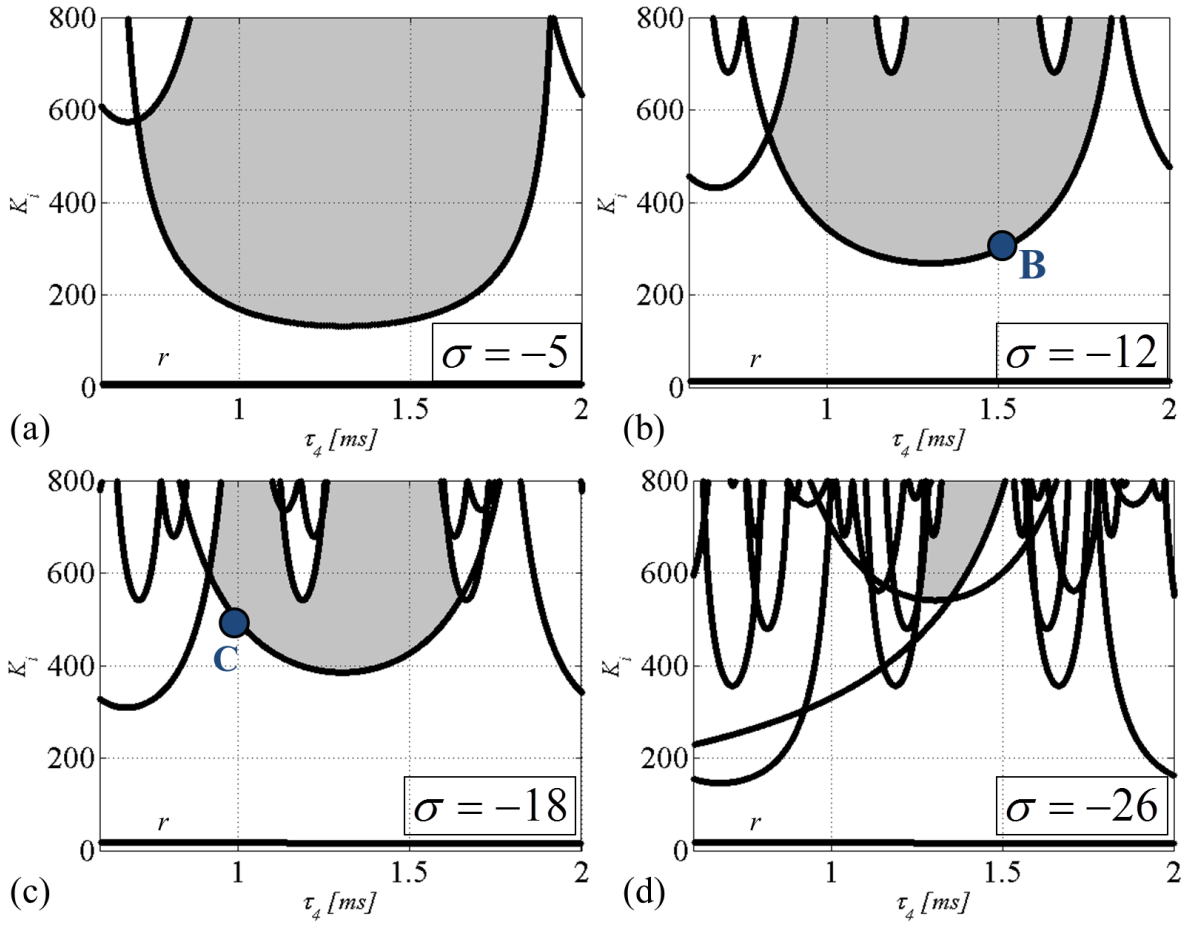

Figure 4.5 The relative stability level maps of the controlled system in (K_i, τ_4) domain for (a) $\sigma = -5$, (b) $\sigma = -12$, (c) $\sigma = -18$, (d) $\sigma = -26$.

The new real part of the stabilized root on Figure 4.6a is very close to -12. This control configuration, $(K_i, \tau_4) = (250, 1.5\,\text{ms})$, is marked as point **B** on Figure 4.5b, which is also on the relative stability curve

with $\sigma = -12$. The same argument can be made for Figure 4.6b and point **C** at $(K_i, \tau_4) = (500, 1.0\,\text{ms})$ on Figure 4.5c, for which $\sigma = -18$. This shows that the analytical stability maps generated in part (a) match well with the numerical results obtained through QPmR in part (b).

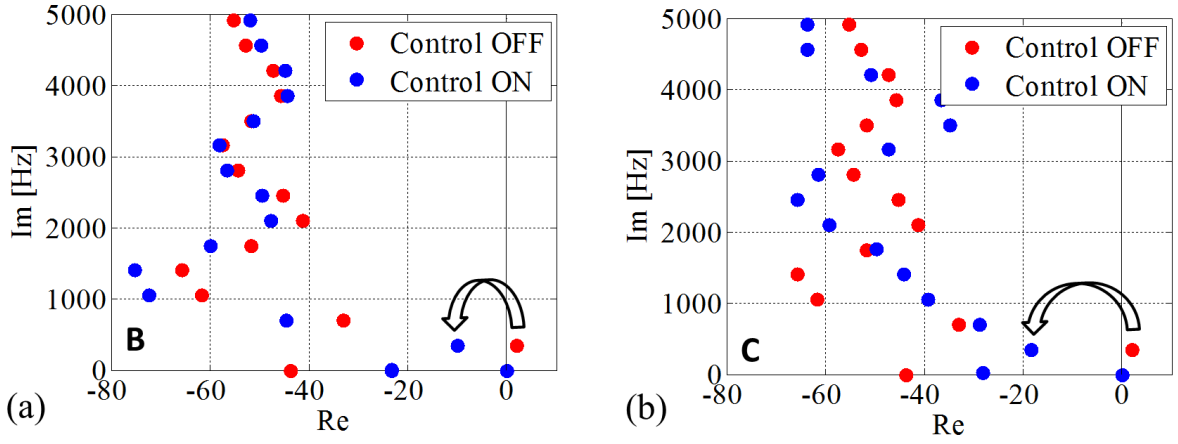

Figure 4.6 Distribution of characteristic roots over the complex plane. Red represents the uncontrolled system, whereas blue is for the controlled system at (a) point **B** on Figure 4.5b, (b) point **C** on Figure 4.5c.

(c) A good descriptor of the robustness of a system is its settling time (or the disturbance rejection speed). This capability can also be used to compare the control performances for different (K_i, τ_4) configurations. Similar to the relative stability boundaries on Figure 4.5, one can sketch settling time contours in (K_i, τ_4) domain as well. Settling time can be computed as approximately 4 times the dominant time constant, where the theoretical time constant is $-1/\sigma$ [48]. Then, using (4.31) with a constant σ, the corresponding *level-settling time* curves can be obtained with the relation $t_s \approx -4/\sigma$. Since the stabilization performance is of interest, we focus on the location of the stabilized root in the complex plane and select the ω scanning range accordingly. The analytical settling time contours (in

seconds) for $\sigma = -5,-10,...,-35$ are obtained as in Figure 4.7a. Then, they are compared with the experimentally determined decay times in Figure 4.7b.

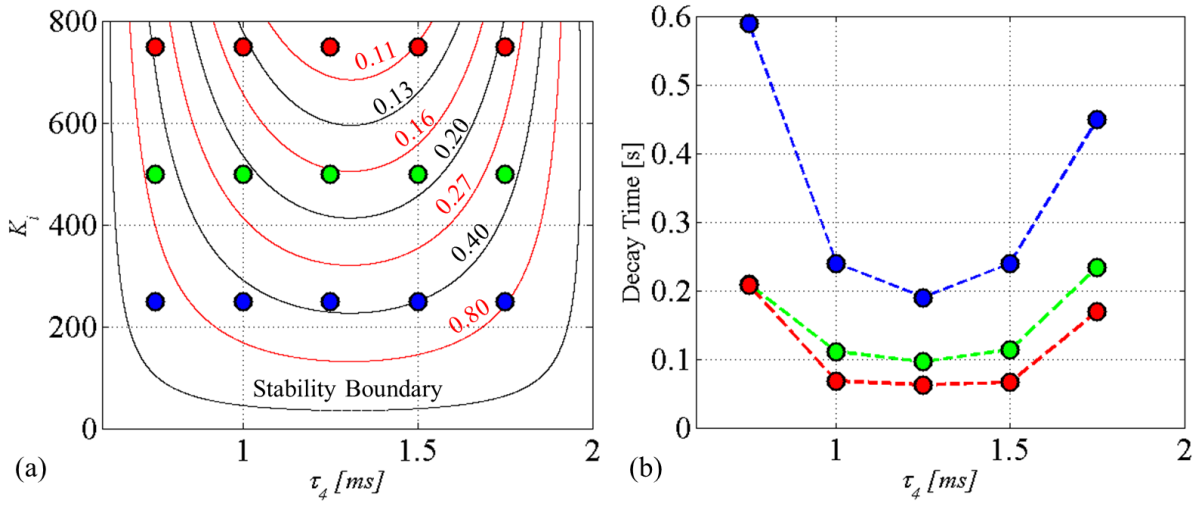

Figure 4.7 (a) Analytical settling time contours (in seconds) and (b) experimental decay time of the stabilized system for various controller parameters.

The experiment is performed with the controller parameters at the red, green and blue dots in Figure 4.7a and the time traces of the pressure oscillations in the tube are recorded. After the controller is turned on, the decay time of the pressure fluctuations at each of these points is calculated and they are displayed on Figure 4.7b. When Figure 4.7a and b are compared, one can see favorable correspondence in the trends. Although the theoretical settling times and the experimental decay times do not exactly coincide, they are of the same order of magnitude. Furthermore their trends are in agreement; increasing K_i prolongs the decay time. Both Figure 4.7a and b agree with our earlier observations from the relative stability maps, that high K_i and $\tau_4 \approx 1.3\text{ms}$ provides the optimal control. It is important to note that the capability of selecting a high gain is practically limited by the experimental equipment such as the actuator.

Some sample time traces of pressure oscillations and the control signal (DAC output) along with the procedure of determining the decay times are given in Figure 4.8 and Figure 4.9 for two arbitrary

(K_i, τ_4) selections: $(250, 1.5\,\text{ms})$ and $(500, 1.0\,\text{ms})$. In both figures, the system starts uncontrolled at $(L, \xi) = (0.508, 0.191)$ and instability sets in. After the amplitude of pressure oscillations grow up to 35-40 Pa, nonlinear effects become dominant and oscillations set into limit cycle modes. Then, the controller is turned on and the unstable-uncontrolled system is stabilized. Both the growth of pressure oscillations at the onset of instability and their decay after the controller is turned on are exponential, which is indicative of linear-system behavior. This observation fortifies the applicability of linear models derived in (4.7) and (4.21) to analyze the stability and control of thermoacoustic dynamics. Furthermore, the frequency spectrum of the sound pressure levels (SPL), before and after control are provided in Figure 4.10 for the two aforementioned (K_i, τ_4) selections. Close to 80dB SPL reduction is observed upon stabilization in both cases.

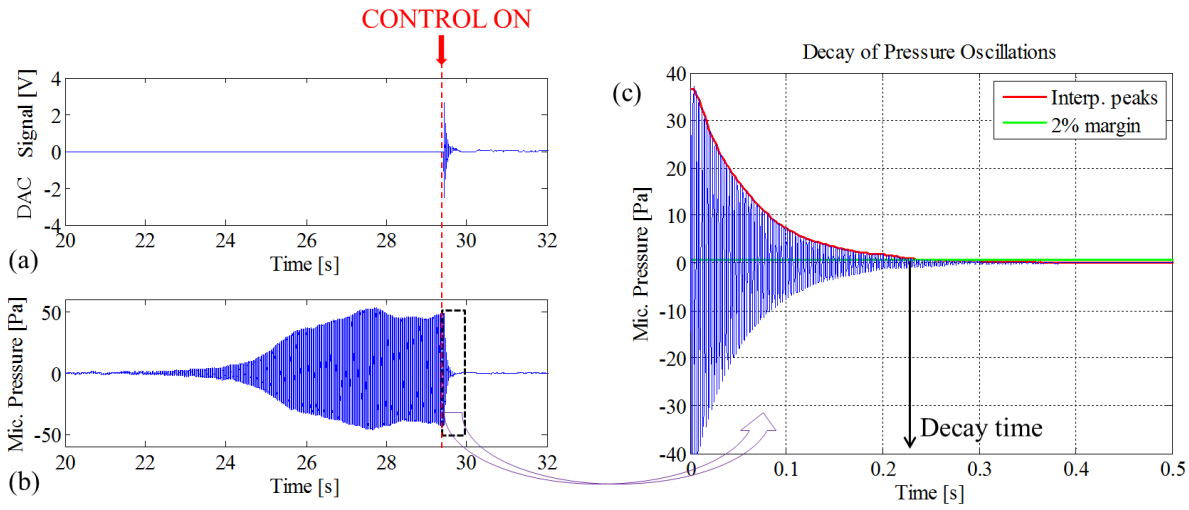

Figure 4.8 (a) Control (DAC) signal (b) pressure oscillations recorded via microphone and (c) experimental decay time determination for $(K_i, \tau_4) = (250, 1.5\,\text{ms})$.

In Figure 4.11a and b, the pressure oscillations measured by the microphone vs. control (DAC) signal, which is sent to the loudspeaker, is plotted for the controller parameters $(K_i, \tau_4) = (250, 0.75\,\text{ms})$ and $(K_i, \tau_4) = (750, 1.25\,\text{ms})$ respectively. These controller configurations correspond to the slowest and

fastest decays in both Figure 4.7a and b. The trajectories start as the controller is turned on and last for about a second. One can see how fast the pressure oscillations approach equilibrium in Figure 4.11b, as compared with Figure 4.11a, therefore declaring the control scheme in Figure 4.11b more effective.

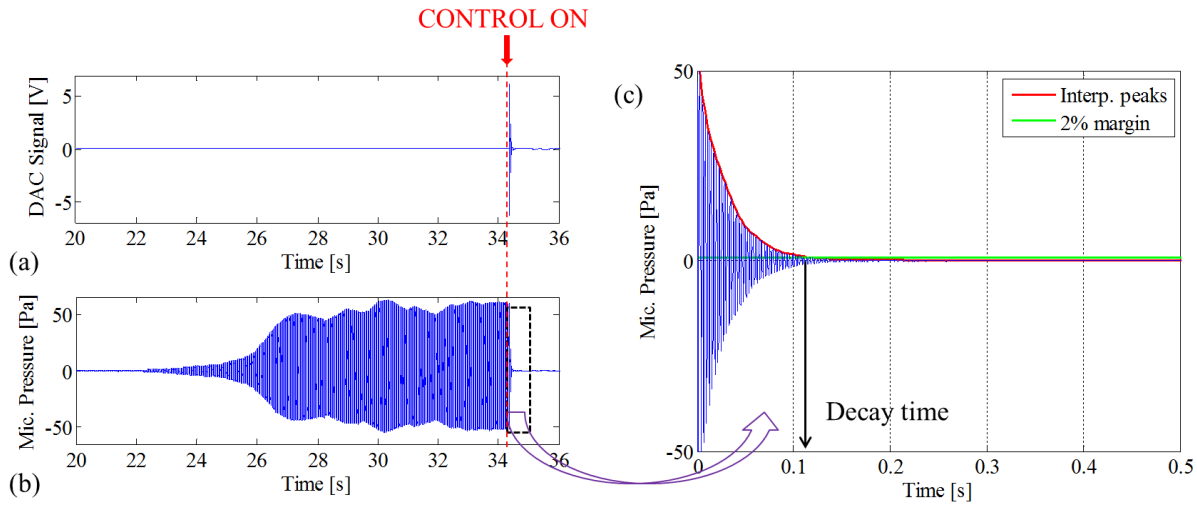

Figure 4.9 (a) Control (DAC) signal (b) pressure oscillations recorded via microphone and (c) experimental decay time determination for $(K_i, \tau_4) = (500, 1.0\,\text{ms})$.

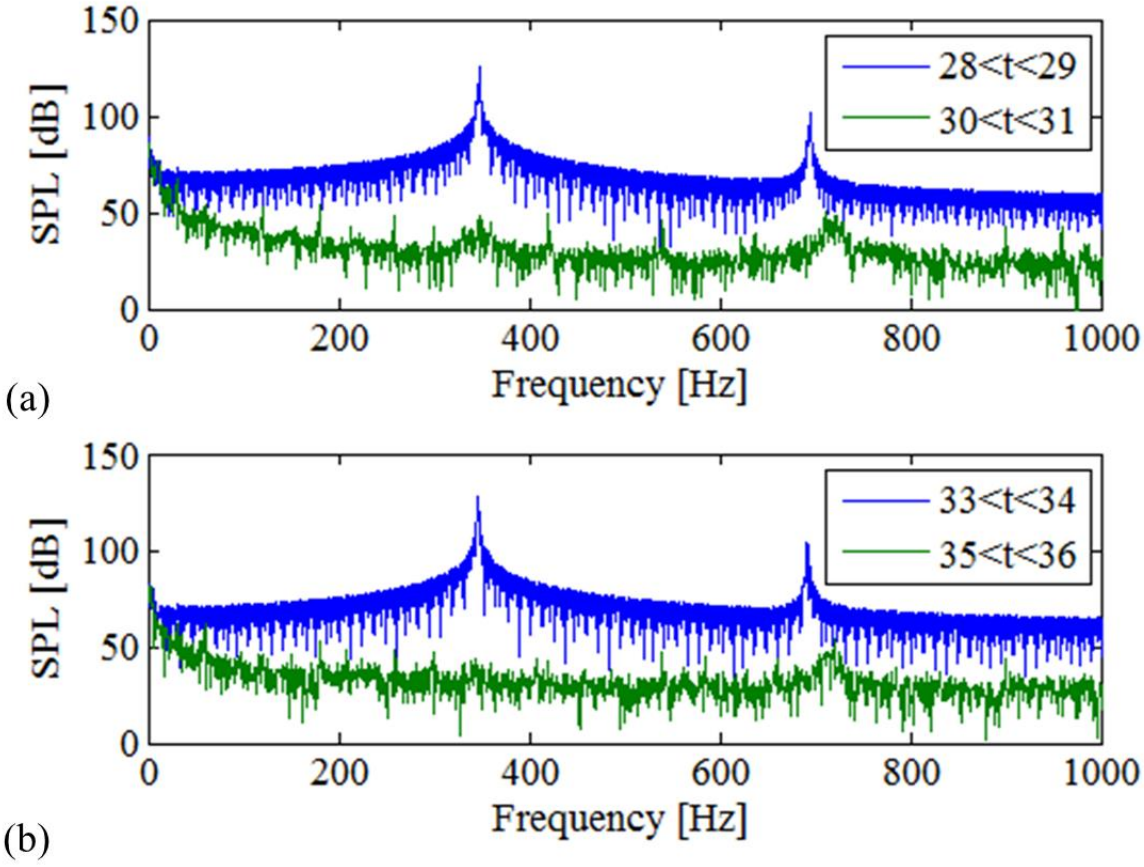

Figure 4.10 Frequency spectrum of sound pressure levels before and after control for (a) $(K_i, \tau_4) = (250, 0.75\,\text{ms})$ and (b) $(K_i, \tau_4) = (750, 1.25\,\text{ms})$.

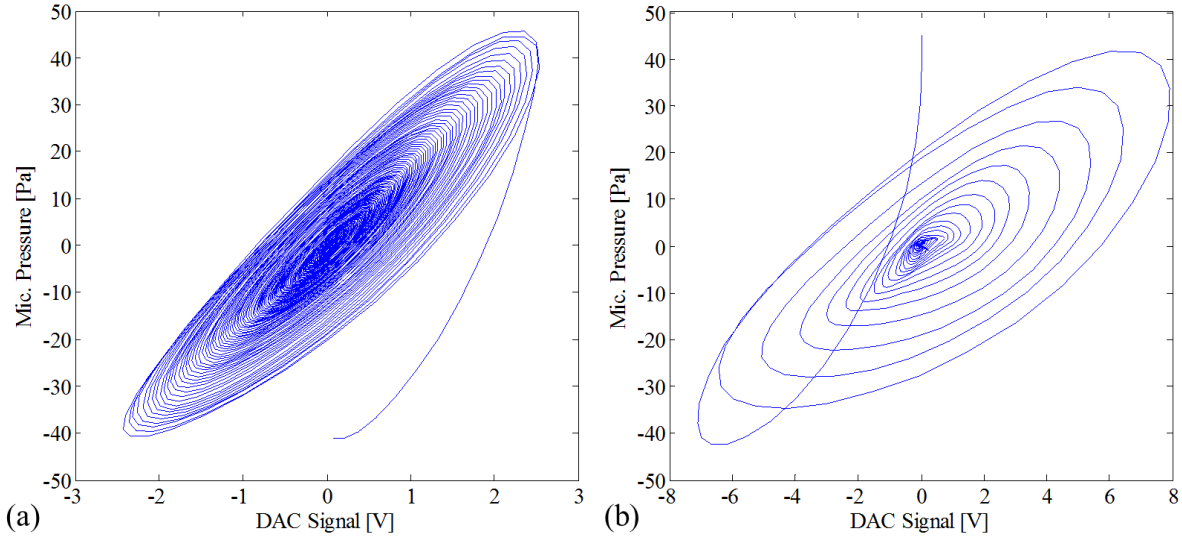

Figure 4.11 Pressure oscillations vs. control signal graphs right after the control is turned on for (a) $(K_i, \tau_4) = (250, 0.75\,\text{ms})$ and (b) $(K_i, \tau_4) = (750, 1.25\,\text{ms})$.

Chapter 5 Passive Control of Thermoacoustic Instability

As mentioned in Chapter 4, control of thermoacoustic instabilities takes two forms: active and passive. As the active approach, feedback control action modulates either acoustic pressure or the fuel injection rates to eliminate thermoacoustic instabilities. One disadvantage of acoustic pressure modulation is the requirement of considerable actuation power, especially when it is transitioned into modern combustors. At industrial scales, fuel modulation is the more viable method; however the limited bandwidth of the fuel valve reduces the control capability. In addition, feedback control has the potential to invite more instability rather than suppression, if it does not work properly [80].

Passive approach is an alternative control technique that does not suffer from the aforementioned issues. Redesigning the chamber, installing some resonators and acoustic liners to the combustor are some such passive control methods [79]. In this chapter, the focus is on the utilization of a Helmholtz resonator to attenuate thermoacoustic instabilities and its effects on the system dynamics.

Helmholtz resonator is a simple encapsulated air cavity as broadly utilized in acoustic structures. When attached to a duct, it imparts a considerable noise reduction within a frequency band around its resonant frequency. Its dynamics has been modeled as a single-degree-of-freedom (SDOF) system in [37] akin to a mechanical vibration absorber (see Figure 5.1). Nonlinear models have also been investigated for such systems in the literature, particularly in the presence of high speed airflow [80]. Helmholtz resonators are widely used as acoustic dampers to abate the combustion-excited oscillations [17].

One critical issue in passive control of thermoacoustic instabilities with resonators is in their proper placement along the duct. In [11], it is shown that wrong placements may result in amplification of pressure oscillations rather than suppression. This study attempts to bring an analytical guideline for this concern.

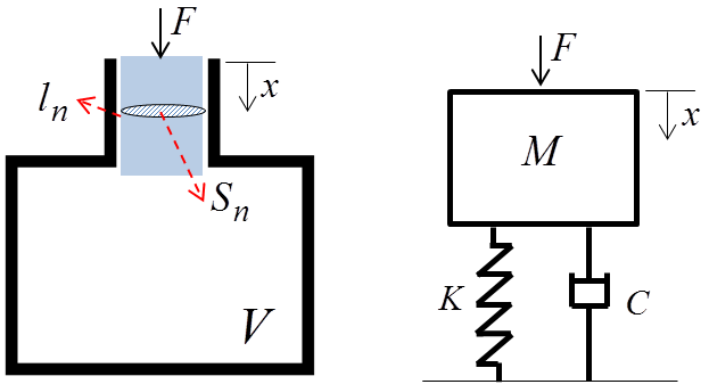

Figure 5.1 The Helmholtz resonator and the mechanical vibration absorber.

First, the Helmholtz resonator dynamics is introduced and its analogy to a mechanical vibration absorber is explained. Then a state-space representation of the Rijke tube dynamics with a Helmholtz resonator is developed in LTI-NMTDS form. Utilizing the CTCR paradigm the stabilizing resonator placements along the duct are revealed for various operating conditions. The analytical findings are supported with experimental results that are obtained using a laboratory-scale Rijke tube setup. Furthermore, a conceptual setting with a strong thermoacoustic coupling is also investigated to observe the resonator's stabilization capability at extreme cases.

5.1 Helmholtz Resonator Dynamics

A Helmholtz resonator is used in an acoustic structure to reduce undesired noise within a frequency band around its resonant frequency. It functions similar to a mechanical vibration absorber as shown in Figure 5.1. The mass of air at the resonator's neck moves against the volume of air in the cavity when excited by external pressure. The air in the larger cavity exerts a counter force on the mass resembling the restoring forces of spring and damper in mechanical vibration absorbers. Small pressure perturbations lead to large oscillating mass fluxes in the neck, which in turn induce energy dissipation and ultimate sound absorption [17].

5.1.1 Mechanical vibration absorber analogy

The air mass at the neck can be expressed as

$$M = l_{eff} S_n \bar{\rho} \tag{5.1}$$

where S_n and l_{eff} are the cross-sectional area and the effective length of the resonator neck, and $\bar{\rho}$ is the air density. The effective neck length of the resonator, when it is attached to a tube (reflecting both end correction factors), is taken as $l_{eff} = l_n + 0.85 d_n$, where l_n is the length and d_n is the diameter of the neck [37]. The stiffness effect that is posed by the air in the cavity can be represented by

$$K = \frac{\bar{c}^2 \bar{\rho} S_n^2}{V} \tag{5.2}$$

where $\bar{c}$ is the speed of sound and V is the volume of the cavity. Then, the undamped natural frequency of the resonator is calculated as

$$\Omega_r = \sqrt{\frac{K}{M}} = \bar{c} \sqrt{\frac{S_n}{V l_{eff}}} \tag{5.3}$$

The resistance or the damping coefficient of a Helmholtz resonator can be expressed as

$$C = \frac{1}{2\pi} \frac{{S_n}^3 \bar{\rho} \bar{c}}{V l_{eff}} \tag{5.4}$$

if the thermoviscous losses are considered negligible [37]. Then, the dynamics of the resonator is governed by the following (SDOF) model

$$M \ddot{x}(t) + C \dot{x}(t) + K x(t) = F(t) \tag{5.5}$$

where $x(t)$ is the inward displacement of the air at the neck and $F(t)$ is the external force exerted by the pressure oscillations outside of the neck.

It is important note that nonlinearities become dominant if the airflow has a non-negligible Mach number as clearly pointed out in [36]. In such cases the simple linear mechanical vibration absorber analogy and (5.5) may not hold anymore and nonlinear analysis may be required as in [80]. In this study; however, the focus is on the airflow created only by natural buoyancy, and with negligible Mach number (see the assumptions listed in Section 3.1) This feature is necessary in adopting the linearized dynamics given in (5.5).

5.1.2 Resonator effect when attached to a Rijke tube

The acoustic impedance of a Helmholtz resonator attached to a duct can be derived using (5.5) as

$$Z_r(s) = \frac{\tilde{P}_r(s)}{S_n \tilde{U}_r(s)} = \frac{1}{S_n^2} \frac{F(s)}{sX(s)} = \frac{1}{S_n^2} \frac{Ms^2 + Cs + K}{s} \tag{5.6}$$

in the Laplace domain. Here $\tilde{P}_r(s)$ and $\tilde{U}_r(s)$ represent the pressure and air velocity fluctuations just outside the resonator neck, respectively. At the interface of the resonator and the cross-sections ④ and ⑤ in Figure 5.2, the following set of equations hold for pressure and velocity fluctuations in time domain

$$\begin{aligned} \tilde{p}_4(t) &= \tilde{p}_5(t) = \tilde{p}_r(t) \\ A\tilde{u}_4(t) &= A\tilde{u}_5(t) + S_n \tilde{u}_r(t) \end{aligned} \tag{5.7}$$

where A is the cross-sectional area of the tube. Substituting (3.6) and (3.7) in (5.7) and taking its Laplace transform one obtains

$$\begin{aligned} F_4(s) + G_4(s) &= F_5(s) + G_5(s) \\ F_4(s) - G_4(s) &= F_5(s) - G_5(s) + \left[F_4(s) + G_4(s)\right] \overline{\rho c} / A Z_r(s) \end{aligned} \tag{5.8}$$

The set of equations above are combined in the following form

$$\begin{pmatrix} G_4(s) \\ F_5(s) \end{pmatrix} = \mathbf{H}_r \begin{pmatrix} F_4(s) \\ G_5(s) \end{pmatrix}, \quad \mathbf{H}_r = \frac{1}{s^2 + (C_r + T_r)s + \Omega_r^2} \begin{bmatrix} -T_r s & s^2 + C_r s + \Omega_r^2 \\ s^2 + C_r s + \Omega_r^2 & -T_r s \end{bmatrix} \tag{5.9}$$

where $\mathbf{H}_r$ is the resonator transfer matrix, $C_r = C/M$, $\Omega_r = \sqrt{K/M}$ and $T_r = S_n^2 \overline{\rho c}/(2MA)$.

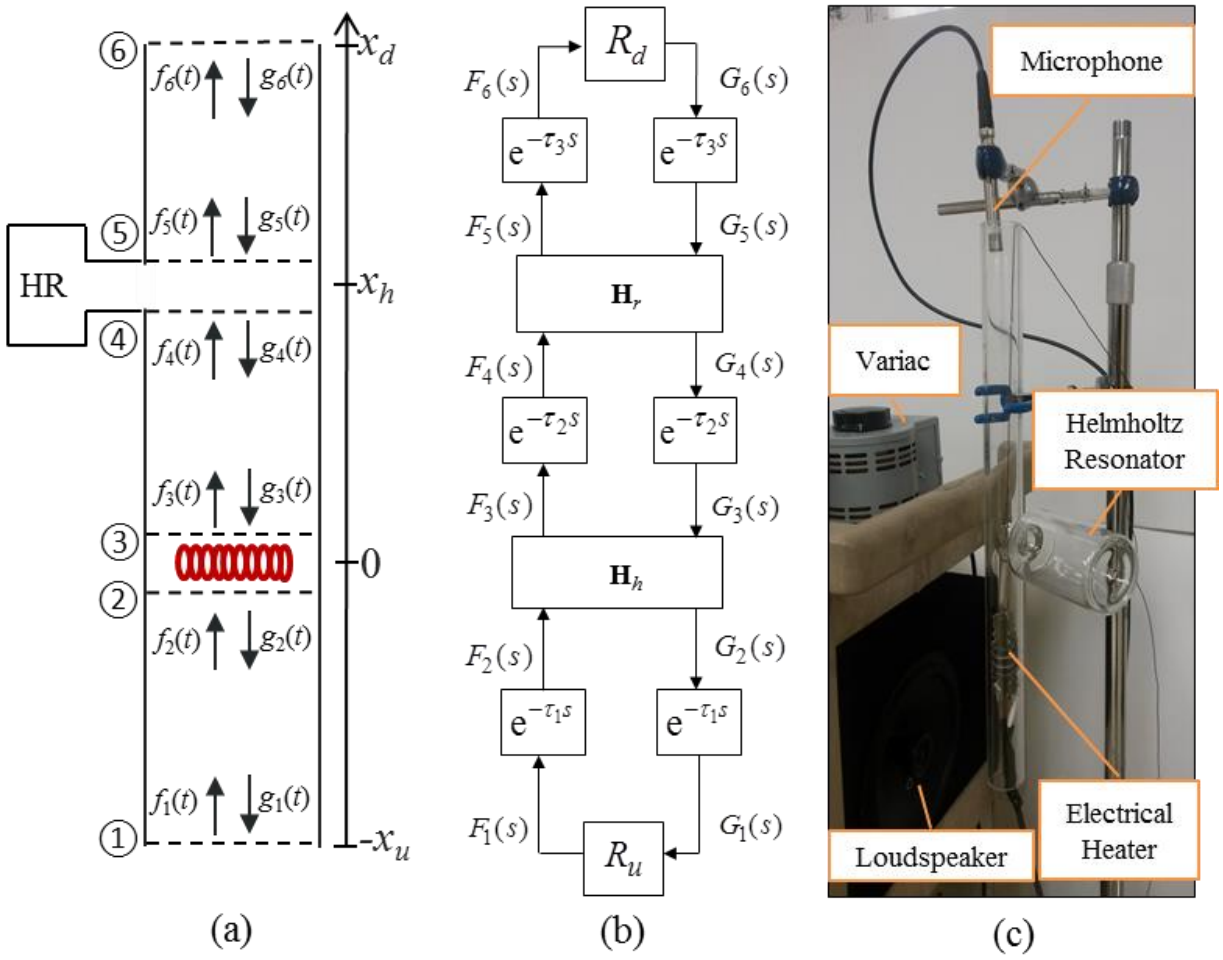

Figure 5.2 (a) Functional sketch of a Rijke tube with Helmholtz resonator, (b) its block diagram and (c) the experimental Rijke tube setup.

5.2 Rijke Tube Dynamics with a Helmholtz Resonator: A State-space Approach

The thermoacoustic dynamics within the Rijke tube is studied in Chapter 3 and extended with a feedback control loop in Chapter 4. Here, the Rijke tube model with a Helmholtz resonator is derived in state-space form. Similar to the developments in the earlier chapters, the acoustic waves are represented by $f_i(t)$ and $g_i(t)$, $i = 1,..., 6$ in Figure 5.2a at different cross-sections denoted by the subscript *i*. As seen in the block diagram in Figure 5.2b, the travel times of the acoustic waves along the duct contribute to the system dynamics as time delays

$$\tau_1 = x_u / \bar{c}\,, \quad \tau_2 = x_h / \bar{c}\,, \quad \tau_3 = (x_d - x_h)/\bar{c} \tag{5.10}$$

where $x_u + x_d = L$, and L is the length of the tube. Note that the average (mean) flow quantities such as density $\bar{\rho}$ and the speed of sound $\bar{c}$ are assumed as constant along the tube.

The dynamics at the heating zone $(x = 0)$ is represented by a transfer matrix $\mathbf{H}_h \in \Re^{2\times 2}$ between the incoming and outgoing acoustic waves [see (3.16)]. The input and output vectors may be defined as $\mathbf{U}_h(s) = [F_2(s) \quad G_3(s)]^{\mathrm{T}} \in \Re^2$ and $\mathbf{Y}_h(s) = [G_2(s) \quad F_3(s)]^{\mathrm{T}} \in \Re^2$ respectively, which yield $\mathbf{Y}_h(s) = \mathbf{H}_h \mathbf{U}_h(s)$. $\mathbf{H}_h \in \Re^{2\times 2}$ matrix can be rewritten in the following form

$$\mathbf{H}_h = \frac{1}{s + Z_1 + Z_2}\begin{bmatrix} Z_1 & s + Z_2 \\ s + 2Z_1 + Z_2 & -Z_1 \end{bmatrix} \tag{5.11}$$

where $Z_1 = a(\gamma - 1)/(2Ab\bar{c}^2\bar{\rho})$ and $Z_2 = 1/b$. In these expressions, γ represents the heat capacity ratio, a is the gain of the heat release dynamics proportional to the mean heat release rate and b is the time constant of the heat release dynamics as explained in Chapter 3. This leads to the following relation in time domain

$$\dot{\mathbf{y}}_h(t) + \mathbf{S}\mathbf{y}_h(t) = \mathbf{M}\dot{\mathbf{u}}_h(t) + \mathbf{N}\mathbf{u}_h(t) \tag{5.12}$$

where $\mathbf{u}_h(t) = \begin{bmatrix} f_2(t) & g_3(t) \end{bmatrix}^{\mathrm{T}} \in \Re^2$, $\mathbf{y}_h(t) = \begin{bmatrix} g_2(t) & f_3(t) \end{bmatrix}^{\mathrm{T}} \in \Re^2$, $\mathbf{S} = (Z_1 + Z_2)\mathbf{I}_2$, $\mathbf{M} = \begin{bmatrix} 0 & 1 \\ 1 & 0 \end{bmatrix}$, $\mathbf{N} = \begin{bmatrix} Z_1 & Z_2 \\ 2Z_1 + Z_2 & -Z_1 \end{bmatrix}$ and $\mathbf{I}_2$ represents the 2×2 identity matrix.

The resonator transfer matrix $\mathbf{H}_r \in \Re^{2\times 2}$ at $(x = x_h)$ connects the incoming acoustic waves $\mathbf{U}_r(s) = \begin{bmatrix} F_4(s) & G_5(s) \end{bmatrix}^{\mathrm{T}} \in \Re^2$ to the outgoing acoustic waves $\mathbf{Y}_r(s) = \begin{bmatrix} G_4(s) & F_5(s) \end{bmatrix}^{\mathrm{T}} \in \Re^2$ as $\mathbf{Y}_r(s) = \mathbf{H}_r\mathbf{U}_r(s)$. In time domain this relation becomes

$$\ddot{\mathbf{y}}_r(t) + \mathbf{V}\dot{\mathbf{y}}_r(t) + \mathbf{Q}\mathbf{y}_r(t) = \mathbf{M}\ddot{\mathbf{u}}_r(t) + \mathbf{J}\dot{\mathbf{u}}_r(t) + \mathbf{W}\mathbf{u}_r(t) \tag{5.13}$$

where $\mathbf{u}_r(t) = \begin{bmatrix} f_4(t) & g_5(t) \end{bmatrix}^{\mathrm{T}} \in \Re^2$, $\mathbf{y}_r(t) = \begin{bmatrix} g_4(t) & f_5(t) \end{bmatrix}^{\mathrm{T}} \in \Re^2$, and the 2×2 matrices are $\mathbf{V} = (C_r + T_r)\mathbf{I}_2$, $\mathbf{Q} = \Omega_r^2\mathbf{I}_2$, $\mathbf{J} = \begin{bmatrix} -T_r & C_r \\ C_r & -T_r \end{bmatrix}$, $\mathbf{W} = \Omega_r^2\mathbf{M}$.

At both tube ends, reflection of the acoustic waves is represented by the reflection coefficients R_u and R_d in Figure 5.2b. Utilizing the reflection coefficients R_u, R_d at the tube ends and the time delays in (5.10), the input vectors $\mathbf{u}_h(t) \in \Re^2$ and $\mathbf{u}_r(t) \in \Re^2$ in (3.16) and (5.9) can be expressed as

$$\begin{aligned} \mathbf{u}_h(t) &= \mathbf{R}_1\mathbf{y}_h(t - 2\tau_1) + \mathbf{L}_1\mathbf{y}_r(t - \tau_2) \\ \mathbf{u}_r(t) &= \mathbf{L}_2\mathbf{y}_h(t - \tau_2) + \mathbf{R}_2\mathbf{y}_r(t - 2\tau_3) \end{aligned} \tag{5.14}$$

where $\mathbf{R}_1 = \begin{bmatrix} R_u & 0 \\ 0 & 0 \end{bmatrix}$, $\mathbf{R}_2 = \begin{bmatrix} 0 & 0 \\ 0 & R_d \end{bmatrix}$, $\mathbf{L}_1 = \begin{bmatrix} 0 & 0 \\ 1 & 0 \end{bmatrix}$ and $\mathbf{L}_2 = \begin{bmatrix} 0 & 1 \\ 0 & 0 \end{bmatrix}$. Substituting (5.14) in (5.12) and (5.13), one obtains

$$\dot{\mathbf{y}}_h(t)+\overline{\mathbf{A}}\dot{\mathbf{y}}_h(t-2\tau_1)+\overline{\mathbf{B}}\dot{\mathbf{y}}_r(t-\tau_2)=\overline{\mathbf{C}}\mathbf{y}_h(t)+\overline{\mathbf{D}}\mathbf{y}_h(t-2\tau_1)+\overline{\mathbf{E}}\mathbf{y}_r(t-\tau_2)$$
$$\ddot{\mathbf{y}}_r(t)+\hat{\mathbf{A}}\ddot{\mathbf{y}}_r(t-2\tau_3)+\hat{\mathbf{B}}\ddot{\mathbf{y}}_h(t-\tau_2)=\hat{\mathbf{C}}\dot{\mathbf{y}}_r(t)+\hat{\mathbf{D}}\dot{\mathbf{y}}_r(t-2\tau_3)+\hat{\mathbf{E}}\dot{\mathbf{y}}_h(t-\tau_2)+\hat{\mathbf{F}}\mathbf{y}_r(t)+\hat{\mathbf{G}}\mathbf{y}_r(t-2\tau_3)+\hat{\mathbf{H}}\mathbf{y}_h(t-\tau_2) \quad (5.15)$$

where $\overline{\mathbf{A}}=-\mathbf{M}\mathbf{R}_1$, $\overline{\mathbf{B}}=-\mathbf{M}\mathbf{L}_1$, $\overline{\mathbf{C}}=-\mathbf{S}$, $\overline{\mathbf{D}}=\mathbf{N}\mathbf{R}_1$, $\overline{\mathbf{E}}=\mathbf{N}\mathbf{L}_1$, $\hat{\mathbf{A}}=-\mathbf{M}\mathbf{R}_2$, $\hat{\mathbf{B}}=-\mathbf{M}\mathbf{L}_2$, $\hat{\mathbf{C}}=-\mathbf{V}$, $\hat{\mathbf{D}}=\mathbf{J}\mathbf{R}_2$, $\hat{\mathbf{E}}=\mathbf{J}\mathbf{L}_2$, $\hat{\mathbf{F}}=-\mathbf{Q}$, $\hat{\mathbf{G}}=\mathbf{W}\mathbf{R}_2$, $\hat{\mathbf{H}}=\mathbf{W}\mathbf{L}_2$ are all 2×2 matrices. Taking the derivative of the first equation in (5.15), a new equation set both with second order dynamics can be obtained as

$$\ddot{\mathbf{y}}_h(t)+\overline{\mathbf{A}}\ddot{\mathbf{y}}_h(t-2\tau_1)+\overline{\mathbf{B}}\ddot{\mathbf{y}}_r(t-\tau_2)=\overline{\mathbf{C}}\dot{\mathbf{y}}_h(t)+\overline{\mathbf{D}}\dot{\mathbf{y}}_h(t-2\tau_1)+\overline{\mathbf{E}}\dot{\mathbf{y}}_r(t-\tau_2)$$
$$\ddot{\mathbf{y}}_r(t)+\hat{\mathbf{A}}\ddot{\mathbf{y}}_r(t-2\tau_3)+\hat{\mathbf{B}}\ddot{\mathbf{y}}_h(t-\tau_2)=\hat{\mathbf{C}}\dot{\mathbf{y}}_r(t)+\hat{\mathbf{D}}\dot{\mathbf{y}}_r(t-2\tau_3)+\hat{\mathbf{E}}\dot{\mathbf{y}}_h(t-\tau_2)+\hat{\mathbf{F}}\mathbf{y}_r(t)+\hat{\mathbf{G}}\mathbf{y}_r(t-2\tau_3)+\hat{\mathbf{H}}\mathbf{y}_h(t-\tau_2) \quad (5.16)$$

Note that this step introduces some artificial dynamics into the system (i.e., some additional characteristic roots at the origin), which will be discussed later in the text. The new set of equations appears as

$$\begin{aligned}&\ddot{\mathbf{y}}(t)+\mathbf{P}_1\ddot{\mathbf{y}}(t-2\tau_1)+\mathbf{P}_2\ddot{\mathbf{y}}(t-\tau_2)+\mathbf{P}_3\ddot{\mathbf{y}}(t-2\tau_3)=\\&\mathbf{P}_4\dot{\mathbf{y}}(t)+\mathbf{P}_5\dot{\mathbf{y}}(t-2\tau_1)+\mathbf{P}_6\dot{\mathbf{y}}(t-\tau_2)+\mathbf{P}_7\dot{\mathbf{y}}(t-2\tau_3)+\mathbf{P}_8\mathbf{y}(t)+\mathbf{P}_9\mathbf{y}(t-\tau_2)+\mathbf{P}_{10}\mathbf{y}(t-2\tau_3)\end{aligned} \quad (5.17)$$

where $\mathbf{y}(t)=\begin{bmatrix}\mathbf{y}_h(t) & \mathbf{y}_r(t)\end{bmatrix}^{\mathrm{T}}\in\Re^4$, $\mathbf{P}_1=\begin{bmatrix}\overline{\mathbf{A}} & \mathbf{0}_2\\ \mathbf{0}_2 & \mathbf{0}_2\end{bmatrix}$, $\mathbf{P}_2=\begin{bmatrix}\mathbf{0}_2 & \overline{\mathbf{B}}\\ \hat{\mathbf{B}} & \mathbf{0}_2\end{bmatrix}$, $\mathbf{P}_3=\begin{bmatrix}\mathbf{0}_2 & \mathbf{0}_2\\ \mathbf{0}_2 & \hat{\mathbf{A}}\end{bmatrix}$, $\mathbf{P}_4=\begin{bmatrix}\overline{\mathbf{C}} & \mathbf{0}_2\\ \mathbf{0}_2 & \hat{\mathbf{C}}\end{bmatrix}$, $\mathbf{P}_5=\begin{bmatrix}\overline{\mathbf{D}} & \mathbf{0}_2\\ \mathbf{0}_2 & \mathbf{0}_2\end{bmatrix}$, $\mathbf{P}_6=\begin{bmatrix}\mathbf{0}_2 & \overline{\mathbf{E}}\\ \hat{\mathbf{E}} & \mathbf{0}_2\end{bmatrix}$, $\mathbf{P}_7=\begin{bmatrix}\mathbf{0}_2 & \mathbf{0}_2\\ \mathbf{0}_2 & \hat{\mathbf{D}}\end{bmatrix}$, $\mathbf{P}_8=\begin{bmatrix}\mathbf{0}_2 & \mathbf{0}_2\\ \mathbf{0}_2 & \hat{\mathbf{F}}\end{bmatrix}$, $\mathbf{P}_9=\begin{bmatrix}\mathbf{0}_2 & \mathbf{0}_2\\ \hat{\mathbf{H}} & \mathbf{0}_2\end{bmatrix}$, $\mathbf{P}_{10}=\begin{bmatrix}\mathbf{0}_2 & \mathbf{0}_2\\ \mathbf{0}_2 & \hat{\mathbf{G}}\end{bmatrix}$.

Here, $\mathbf{0}_2$ represents a 2×2 zero matrix and all $\mathbf{P}_j$, $j=1,2,...,10$ matrices are 4×4. Finally, selecting the state vector as $\mathbf{x}(t)=\begin{bmatrix}\mathbf{x}_1(t) & \mathbf{x}_2(t)\end{bmatrix}^{\mathrm{T}}=\begin{bmatrix}\mathbf{y}(t) & \dot{\mathbf{y}}(t)\end{bmatrix}^{\mathrm{T}}\in\Re^8$, the state space representation of the overall dynamics is obtained as

$$\dot{\mathbf{x}}(t)+\mathbf{H}_1\dot{\mathbf{x}}(t-2\tau_1)+\mathbf{H}_2\dot{\mathbf{x}}(t-\tau_2)+\mathbf{H}_3\dot{\mathbf{x}}(t-2\tau_3)=\mathbf{T}_0\mathbf{x}(t)+\mathbf{T}_1\mathbf{x}(t-2\tau_1)+\mathbf{T}_2\mathbf{x}(t-\tau_2)+\mathbf{T}_3\mathbf{x}(t-2\tau_3) \quad (5.18)$$

where $\mathbf{H}_1 = \begin{bmatrix} \mathbf{0}_4 & \mathbf{0}_4 \\ \mathbf{0}_4 & \mathbf{P}_1 \end{bmatrix}$, $\mathbf{H}_2 = \begin{bmatrix} \mathbf{0}_4 & \mathbf{0}_4 \\ \mathbf{0}_4 & \mathbf{P}_2 \end{bmatrix}$, $\mathbf{H}_3 = \begin{bmatrix} \mathbf{0}_4 & \mathbf{0}_4 \\ \mathbf{0}_4 & \mathbf{P}_3 \end{bmatrix}$, $\mathbf{T}_0 = \begin{bmatrix} \mathbf{0}_4 & \mathbf{I}_4 \\ \mathbf{P}_8 & \mathbf{P}_4 \end{bmatrix}$, $\mathbf{T}_1 = \begin{bmatrix} \mathbf{0}_4 & \mathbf{0}_4 \\ \mathbf{0}_4 & \mathbf{P}_5 \end{bmatrix}$,

$\mathbf{T}_2 = \begin{bmatrix} \mathbf{0}_4 & \mathbf{0}_4 \\ \mathbf{P}_9 & \mathbf{P}_6 \end{bmatrix}$, $\mathbf{T}_3 = \begin{bmatrix} \mathbf{0}_4 & \mathbf{0}_4 \\ \mathbf{P}_{10} & \mathbf{P}_7 \end{bmatrix}$ are all 8×8 matrices.

5.3 Passive Stabilization with Experiments

In this section, a Rijke tube in unstable operating conditions is taken and it is attempted to be stabilized by attaching a Helmholtz resonator. First the CTCR theory is implemented on the mathematical model developed in Section 5.2 to obtain an exhaustive stability map in the parametric space. The analytical findings from this stage are then compared with the experimental results. Separately, case studies are performed where the resonator's stabilization effect under stronger thermoacoustic coupling is investigated.

The experimental set-up is formed around a glass tube with an electrical heating element as shown in Figure 5.2c. The heater is driven with constant power using a variac. A bottle shaped glass acoustic cavity is used as a Helmholtz resonator. A microphone at the downstream end of the tube records the pressure fluctuations. A loudspeaker is deployed to provide a disturbance noise to the set-up in order to investigate the system characteristics.

5.3.1 Instability without the resonator

First the stability of a plain Rijke tube, without any Helmholtz resonator is analyzed. This particular case was studied in Chapter 3 with several tubes. Following the developed mathematical model in Section 5.2, in the absence of a Helmholtz resonator, the thermoacoustic dynamics in the Rijke tube is simply governed by (5.12) and

$$\mathbf{u}_h(t) = \mathbf{R}_1 \mathbf{y}_h(t - 2\tau_1) + \mathbf{R}_2 \mathbf{y}_h(t - 2\tau_2 - 2\tau_3), \quad \mathbf{u}_h(t) \in \Re^2 \tag{5.19}$$

Once (5.12) and (5.19) are combined, a state space representation of plain Rijke tube can be obtained as

$$\dot{\mathbf{y}}_h(t) + \overline{\mathbf{A}}\mathbf{y}_h(t-2\tau_1) + \hat{\mathbf{A}}\mathbf{y}_h(t-2\tau_2-2\tau_3) = \overline{\mathbf{C}}\mathbf{y}_h(t) + \overline{\mathbf{D}}\mathbf{y}_h(t-2\tau_1) + \overline{\mathbf{F}}\mathbf{y}_h(t-2\tau_2-2\tau_3), \quad \mathbf{y}_h(t) \in \Re^2 \tag{5.20}$$

where $\overline{\mathbf{F}} = \mathbf{N}\mathbf{R}_2$ and the remaining matrices are as defined in the previous section. Over this dynamics, the condition in Theorem 2.2 should be checked first. Substituting the operational parameters in Table 5.1 in (5.20), the characteristic quasi-polynomial of the associated difference equation is obtained as

$$D(s,\tau_1,\tau_2,\tau_3) = \det[(\mathbf{I}_2 + \overline{\mathbf{A}}e^{-2\tau_1 s} + \hat{\mathbf{A}}e^{-2(\tau_2+\tau_3)s}] = 1 - 0.865e^{-2(\tau_1+\tau_2+\tau_3)s} = 0 \tag{5.21}$$

where $|e^{-2(\tau_1+\tau_2+\tau_3)s}| = 1/0.865 > 1$ implying $\mathrm{Re}(s) < 0$. That is, all the infinitely many characteristic roots of (5.21) are located on the left half of the complex plane. Thus (5.21) is stable for any delay composition. In the next step to completely assess the stability of the neutral system given by (5.20), the entire characteristic equation is considered with the operations parameters in Table 5.1.

$$CE(s,\tau_1,\tau_2,\tau_3) = \det[s(\mathbf{I}_2 + \overline{\mathbf{A}}e^{-2\tau_1 s} + \hat{\mathbf{A}}e^{-2(\tau_2+\tau_3)s}) - (\overline{\mathbf{C}} + \overline{\mathbf{D}}e^{-2\tau_1 s} + \overline{\mathbf{F}}e^{-2(\tau_2+\tau_3)s})] = 0 \tag{5.22}$$

which, interestingly, yields a factored form as

$$CE(s,\tau_1,\tau_2,\tau_3) = CE_1(s) \times CE_2(s,\tau_1,\tau_2,\tau_3) = 0 \tag{5.23}$$

where $CE_1(s) = s + 704.0 = 0$ and

$$\begin{aligned} CE_2(s,\tau_1,\tau_2,\tau_3) &= (1 - 0.865e^{-2(\tau_1+\tau_2+\tau_3)s})s + 704.0 + 189.7e^{-2\tau_1 s} \\ &- 189.7e^{-2(\tau_2+\tau_3)s} - 608.9e^{-2(\tau_1+\tau_2+\tau_3)s} = 0 \end{aligned} \tag{5.24}$$

$CE_1(s)$ has a stationary root at $s = -704.0$, therefore does not affect the stability of the system. On the other hand $CE_2(s,\tau_1,\tau_2,\tau_3)$ presents delay-dependent stability characteristics. To obtain the relevant stability map in the parametric space of $(L, x_u) \in \Re^{2+}$ the CTCR paradigm is deployed on (5.24). The

outcome is given as the kernel in Figure 5.3a. The corresponding imaginary root frequency variations on this kernel hypercurve are presented in Figure 5.3b.

In Figure 5.3a, the kernel hypercurve is colored in red and the stable region is shaded in grey. No offspring hypercurve exists in the parameter range depicted in this figure. The physically infeasible region, where $x_u > L$ is shown with crosshatch. The thick black line corresponds to our experimental tube length, $L = 0.508\,\mathrm{m}$. The '×' markers on this line represent the settings at which instability is observed experimentally. The 'o' markers, on the other hand, represent the tests resulting in stable operation. In the next set of tests, the focus will be on the stabilization of an unstable Rijke tube with a Helmholtz resonator.

Table 5.1 Operational parameters for the Helmholtz resonator mounted Rijke tube experiment.

Parameter	Value	Unit
R_u	-0.93	-
R_d	-0.93	-
γ	1.4	-
A	7.07×10^{-4}	m^2
L	0.508	m
$\overline{\rho}$	1.2	kg/m^3
$\overline{c}$	340	m/s
a	200	-
b	0.002	-
S_n	2.27×10^{-4}	m^2
V	2.65×10^{-4}	m^3
l_n	0.025	m

5.3.2 Resonator impact on thermoacoustic instability

For passive control of thermoacoustic instability in the unstable Rijke tube, a Helmholtz resonator with a natural frequency different than the observed frequency of instability is chosen. As seen in Figure 5.3b, the sound pressure frequency at the stability boundary corresponding to our tube length is 337.7 Hz. Note

that this is not the frequency of an unstable system with an x_u value inside the unstable region (for instance at point **A**), but the transition frequency for another x_u. On the other hand, the Helmholtz resonator used in the experiments (with design parameters in Table 5.1) exhibits a natural frequency of 252.14 Hz. This combination creates a scenario where the vibration absorber is not perfectly tuned, therefore where it is placed along the duct plays a very important role for stabilization purposes.

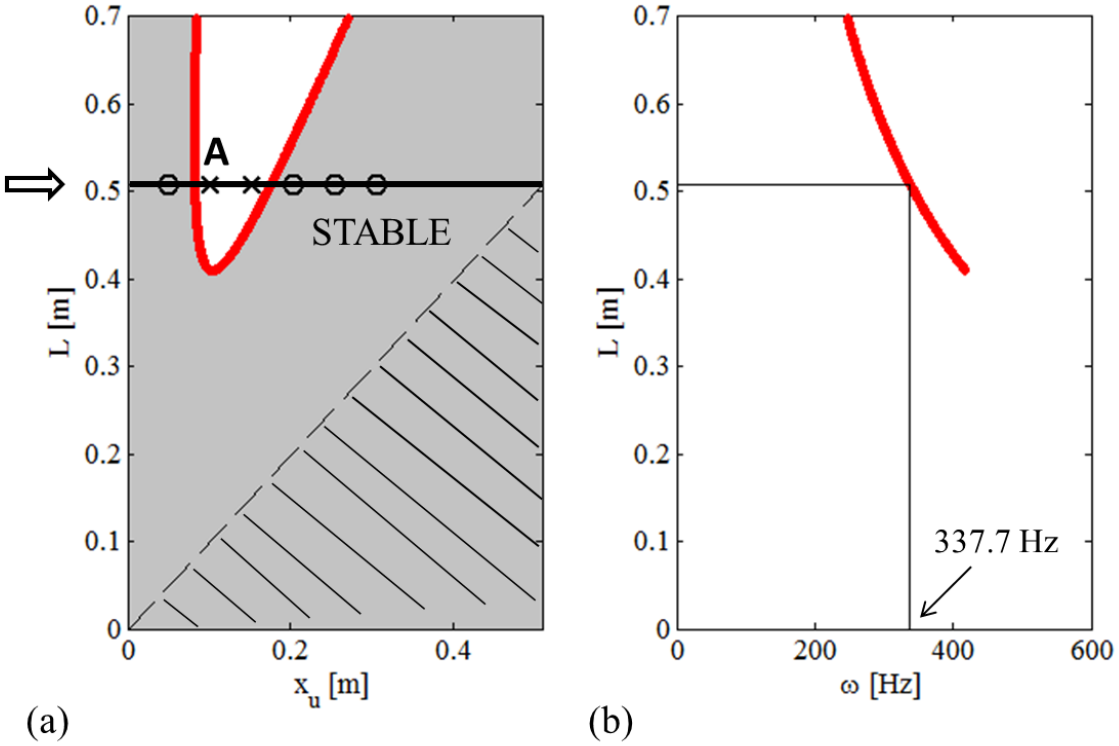

Figure 5.3 (a) Stability map of the Rijke tube with no Helmholtz resonator and (b) its frequency information.

To analyze the stability of the resonator mounted Rijke tube that is governed by (5.18), first Theorem 2.2 is checked, again by calculating the characteristic quasi-polynomial of the associated difference equation

$$D(s,\tau_1,\tau_2,\tau_3)=\det[\mathbf{I}_8+\mathbf{H}_1e^{-2\tau_1 s}+\mathbf{H}_2e^{-\tau_2 s}+\mathbf{H}_3e^{-2\tau_3 s}]=1-0.865e^{-2(\tau_1+\tau_2+\tau_3)s}=0 \tag{5.25}$$

which is identical to (5.22). Therefore (5.25) is deemed stable for any delay composition. Next, the characteristic equation of (5.18) is considered as

$$CE(s,\tau_1,\tau_2,\tau_3)=\det[s(\mathbf{I}_8+\mathbf{H}_1e^{-2\tau_1 s}+\mathbf{H}_2e^{-\tau_2 s}+\mathbf{H}_3e^{-2\tau_3 s})-\mathbf{T}_0-\mathbf{T}_1e^{-2\tau_1 s}-\mathbf{T}_2e^{-\tau_2 s}-\mathbf{T}_3e^{-2\tau_3 s}]=0 \tag{5.26}$$

which again yields an interesting factorization as

$$CE(s,\tau_1,\tau_2,\tau_3)=CE_3(s)\times CE_4(s,\tau_1,\tau_2,\tau_3)=0 \tag{5.27}$$

this time with a fifth degree polynomial factor as $CE_3(s)=s^2(s+704.0)(s^2+1390.5s+2.51\times10^6)$ and the remaining factor in (5.27) becomes

$$\begin{aligned}CE_4(s,\tau_1,\tau_2,\tau_3)&=(1-0.865e^{-2(\tau_1+\tau_2+\tau_3)s})s^3+(2094.0+189.7e^{-2\tau_1 s}-189.7e^{-2(\tau_2+\tau_3)s}\\&-1287.0e^{-2(\tau_1+\tau_2)s}-1287.0e^{-2\tau_3 s}+582.1e^{-2(\tau_1+\tau_2+\tau_3)s})s^2+(3.49\times10^6+2.64\times10^5\,e^{-2\tau_1 s}\\&-2.82\times10^5\,e^{-2\tau_2 s}-9.06\times10^5\,e^{-2\tau_3 s}-9.06\times10^5\,e^{-2(\tau_1+\tau_2)s}-2.44\times10^5\,e^{-2(\tau_1+\tau_3)s}\\&+2.61\times10^5\,e^{-2(\tau_2+\tau_3)s}-1.33\times10^6\,e^{-2(\tau_1+\tau_2+\tau_3)s})s+1.77\times10^9+4.76\times10^8\,e^{-2\tau_1 s}\\&-4.76\times10^8\,e^{-2(\tau_2+\tau_3)s}-1.53\times10^9e^{-2(\tau_1+\tau_2+\tau_3)s}=0\end{aligned} \tag{5.28}$$

Notice that $CE_3(s)$ has two roots at the origin. These roots are, in fact, artificially introduced into the dynamics due to the derivative operation which was performed on the first equation in (5.15) (see Section 5.2). Therefore, in the remainder of the text this root pair at the origin will be disregarded. The rest of the roots of $CE_3(s)$ are $s_1=-704.0$, $s_{2,3}=-695.3\pm1423.6\mathrm{i}$, which are stationary and they have $\mathrm{Re}(s)<0$. For the delay dependent stability analysis $CE_4(s,\tau_1,\tau_2,\tau_3)$ is considered. Considering the fact that $L=\bar{c}(\tau_1+\tau_2+\tau_3)$ is fixed in the experiment, and defining $x_r=x_d-x_h$, the stability map corresponding to the characteristic equation in (5.28) is obtained in the parametric space of $(x_r,x_u)=\bar{c}(\tau_3,\tau_1)\in\Re^{2+}$ utilizing the CTCR paradigm. It is given in Figure 5.4a.

In Figure 5.4a, the kernel and offspring hypercurves are colored in red and blue, respectively. The stable region is shaded grey and the physically infeasible region, where $x_u + x_r > L$ is marked with a cross-hatch. The thick black line represents $x_r = 0$, namely the resonator is positioned at the end of the tube. As such it does not participate in the dynamics of the tube at all. That means the outcome of this setting should be identical to the case in Figure 5.3a without Helmholtz resonator. Notations remain unchanged, as the '×' markers denote unstable, whereas 'o' markers represent stable operations. The match between the analytical and experimental results is not perfect; however, they represent similar trends in distribution. The analytical findings seem to be more conservative in predicting the stable zones, which implies that the resonator dynamics is more damped in the experiment than it is analytically predicted. Better results could have been obtained if the damping characteristics are perfectly identified; however, this requires additional experimental capabilities [36] and is a topic of future study.

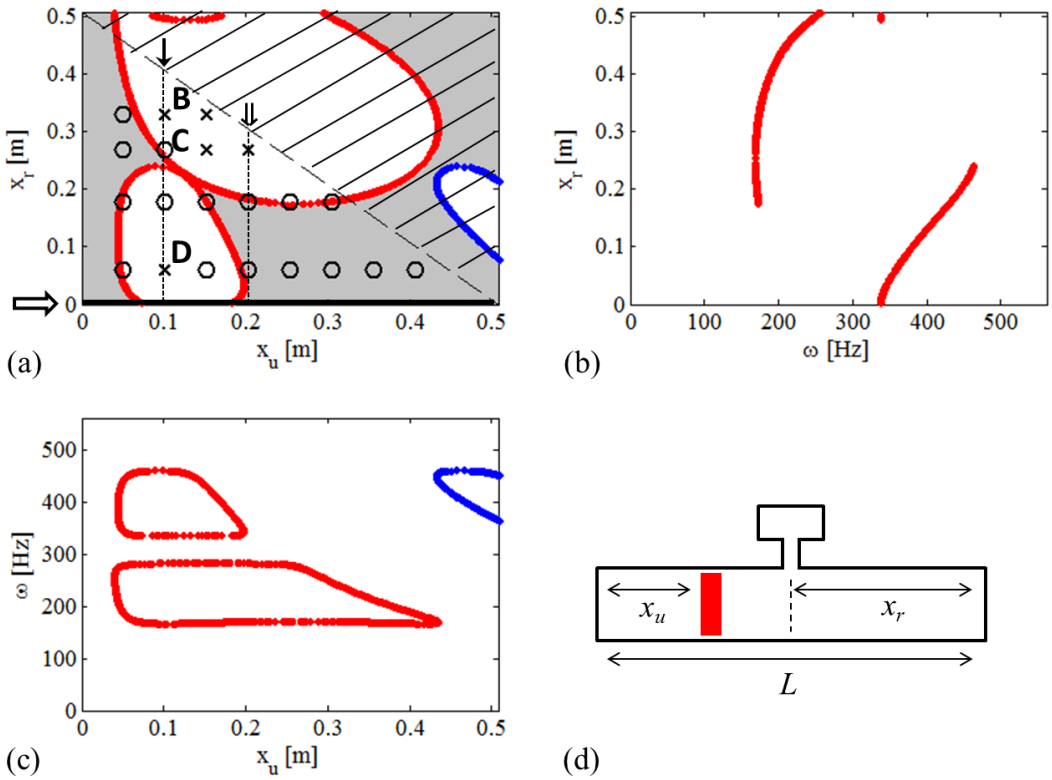

Figure 5.4 (a) Stability map of Rijke tube with a Helmholtz resonator, (b) x_r vs. ω variations, (c) ω vs. x_u variations, (d) a schematic of x_u and x_r definitions on the Rijke tube.

Careful observation of Figure 5.4a reveals that the plain Rijke tube which is unstable could be stabilized by properly positioning the resonator (see vertical dashed line marked by "↓"). In contrast, for some heater positions that lead to stable operations in the plain tube, it is possible to destabilize the system when the resonator is improperly mounted at certain points (see vertical line marked by "⇓"). Very similar findings have already been published in [11], where it is experimentally shown that certain resonator placements may result in amplification while others cause suppression of pressure oscillations.

Figure 5.4b and Figure 5.4c display the complete set of frequency intervals at which stability to instability crossover can be can be observed depending on the resonator (Figure 5.4b) and heater (Figure 5.4c) locations. To investigate the frequency characteristics of the system further, some specific test results are discussed next. The time traces of pressure oscillations during the experimental runs at points **A**, **B** and **D** in Figure 5.3a and Figure 5.4a are shown in Figure 5.5a. To extract the frequency information during these tests, fast fourier transform (FFT) of the signals at the onset of instabilities are performed as shown in Figure 5.5b.

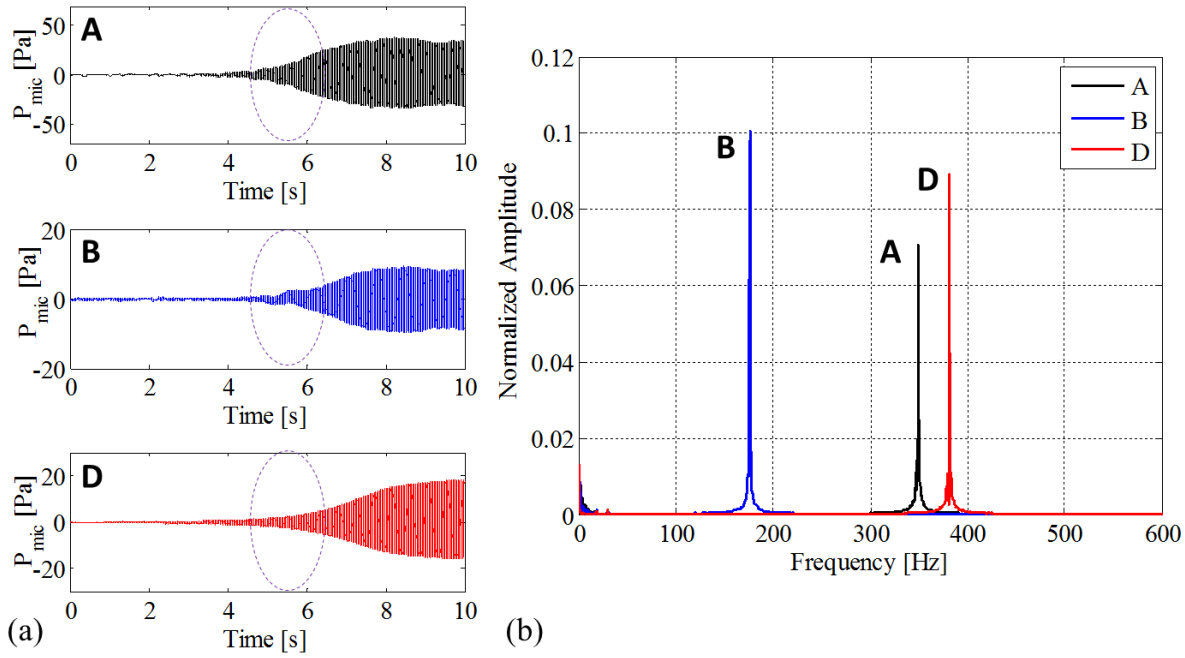

Figure 5.5 (a) Unstable pressure oscillations during experimental tests, (b) FFT information at the onset of instability.

At point **C** in Figure 5.4a, the stability map predicts instability, however, the experimental test at this setting results in a stable operation. To extract the frequency information at this setting, a white noise input is deployed through the loudspeaker at the upstream end of the tube and the pressure oscillations within the tube are recorded. Right after the white noise input ends, an FFT analysis is performed on the recorded decaying pressure fluctuations. The time trace of the ensuing pressure and the FFT results are shown in Figure 5.6a and Figure 5.6b.

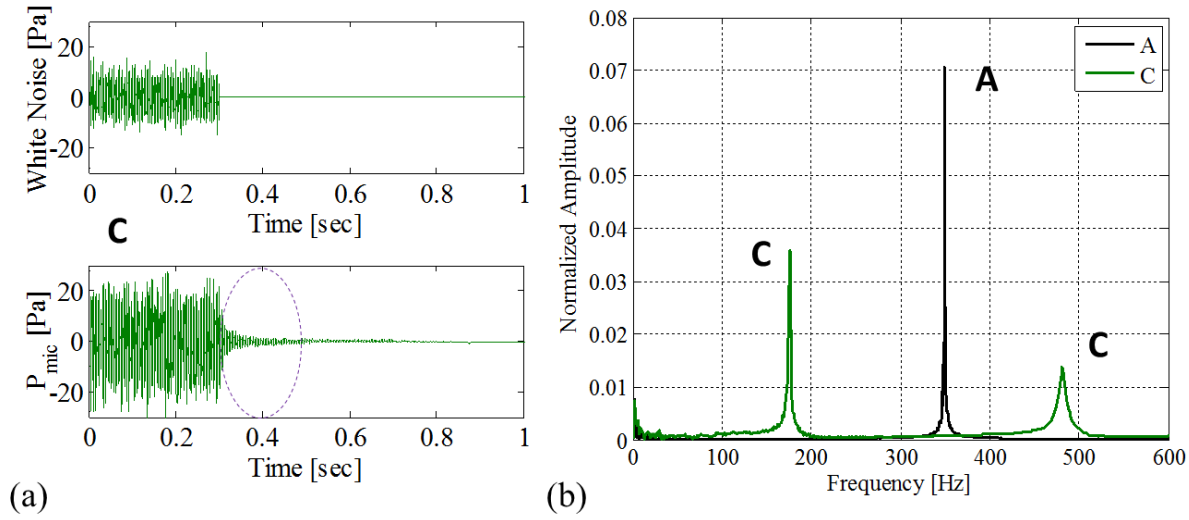

Figure 5.6 (a) White noise test at a stable operating point, (b) the corresponding FFT result.

In Figure 5.6b, the *frequency splitting* phenomenon is observed very clearly, when the sensitive frequencies of the plain Rijke tube (**A**) and the resonator mounted Rijke tube (**C**) are compared. This is akin to the case that occurs when a SDOF mechanical vibration absorber is attached to a plant. The new system does not respond at the original frequency but it becomes sensitized at two neighboring and additional side frequencies [34].

To compare the experimentally detected frequencies in Figure 5.5b and Figure 5.6b with those frequencies that are extracted from the corresponding mathematical models, QPmR algorithm is utilized. Deploying QPmR on (5.24) for point **A** and on (5.28) for points **B**, **C** and **D**, the characteristic root locations are determined as shown in Figure 5.7a and b.

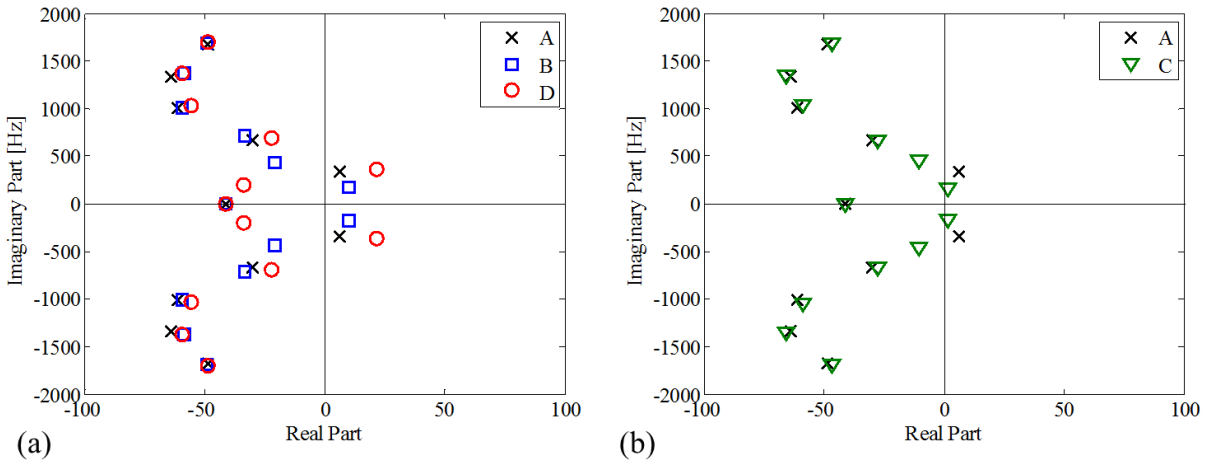

Figure 5.7 Characteristic Roots of the system at the operating points (a) **A**, **B**, **D** and (b) **A**, **C** in Figure 5.3a and Figure 5.4a.

The frequencies which are obtained from the experiments and the mathematical models are compared in Table 5.2. The relative errors are all minor, indicating that the mathematical model at hand captures the frequencies with desirable fidelity.

Table 5.2 Comparison of detected frequencies from the mathematical model and the experiments

Operating Points	Model Frequency (Hz)	Experiment Frequency (Hz)	Error (%)
A	337.6	349.4	3.4
B	173.7	175.8	1.2
C	168.2	175.8	4.3
	461.0	481.0	4.2
D	358.0	381.2	6.1

5.3.3 Resonator performance under strong thermoacoustic coupling

In this section, a conceptual case study is considered for a Rijke tube with substantially larger heat release rate into the system. One should remember that the heat release rate is the regenerative mechanism that manipulates the delayed influence of the unsteady pressure in the Rijke tube dynamics. Undoubtedly its

intensity, a, plays a very critical role on the analytical model [see the arguments around equation (3.14)]. This quantity represents the "strength of thermoacoustic coupling" in the system. If it is increased conceptually to the levels well above our experimental capabilities, it is expected to bring the influence of the time-delays to more pronounced levels. The mission in this subsection is to explore these influences.

A similar effect is also observed in the machine tool industry. The regenerative mechanism lies behind the *machine tool chatter* phenomenon (a.k.a. chatter instability) as well [51]. As the depth of cut increases, the regenerative effect amplifies, causing stronger chatter instability. It is analogous to the effect of heat release rate intensity on thermoacoustic instability.

Keeping all the operational parameters in Table 5.1 fixed except 'a' the gain (intensity) of heat release rate, the CTCR paradigm is repeatedly implemented on (5.28). Three different values for the intensity are considered: $a = 200$ (the experimentally studied case), $a = 400$ and $a = 600$. The corresponding stability maps are obtained as shown in Figure 5.8a, b and c, respectively. The stability map partitions are color-coded with the crossing frequency information. NU information is also provided in some select regions within the figures.

Notice that as the heat release rate intensity, a, increases, it becomes more difficult to stabilize the system with a Helmholtz resonator (i.e. the stable zones are very limited). This supports the argument that stronger thermoacoustic coupling amplifies the regenerative effects in the system, causing more violent instabilities. Beyond the conceptual bound of the heat release rate, $a = 600$, the system is almost impossible to stabilize (see Figure 5.8c). When compared with the stability maps for lower intensity values (Figure 5.8a and b) the frequency range at which instabilities occur is much broader in Figure 5.8c.

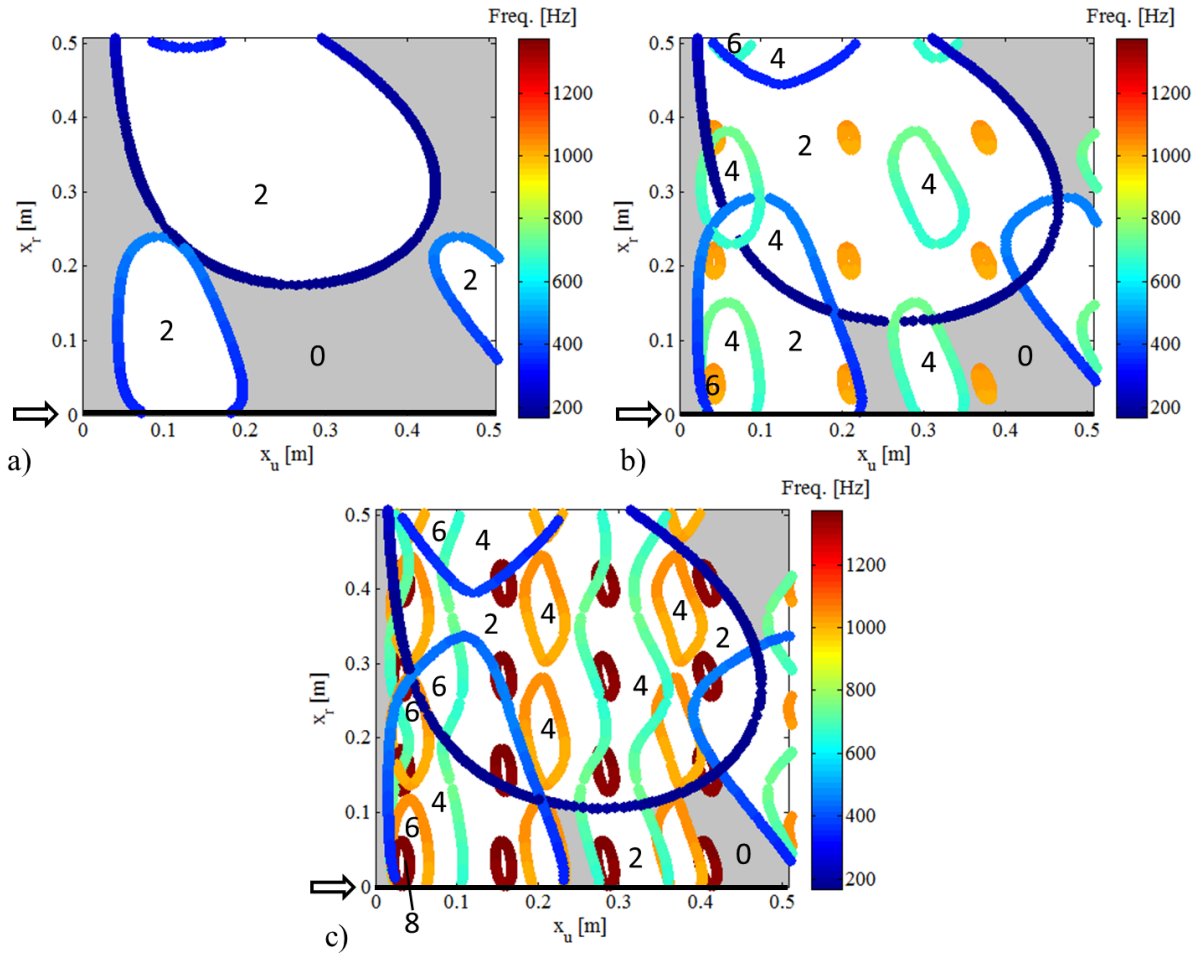

Figure 5.8 Frequency color-coded stability maps for (a) $a = 200$, (b) $a = 400$ and (c) $a = 600$.

In addition, one can observe that unlike Figure 5.8a, there are unstable regions with $NU > 2$ in Figure 5.8b and c, indicating that multiple earlier-undetected system modes are now excited at these settings and instability may occur at multiple modal frequencies. This reveals the following limitation: a single resonator may not very effective at stabilizing a system that is unstable at multiple (and distinct) modal frequencies. Then, one can pose the question whether utilization of multiple resonators would help passive stabilization in such a case. There are several experimental studies in the literature that follow this path [80]. Different resonator configurations can be conceived such as series and parallel [70], which result in similar suppression effects of multiple vibration absorbers. Although this study is confined to

single resonator designs, the baseline mathematical model is scalable to those cases with multiple resonators and different designs. Specifically, the CTCR paradigm can still be utilized in such configurations as the stability assessment tool, although the computational load would increase due to the higher system order and larger number of time delays.

Chapter 6 Active-Passive Control of Thermoacoustic Instabilities and Rise of Secondary Modes

In general, passive absorbers perform well in attenuating the amplitude of pressure oscillations. However, they are typically unable to eliminate them completely; in other words, these devices may not suffice to stabilize the unstable thermoacoustic dynamics. In that regard, combination of active and passive approaches may achieve better results. The passive absorber removes the bulk of the acoustic energy and the active control reduces the residual pressure fluctuations to practically zero. Since the active controller treats the already attenuated acoustic pressures (after the passive absorption), the energy required for it would be relatively small, which makes the operation highly desirable. An interesting study on such a deployment is [78] which also utilizes a Helmholtz resonator for passive absorption. In addition, a feedback control is used to optimally manipulate the amplitude and the frequency of the oscillations of the resonator's back-plate.

In this chapter, the active and passive approaches are combined to control the thermoacoustic instability in a Rijke tube. A Helmholtz resonator as in Chapter 5 and a separate feedback control loop as in Chapter 4 are used together. This combined construct of the Rijke tube together with both the active and passive control elements leads to a more complex system dynamics which will be studied here. More importantly, it creates a platform to study the interference of secondary dynamic modes to thermoacoustic instability.

The interference of secondary dynamic modes during thermoacoustic instability control has been experimentally observed in the literature ([14] and references therein). [24] studied the origin of such secondary mode instabilities using finite dimensional models, which are unable to capture the entire thermoacoustic dynamics. The analytical prediction of this phenomenon over an infinite dimensional mathematical model is missing in the literature. This chapter aims to address this problem and focuses on

the analytical prediction and experimental verification of thermoacoustic instability caused by secondary dynamic modes.

First, an LTI-NMTDS model of the Rijke tube dynamics containing a resonator and a feedback control loop is derived. The stability analysis results obtained through CTCR for the Rijke tube with and without the resonator are presented. Then, an unstable operation for the resonator-mounted tube is selected and it is attempted to stabilize the dynamics using a feedback controller. The controller parameters that can achieve this stabilization are exhaustively identified. These declarations yield the highlight theme of this study by displaying how certain control settings could invite instability in higher order dynamic modes of the system, while the originally unstable mode is stabilized. Finally, all the analytical findings are verified with experimental results from a laboratory scale Rijke tube.

6.1 Combined Mathematical Model for Rijke Tube with Active and Passive Control

The combined mathematical model is derived similar to the earlier chapters; however, with some differences. Rather than following a state-space approach, the LTI-NMTDS model is developed such that it leads to a classical eigenvalue problem eventually. Moreover, considering that the aim is to study instabilities caused by different thermoacoustic modes, a higher fidelity identification of the feedback loop components (e.g., microphone, loudspeaker, linear amplifier) is made rather than the flat frequency response assumption. The remaining assumptions made in Chapter 3 and 5 hold in this development.

The acoustic waves $f(x,t)$ and $g(x,t)$ are denoted as $f_i(t)$ and $g_i(t)$ in Figure 6.1a, with the subscript $i = 1,...,7$ indicating the cross-sections along the tube that the functions are evaluated at. $x = 0$ corresponds to location of the heater. The upstream and downstream tube ends are marked as $x = -x_u$ and downstream $x = x_d$, where x_u and x_d denote the distances between ①-② and ③-⑦, respectively.

The Helmholtz resonator is mounted at $x = x_h$ and the microphone is located at $x = x_m$ to record the downstream pressure fluctuations. The microphone senses the sound pressure signal which is fed through the controller and linear amplifier, and finally back into the system as a controlling pressure wave via a loudspeaker at the upstream end of the tube.

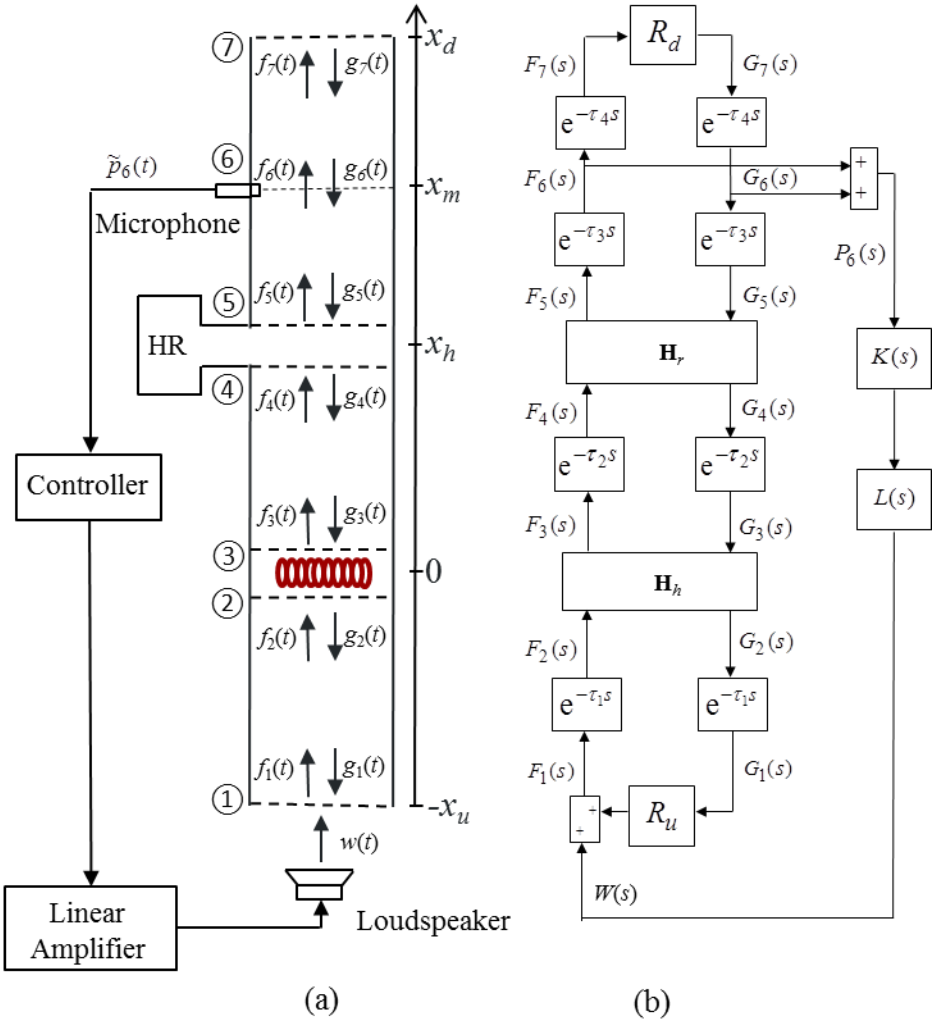

Figure 6.1 (a) Schematic representation of Rijke tube with Helmholtz resonator and a feedback control, (b) its block diagram representation.

The corresponding block diagram to this system is given in Figure 6.1b, where the system variables are the acoustic waves given in Laplace domain as $F_i(s)$ and $G_i(s)$, $i=1,...,7$. The time delays $\tau_1 = x_u/\bar{c}$, $\tau_2 = x_h/\bar{c}$, $\tau_3 = (x_m - x_h)/\bar{c}$ and $\tau_4 = (x_d - x_m)/\bar{c}$ represent the acoustic travel times. Next, the representative system model for the thermoacoustic dynamics is derived from a controls perspective.

All the cross-sectional variables in Figure 6.1b are interconnected through some causal relations. The interaction of acoustic waves at heating zone $(x=0)$ and resonator zone $(x=x_h)$ can be expressed as

$$\begin{bmatrix} G_2(s) \\ F_3(s) \\ G_4(s) \\ F_5(s) \end{bmatrix} = \mathbf{H} \begin{bmatrix} F_2(s) \\ G_3(s) \\ F_4(s) \\ G_5(s) \end{bmatrix}, \qquad \mathbf{H} = \begin{bmatrix} \mathbf{H}_h & \mathbf{0}_2 \\ \mathbf{0}_2 & \mathbf{H}_r \end{bmatrix} \tag{6.1}$$

where $\mathbf{0}_2$ is a vacuous matrix of size 2×2. The descriptors of $\mathbf{H}_h$ (transfer matrix at the heating zone) and $\mathbf{H}_r$ (transfer matrix at the Helmholtz resonator attachment) can be found in, equations (5.11) and (5.9) respectively. The acoustic pressure variables are connected to one another through some time delays as indicated in Figure 6.1b. These relations are captured, using the same set of variables as in equation (6.1), in the form of some transport delays

$$\begin{bmatrix} F_2(s) \\ G_3(s) \\ F_4(s) \\ G_5(s) \end{bmatrix} = \mathbf{T}_1 \begin{bmatrix} F_1(s) \\ G_4(s) \\ F_3(s) \\ G_7(s) \end{bmatrix}, \qquad \mathbf{T}_1 = \begin{bmatrix} \mathrm{e}^{-\tau_1 s} & 0 & 0 & 0 \\ 0 & \mathrm{e}^{-\tau_2 s} & 0 & 0 \\ 0 & 0 & \mathrm{e}^{-\tau_2 s} & 0 \\ 0 & 0 & 0 & \mathrm{e}^{-(\tau_3+\tau_4)s} \end{bmatrix} \tag{6.2}$$

The acoustic system variables at the tube ends (i.e. cross-sections ① and ⑦) are connected to each other via the reflection coefficients R_u and R_d. In addition, the feedback control signal $W(s)$ [Laplace domain representation of $w(t)$] acts as a control input to the system. This function denotes the speaker-induced additive acoustic pressure fluctuation at the upstream end of the tube and it is incorporated into the system dynamics as follows:

$$\begin{bmatrix} F_1(s) \\ G_4(s) \\ F_3(s) \\ G_7(s) \end{bmatrix} = \mathbf{R} \begin{bmatrix} G_1(s) \\ G_4(s) \\ F_3(s) \\ F_7(s) \end{bmatrix} + \begin{bmatrix} W(s) \\ 0 \\ 0 \\ 0 \end{bmatrix}, \qquad \mathbf{R} = \begin{bmatrix} R_u & 0 & 0 & 0 \\ 0 & 1 & 0 & 0 \\ 0 & 0 & 1 & 0 \\ 0 & 0 & 0 & R_d \end{bmatrix} \tag{6.3}$$

The input vector on the right-hand-side of (6.3) multiplying $\mathbf{R}$ is written in terms of the output vector in (6.1) as

$$\begin{bmatrix} G_1(s) \\ G_4(s) \\ F_3(s) \\ F_7(s) \end{bmatrix} = \mathbf{T}_2 \begin{bmatrix} G_2(s) \\ F_3(s) \\ G_4(s) \\ F_5(s) \end{bmatrix}, \qquad \mathbf{T}_2 = \begin{bmatrix} \mathrm{e}^{-\tau_1 s} & 0 & 0 & 0 \\ 0 & 0 & 1 & 0 \\ 0 & 1 & 0 & 0 \\ 0 & 0 & 0 & \mathrm{e}^{-(\tau_3+\tau_4)s} \end{bmatrix} \tag{6.4}$$

Equations (6.1) - (6.4) complete the dynamic representation of the Rijke tube. Before finalizing the modelling effort, however, one needs to look at the formation of the feedback control element $W(s)$, as it is a critical element in the overall system behavior.

The control command $W(s)$ should be looked at as an ensemble of several dynamical components: downstream acoustic pressure sensor, the feedback control logic, linear power amplifier and the loudspeaker (actuator). Such a combined effect can be modelled as follows

$$W(s) = K(s)L(s)P_6(s) = K(s)L(s)[F_6(s) + G_6(s)] = K(s)L(s)\mathrm{e}^{-\tau_3 s}[1 + R_d \mathrm{e}^{-2\tau_4 s}]F_5(s) \tag{6.5}$$

Here, $K(s)$ denotes the actual control logic which is user defined, whereas $L(s)$ represents the combined transfer function of all the remaining components in the feedback loop, such as the microphone, linear amplifier and the loudspeaker. $P_6(s)$ is the combination of $F_6(s)$ and $G_6(s)$ as per (3.6) at the cross-section ⑥. In this investigation a time-delayed integral control logic is adopted, which consists of a control gain K and a control delay τ_5:

$$K(s) = -\frac{1}{s}\mathrm{K}\mathrm{e}^{-\tau_5 s} \tag{6.6}$$

This logic provides some filtering (averaging) effect with its integral action on the measurement noise as well as the amplification gain and a proper signal delay. This is the same construct that has been utilized in Chapter 4 for active control.

In the literature [14], the delay element τ_5 in (6.6) is characteristically selected as a "phase shift operator" when the dynamic suppression is aimed at a particular mode and the corresponding frequency. This logic comes with a controversial proposition. Such modal suppression attempts need to first identify the mode in which the tube dynamics will exhibit instability, and this needs to be done a priori to the control implementation. Once the troublesome frequency is identified, the relevant phase shift is determined by selecting an appropriate delay τ_5. Here, the interlinking of the control delay with the targeted frequency of instability is ignored. This point constitutes the highlight theme of the study, that the system at hand is infinite dimensional, thus it has infinitely many modes, and any one of them can exhibit instability while the conventional controller is occupied with suppression of a specific frequency. To preclude such an occurrence the dynamic suppression has to be performed in a holistic fashion and to assure stability in all the infinitely many modes of the system, not only a few. As such the delay in (6.6) has to be conceived as a completely free and independent control parameter to be selected for the design of the control logic.

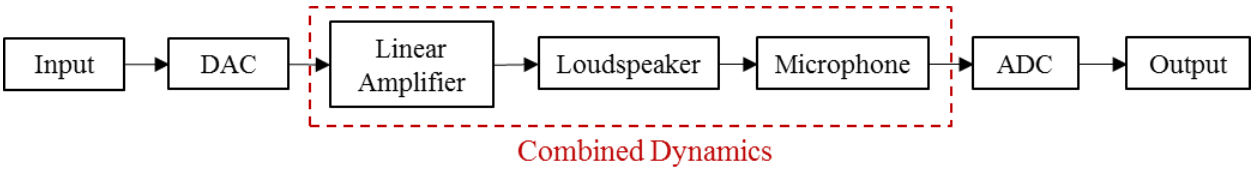

Figure 6.2 Block diagram of the open loop setup for the identification of the combined sensor/actuator setting.

One critical element in (6.5) is $L(s)$ as it represents the dynamic properties of many components. To identify $L(s)$ with some level of fidelity, a set of open-loop system identification tests is conducted using a data acquisition system (dSpace MicroAutoBox), linear amplifier, loudspeaker and the microphone. The

microphone is positioned facing the loudspeaker and the setup is structured as shown in Figure 6.2. Notice that the Rijke tube related elements are kept completely out of this exercise.

A chirp signal is provided as the input with a unity gain, covering a frequency range of 10-1000 Hz for a duration of 100 seconds. The data acquisition takes place at a sampling rate of 10 kHz. A transfer function is conceived using empirical and iterative model matching trials to represent this set-up, such that the frequency response characteristics concur between those obtained from experimental data and from the model. The resulting transfer function for the given system is

$$L(s) = \frac{500\, s^2}{s^3 + 5855 s^2 + 1.263 \times 10^6 s + 7.493 \times 10^8} \tag{6.7}$$

Such a component identification operation for the combined sensor/actuator couple is an essential step in order to reach an accurate control design. In Chapter 4 it is shown that flat frequency response assumption for the sensor/actuator setting (i.e., the assumption that these elements act like a simple "gain" operator) is sufficient to stabilize the fundamental unstable mode of the dynamics. Nevertheless, this assumption fails to capture the potential instabilities caused by the secondary dynamic modes (with different modal frequencies) of the thermoacoustic system. Considering that the aim here is to study especially the interference of the secondary dynamic modes to thermoacoustic instability, a more accurate identification of combined sensor/actuator couple is required.

The comparison of Bode plots using the experimental data and the model transfer function of (6.7) is shown in Figure 6.3. The identified transfer function matches very well with the experiment within the range of 150-600 Hz, although there is acceptable level of deviation at frequencies outside this range. A higher order, but more representative transfer function with better fidelity could still be obtained. This would however, increase the computational complexity further. For the objectives of the study it is sufficient to adopt $L(s)$ as in (6.7).

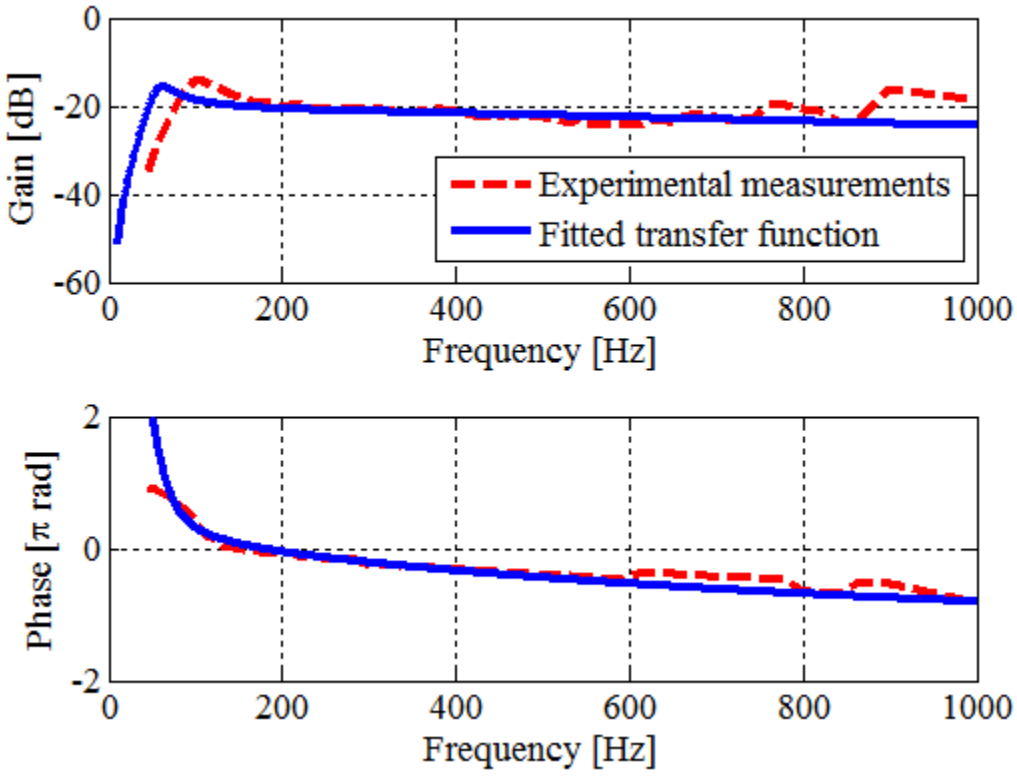

Figure 6.3 Identification of $L(s)$, the open loop transfer function in the feedback line.

Now that the feedback controlled pressure wave $W(s)$ is expressed in terms of the acoustic system variables, (6.5) is rewritten as

$$\begin{bmatrix} W(s) \\ 0 \\ 0 \\ 0 \end{bmatrix} = \mathbf{\Pi} \begin{bmatrix} G_2(s) \\ F_3(s) \\ G_4(s) \\ F_5(s) \end{bmatrix}, \qquad \mathbf{\Pi} = \begin{bmatrix} 0 & 0 & 0 & K(s)L(s)\mathrm{e}^{-\tau_3 s}\left[1 + R_d \mathrm{e}^{-2\tau_4 s}\right] \\ 0 & 0 & 0 & 0 \\ 0 & 0 & 0 & 0 \\ 0 & 0 & 0 & 0 \end{bmatrix} \tag{6.8}$$

Using (6.4) and (6.8) in (6.3) and combining the result with (6.1) and (6.2) gives

$$\begin{bmatrix} G_2(s) & F_3(s) & G_4(s) & F_5(s) \end{bmatrix}^{\mathrm{T}} = \mathbf{H}\mathbf{T}_1\left[\mathbf{R}\mathbf{T}_2 + \mathbf{\Pi}\right]\begin{bmatrix} G_2(s) & F_3(s) & G_4(s) & F_5(s) \end{bmatrix}^{\mathrm{T}} \tag{6.9}$$

Then the overall system representation becomes

$$\mathbf{M}\left[G_2(s) \quad F_3(s) \quad G_4(s) \quad F_5(s)\right]^{\mathrm{T}} = 0, \qquad \mathbf{M} = \mathbf{I}_4 - \mathbf{H}\mathbf{T}_1\left[\mathbf{R}\mathbf{T}_2 + \mathbf{\Pi}\right] \tag{6.10}$$

where $\mathbf{I}_4$ is 4×4 identity matrix and $\mathbf{M}$ represents the entire system matrix. Equation (6.10) presents a classical eigenvalue problem and $\mathbf{M}$ leads to a determinant which forms the characteristic equation of the system

$$CE(s,\boldsymbol{\tau}) = \det(\mathbf{M}) = 0 \tag{6.11}$$

This is a quasi-polynomial equation involving five independent time delays, which are represented by the delay vector $\boldsymbol{\tau} = (\tau_1, \tau_2, ..., \tau_5) \in \Re^{5+}$. The dynamics represented by the characteristic polynomial in (6.11) falls into the linear time-invariant multiple time-delay system (LTI-MTDS) class of neutral type as we discussed in Chapter 2.

6.2 Detection of Secondary-mode Interference in Thermoacoustic Instability Control

In this section, the effect of combined active-passive control strategies on the stability properties of Rijke tube is investigated analytically using the CTCR paradigm. The following systematic stages are followed.

(i) First, the stability of uncontrolled Rijke tube without the resonator is studied. The heater is intentionally positioned in the tube such that the operation becomes unstable. Then, CTCR analysis of the tube with a Helmholtz resonator is performed similar to Chapter 5. The resonator design is kept suboptimal, again on purpose and its location on the tube is selected such that the system still operates in an unstable mode even after including the resonator.

(ii) On this unstable system the time delayed integral control logic is deployed and the overall system stability variations are studied for the controlled dynamics. The controller parameters that stabilize the system are identified exhaustively, again using the CTCR-generated stability maps.

(iii) At the very end of this chain of tests the following is demonstrated: A given feedback control logic, if not selected pursuant to a holistic analytical methodology, may in fact excite the secondary modes of the system, while suppressing the unstable mode of the dynamics. This critical nuance was observed in earlier investigations and with this study a crisp analytical reasoning is provided.

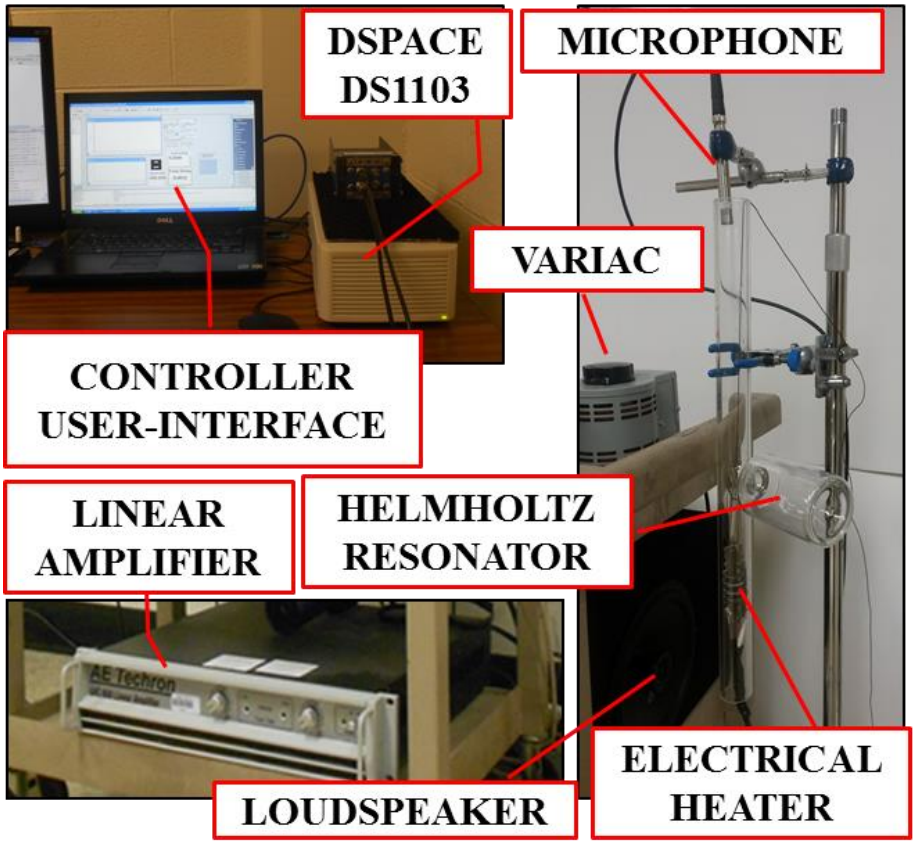

Figure 6.4 Picture of the experimental setup.

All these revelations of CTCR are validated step by step using the results from the corresponding experimental tests which are conducted on a laboratory scale Rijke tube. A picture of the setup is provided in Figure 6.4 and the critical parameters of the test platform are provided in Table 6.1.

6.2.1 Unstable Rijke tube with passive control

The characteristic equation of the Rijke tube dynamics in absence of the feedback loop and the resonator can be obtained by simply substituting $K(s)=0$ and $\mathbf{H}_r=\begin{bmatrix}0 & 1\\ 1 & 0\end{bmatrix}$ in equation (6.11). Using the parameters in Table 6.1 this equation becomes

$$\begin{aligned} CE_1(s,\boldsymbol{\tau}) = (1-0.865\,\mathrm{e}^{-2(\tau_1+\tau_2+\tau_3+\tau_4)s})\,s + 699.3 + 185.3\,\mathrm{e}^{-2\tau_1 s} \\ -185.3\mathrm{e}^{-2(\tau_2+\tau_3+\tau_4)s} - 604.8\mathrm{e}^{-2(\tau_1+\tau_2+\tau_3+\tau_4)s} = 0 \end{aligned} \tag{6.12}$$

where $\boldsymbol{\tau}=(\tau_1,\tau_2,\tau_3,\tau_4)\in\Re^{4+}$. Theorem 2.2 for the dynamics given by equation (6.12) is checked first. The corresponding difference operator is extracted as

$$D_1(s,\boldsymbol{\tau}) = 1-0.865\,\mathrm{e}^{-2(\tau_1+\tau_2+\tau_3+\tau_4)s} = 0 \tag{6.13}$$

It is apparent that $|\mathrm{e}^{-2(\tau_1+\tau_2+\tau_3+\tau_4)s}|=1.16>1$ yields infinitely many zeros all of which lie in $\mathbf{C}^-$. Therefore the necessary condition in Theorem 2.2 is satisfied for any delay composition. Next, the exponential stability of the complete system given in equation (6.12) is tested as per Theorem 2.1, again using the CTCR paradigm. Its stability map is created in the selected parametric space of tube length [i.e., $L=(\sum_{j=1}^{4}\tau_j)\bar{c}$] and the heater location $x_u=\tau_1\bar{c}$ as shown in Figure 6.5a.

In Figure 6.5a, the shaded region represents stable operating conditions. That is, when Rijke tube length and heater location composition (L,x_u) is selected outside this shaded area, the pressure oscillations are expected to grow in amplitude exponentially (a linear system characteristic). When such an unstable test is conducted the growing amplitudes eventually settle into a limit cycle (a nonlinear system characteristic) as discussed in the earlier chapters. The color-coded curve [i.e., $\wp$ - see (2.11)] that separates the stable and unstable regions represents the loci of (L,x_u) compositions, for which (6.12) has a pair of characteristic roots on the imaginary axis. The system is marginally stable along this curve, and the color-

coding represents the imaginary root locations (resonant frequencies) in Hz. Furthermore, the number of unstable roots (*NU*) of the characteristic polynomial (6.12) is noted in each region. When $NU = 0$, all the characteristic roots are in $\mathbf{C}^-$, in other words the system is exponentially stable.

Table 6.1 Operational parameters for the Rijke tube with active-passive control

Parameter	Value	Unit
R_u	-0.93	-
R_d	-0.93	-
γ	1.4	-
A	7.07×10^{-4}	m^2
L	0.508	m
$\bar{\rho}$	1.204	kg/m^3
$\bar{c}$	343.4	m/s
a	200	-
b	0.002	-
S_n	2.27×10^{-4}	m^2
V	2.65×10^{-4}	m^3
l_n	0.025	m

As given in Table 6.1, the tube length in our experiment is $L = 0.508\,\text{m}$. In the following tests the heater location is intentionally fixed at $x_u = 0.102\,\text{m}$ (point **A** in Figure 6.5a), which makes the thermoacoustic dynamics in the system unstable.

Next, on this unstable Rijke tube the effects of mounting a Helmholtz resonator is investigated briefly. The effectiveness of the resonator in dynamic suppression is directly correlated to the proximity of the frequency at which the resonator offers maximum damping and the frequency of unstable pressure oscillations. The geometric dimensions of the resonator are selected [see (5.9) and Table 6.1] such that its resonant frequency $(254.7\,\text{Hz})$ is different from the frequency of unstable pressure oscillations at point **A** $(349.1\,\text{Hz})$. This indicates a sub-optimum resonator design for passive control of the unstable Rijke tube dynamics. Taking $K(s) = 0$ (i.e., no feedback control) and forming the $\mathbf{H}_r$ matrix as according to (5.9), characteristic equation (6.11) exhibits a new form

$$
\begin{aligned}
CE_2(s,\vec{\tau}) = {} & (1-0.865\,\mathrm{e}^{-2(\tau_1+\tau_2+\tau_3+\tau_4)s})\,s^3 + (2104+185.3\,\mathrm{e}^{-2\tau_1 s} - 185.3\mathrm{e}^{-2(\tau_2+\tau_3+\tau_4)s} \\
& - 1300.0\,\mathrm{e}^{-2(\tau_1+\tau_2)s} - 1300.0\,\mathrm{e}^{-2(\tau_3+\tau_4)s} + 598.1\mathrm{e}^{-2(\tau_1+\tau_2+\tau_3+\tau_4)s})s^2 + (3.54\times10^6 \\
& + 2.60\times10^5\,\mathrm{e}^{-2\tau_1 s} + 2.58\times10^5\,\mathrm{e}^{-2(\tau_2+\tau_3+\tau_4)s} - 2.79\times10^5\,\mathrm{e}^{-2\tau_2 s} - 2.41\times10^5\,\mathrm{e}^{-2(\tau_1+\tau_3+\tau_4)s} \\
& - 9.09\times10^5\,\mathrm{e}^{-2(\tau_1+\tau_2)s} - 9.09\times10^5\,\mathrm{e}^{-2(\tau_3+\tau_4)s} - 1.37\times10^6\,\mathrm{e}^{-2(\tau_1+\tau_2+\tau_3+\tau_4)s})s + 1.79\times10^9 \\
& + 4.75\times10^8\,\mathrm{e}^{-2\tau_1 s} - 4.75\times10^8\,\mathrm{e}^{-2(\tau_2+\tau_3+\tau_4)s} - 1.55\times10^9\,\mathrm{e}^{-2(\tau_1+\tau_2+\tau_3+\tau_4)s} = 0
\end{aligned}
\tag{6.14}
$$

Notice that the difference operator in (6.14) is identical to the one in (6.13), $D_2(s,\boldsymbol{\tau}) = D_1(s,\boldsymbol{\tau})$. Therefore the necessary condition of Theorem 2.2 is automatically satisfied. Fixing the tube length at $L = 0.508\,\mathrm{m}$, the stability map for (6.14) is generated using the unique procedure of CTCR once more, but this time in the domain of $x_r = x_d - x_h = (\tau_3 + \tau_4)\bar{c}$ and $x_u = \tau_1\bar{c}$ as shown in Figure 6.5b. Similar to Figure 6.5a, the shaded region is stable (corresponding to $NU = 0$) and the resonant frequencies are color-coded on the curves separating the stable and unstable regions in Figure 6.5b. While the heater is at $x_u = 0.102\,\mathrm{m}$ (point **A** in Figure 6.5a) the Helmholtz resonator is attached at $x_r = 0.330\,\mathrm{m}$, which corresponds to point **B** in Figure 6.5b. The new operating configuration purposely selected once again within the unstable region, but with some different characteristics as discussed next.

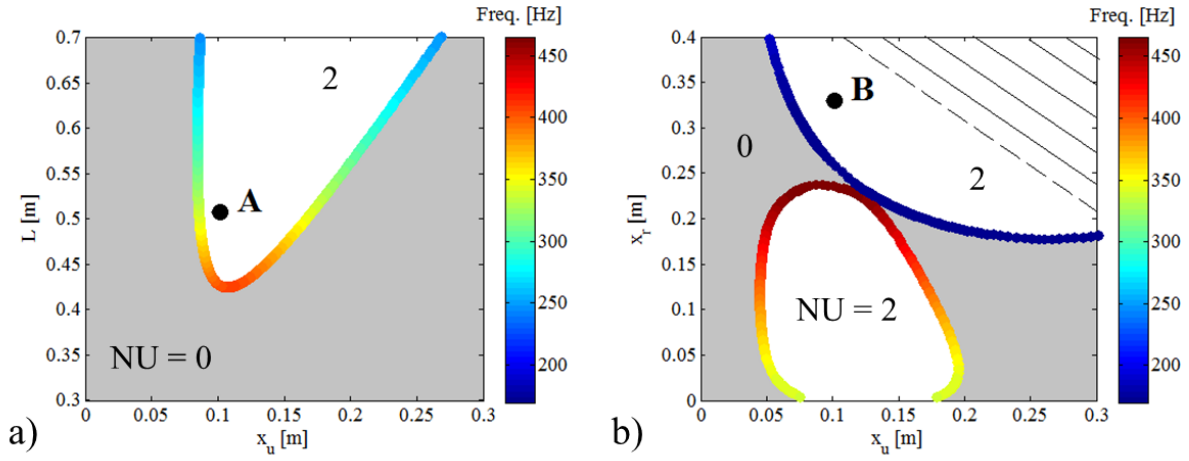

Figure 6.5 Stability maps of (a) plain Rijke tube in (L, x_u) space, (b) resonator mounted Rijke tube in (x_r, x_u) space.

To compare the two different unstable operating conditions at points **A** and **B**, the QPmR algorithm is deployed. Using QPmR on characteristic equations (6.12) and (6.14) for points **A** and **B**, respectively, the dominant root distributions are obtained as presented in Figure 6.6a. Notice that there is only a pair of characteristic roots in $\mathbf{C}^+$ for both cases, indicating that the oscillations of growing amplitudes will take place at a single frequency. This modal frequency is obviously different at points **A** and **B**, since the imaginary parts of the unstable roots are considerably different as seen in Figure 6.6a. To verify this, the pressure oscillations are recorded experimentally as the system operates at these points. In Figure 6.6b, these time traces of pressure oscillations for unstable operating points **A** and **B** are displayed (without and with the resonator, respectively). The fundamental frequencies of these two pressure readings are extracted at the onset of the respective exponential growth phases, performing sectional FFT. The corresponding power spectral densities are shown in Figure 6.6c, with the experimentally measured center frequencies at $f_{\text{ex}}^{\mathbf{A}} = 349.1\text{Hz}$, $f_{\text{ex}}^{\mathbf{B}} = 175.8\text{Hz}$. These frequencies are also calculated using the dominant roots of the conceived models as shown in Figure 6.6a, $f_{\text{mod}}^{\mathbf{A}} = 340.8\text{Hz}$, $f_{\text{mod}}^{\mathbf{B}} = 175.3\text{Hz}$. The disagreements between the analytically obtained values and those from the experiments are very small, which gives a strong encouragement to the procedure presented here.

As an important observation, the amplitude of pressure oscillations after the limit cycle behavior sets in Figure 6.6b, are much smaller for operating point **B** when compared to those of point **A**. One can claim that the addition of the Helmholtz resonator to the Rijke tube as a passive control element reduces the residual oscillatory energy, which is exhibited by lower limit cycle amplitudes. It is obvious that the resonator is absorbing some energy, but without being able to stabilize the system as the CTCR stability maps declared in Figure 6.5b. Therefore the proposed analytical methodology used here provides a definitive new insight to the stability posture of the complex dynamics.

6.2.2 Active-passive controlled Rijke tube stability and excitation of secondary modes

In this section, the unstable operating conditions of **B** are taken, and a feedback loop is introduced with the control law (6.6). The objective is to stabilize the unstable dynamics of the resonator-mounted Rijke tube, without targeting any modal frequency. Once again, the present approach decouples the treatment from some particular modes of the system. Therefore it is a holistic procedure of stabilization in the truly infinite-dimensional sense.

When the controller gain and feedback delay (K, τ_5) are considered as free parameters, (6.11) can be rewritten using the model in (6.7) it exhibits a 6th order LTI-NMTDS,

$$
\begin{aligned}
CE_3(s,\boldsymbol{\tau}) = {} & (1-0.865\,\mathrm{e}^{-2(\tau_1+\tau_2+\tau_3+\tau_4)s})\,s^6 + (7959 + 185.3\,\mathrm{e}^{-2\tau_1 s} - 185.3\mathrm{e}^{-2(\tau_2+\tau_3+\tau_4)s} \\
& - 1300.0\,\mathrm{e}^{-2(\tau_1+\tau_2)s} - 1300.0\,\mathrm{e}^{-2(\tau_3+\tau_4)s} - 4466\,\mathrm{e}^{-2(\tau_1+\tau_2+\tau_3+\tau_4)s})s^5 + (1.71\times10^7 + 1.34\times10^6\,\mathrm{e}^{-2\tau_1 s} \\
& - 8.27\times10^5\,\mathrm{e}^{-2(\tau_2+\tau_3+\tau_4)s} - 2.79\times10^5\,\mathrm{e}^{-2\tau_2 s} - 8.52\times10^6\,\mathrm{e}^{-2(\tau_1+\tau_2)s} - 8.52\times10^6\,\mathrm{e}^{-2(\tau_3+\tau_4)s} \\
& + 1.04\times10^6\,\mathrm{e}^{-2(\tau_1+\tau_2+\tau_3+\tau_4)s} - 2.41\times10^5\,\mathrm{e}^{-2(\tau_1+\tau_3+\tau_4)s} - 465\mathrm{K}\mathrm{e}^{-(\tau_1+\tau_2+\tau_3+2\tau_4+\tau_5)s} \\
& + 500\,\mathrm{K}\mathrm{e}^{-(\tau_1+\tau_2+\tau_3+\tau_5)s})s^4 + (2.59\times10^{10} + 2.23\times10^9\,\mathrm{e}^{-2\tau_1 s} + 8.01\times10^8\,\mathrm{e}^{-2(\tau_2+\tau_3+\tau_4)s} \\
& - 1.63\times10^9\,\mathrm{e}^{-2\tau_2 s} - 6.96\times10^9\,\mathrm{e}^{-2(\tau_1+\tau_2)s} - 6.96\times10^9\,\mathrm{e}^{-2(\tau_3+\tau_4)s} - 9.48\times10^9\,\mathrm{e}^{-2(\tau_1+\tau_2+\tau_3+\tau_4)s} \\
& - 1.41\times10^9\,\mathrm{e}^{-2(\tau_1+\tau_3+\tau_4)s} - 4.21\times10^5\,\mathrm{K}\mathrm{e}^{-(\tau_1+\tau_2+\tau_3+2\tau_4+\tau_5)s} + 4.53\times10^5\,\mathrm{K}\mathrm{e}^{-(\tau_1+\tau_2+\tau_3+\tau_5)s})s^3 \\
& + (1.65\times10^{13} + 3.25\times10^{12}\,\mathrm{e}^{-2\tau_1 s} - 2.59\times10^{12}\,\mathrm{e}^{-2(\tau_2+\tau_3+\tau_4)s} - 3.52\times10^{11}\,\mathrm{e}^{-2\tau_2 s} - 2.12\times10^{12}\,\mathrm{e}^{-2(\tau_1+\tau_2)s} \\
& - 2.12\times10^{12}\,\mathrm{e}^{-2(\tau_3+\tau_4)s} - 1.04\times10^{13}\,\mathrm{e}^{-2(\tau_1+\tau_2+\tau_3+\tau_4)s} - 3.04\times10^{11}\,\mathrm{e}^{-2(\tau_1+\tau_3+\tau_4)s} \\
& - 1.19\times10^9\,\mathrm{K}\mathrm{e}^{-(\tau_1+\tau_2+\tau_3+2\tau_4+\tau_5)s} + 1.28\times10^9\,\mathrm{K}\mathrm{e}^{-(\tau_1+\tau_2+\tau_3+\tau_5)s})s^2 + (4.92\times10^{15} + 7.95\times10^{14}\,\mathrm{e}^{-2\tau_1 s} \\
& - 4.06\times10^{14}\,\mathrm{e}^{-2(\tau_2+\tau_3+\tau_4)s} - 2.09\times10^{14}\,\mathrm{e}^{-2\tau_2 s} - 6.81\times10^{14}\,\mathrm{e}^{-2(\tau_1+\tau_2)s} - 6.81\times10^{14}\,\mathrm{e}^{-2(\tau_3+\tau_4)s} \\
& - 2.99\times10^{15}\,\mathrm{e}^{-2(\tau_1+\tau_2+\tau_3+\tau_4)s} - 1.81\times10^{14}\,\mathrm{e}^{-2(\tau_1+\tau_3+\tau_4)s} - 1.07\times10^{12}\,\mathrm{K}\mathrm{e}^{-(\tau_1+\tau_2+\tau_3+2\tau_4+\tau_5)s} \\
& + 1.15\times10^{12}\,\mathrm{K}\mathrm{e}^{-(\tau_1+\tau_2+\tau_3+\tau_5)s})s + 1.34\times10^{18} + 3.56\times10^{17}\,\mathrm{e}^{-2\tau_1 s} - 3.56\times10^{17}\,\mathrm{e}^{-2(\tau_2+\tau_3+\tau_4)s} \\
& - 1.16\times10^{18}\,\mathrm{e}^{-2(\tau_1+\tau_2+\tau_3+\tau_4)s} = 0
\end{aligned}
\tag{6.15}
$$

where $\boldsymbol{\tau} = (\tau_1, \tau_2, \tau_3, \tau_4, \tau_5) \in \Re^{5+}$ has five independent delays. Four of them are constants due to the fixed tube length, heater location, resonator location and microphone position and they can be determined as explained in Section 6.1. The only remaining parameters (K, τ_5) form the domain where the stability maps will be explored using the CTCR paradigm.

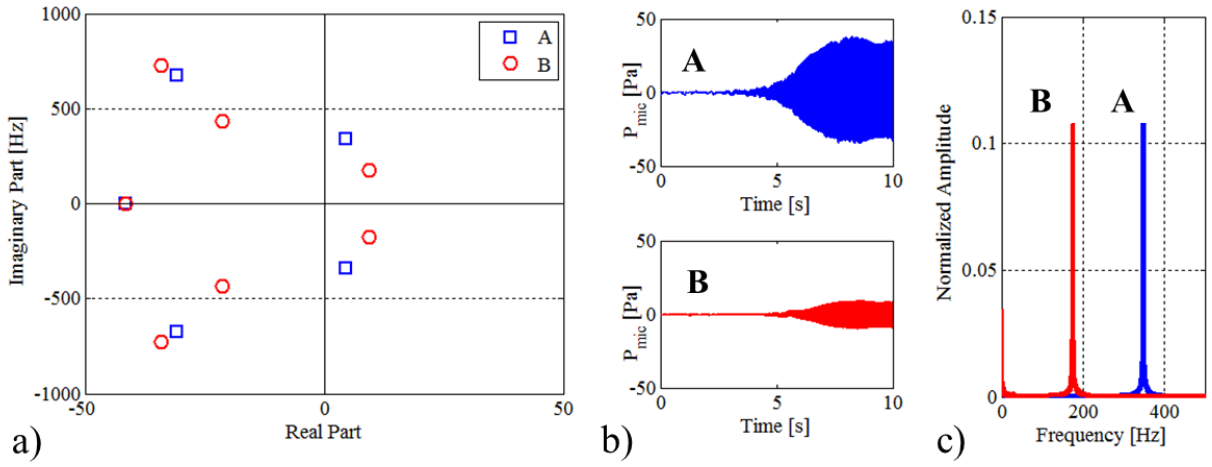

Figure 6.6 (a) QPmR-generated characteristic root locations at points **A** and **B** in Figure 6.5a and b, respectively; (b) microphone recordings from the corresponding experimental tests; (c) segmented FFT outlook for these measured signals.

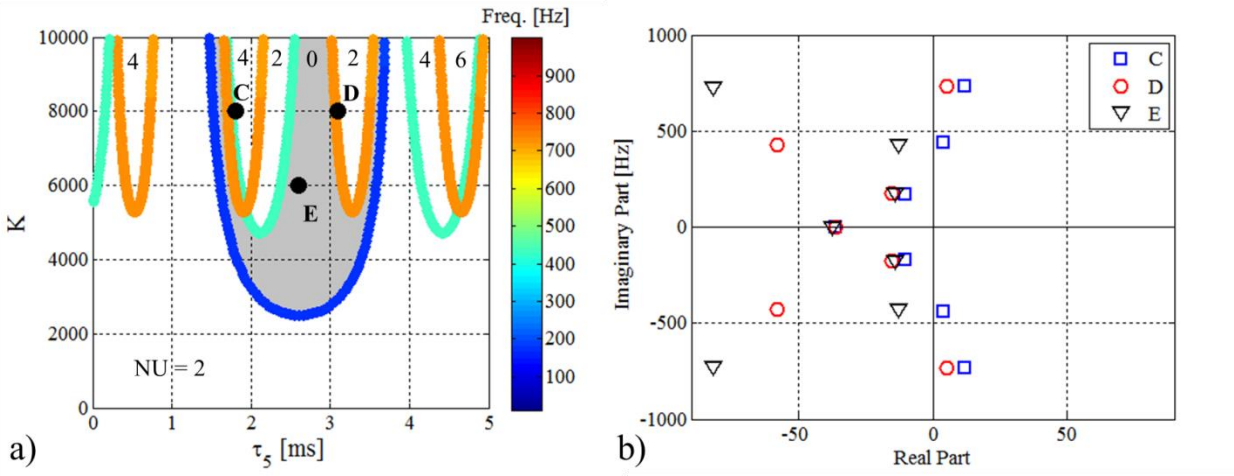

Figure 6.7 (a) Stability map in controller parameter space, (K, τ_5), (b) QPmR-generated characteristic root locations at points **C**, **D** and **E** in (a).

The difference operator of (6.15) is again identical to (6.13), so the necessary condition in Theorem 2.2 holds. The earlier mentioned parameters $L = 0.508\text{m}$, $x_u = 0.102\text{ m}$ and $x_r = 0.330\text{ m}$ ($x_h = 0.076\text{ m}$) are

fixed to identify the operating conditions at point **B** in Figure 6.5b, but this time with feedback control. The microphone, which is used as the sensor to measure the pressure fluctuations, is placed at $x_m = 0.356\,\text{m}$. The stabilizing controller designs in the domain of (K, τ_5) are exhaustively declared via CTCR as shown in Figure 6.7a along with the marginal stability frequencies at the stability boundaries (indicated by color coding) and the regional number of unstable roots as marked.

The origin of Figure 6.7a corresponds to the uncontrolled dynamics at point **B** in Figure 6.5b, which is unstable at a modal frequency of $f_{\text{mod}}^{\mathbf{B}} = 175.3\,\text{Hz}$. When the control as suggested in (6.6) is deployed using the parameters (K, τ_5) from within the shaded region (where $NU = 0$), the system is stabilized. But a striking feature in this figure appears for high-gain control applications such as $\text{K} > 5000$. If the controller parameters are not carefully selected, it is clear that, the system can be destabilized at some higher dynamic modes of the system, although the initial unstable dynamic mode remains stabilized. This feature has been observed by other researchers [19] and it forms a key contribution. Same discovery is mentioned without justification in [14] as: "Simple controllers involving just a fixed time delay of phase-shift introduce a new oscillation mode, which becomes unstable as gain is increased and gives rise to a new peak in the pressure spectrum". The excitement in the present findings is that the CTCR paradigm provides a holistic methodology to identify the destabilizing design selections as opposed to those that impart stability for high-gain time-delayed controller so that undesired instabilities at other frequencies (i.e., higher modes) will not occur.

To demonstrate this crucial point, three control settings are picked: $(\text{K}, \tau_5) = (8000, 1.8\,\text{ms})$, $(\text{K}, \tau_5) = (8000, 3.1\,\text{ms})$, $(\text{K}, \tau_5) = (6000, 2.6\,\text{ms})$, which are represented by points **C**, **D** and **E** in Figure 6.7a. The number of unstable roots of (6.15) declared by the CTCR for these cases are $NU = 4$, $NU = 2$ and $NU = 0$, respectively. Therefore we expect to observe two unstable modes at point **C**, one unstable mode at point **D** and stable operation at point **E**.

The QPmR-generated characteristic root distribution of equation (6.15) is plotted in Figure 6.7b, for (K, τ_5) compositions at these points. The initial unstable system with a characteristic root pair in the right half plane (at the frequency of $f_{\text{mod}}^{\mathbf{B}} = 175.3\text{Hz}$ in Figure 6.6a) is now stabilized by selecting (K, τ_5) at point **E**. The remarkable feature appears at this junction. Although this unstable root pair can be brought to left half plane by selecting (K, τ_5) at points **C** or **D**, the other characteristic roots (i.e., those of the higher order modes) of the system migrate to right half plane at higher frequencies. As predicted by *NU* distributions in Figure 6.7a, Figure 6.7b shows that the system has two pairs of characteristic roots in right half plane for point **C**, and one pair for point **D**. Such a design for controller unfortunately results in an unstable system again, but pressure oscillations take place at different frequencies.

Figure 6.8, Figure 6.9 and Figure 6.10 display the experimental results corresponding to those points **C**, **D** and **E** in Figure 6.7a. In pane (a) of these three figures, the microphone-detected pressure fluctuations are shown. The control is off at the beginning, so the pressure fluctuations start to grow exponentially and then they are set into a limit cycle in all three figures. Until the control is turned on, we observe the same scenario as for point **B** in Figure 6.6b. The instant the control triggers is marked with a thin red line. From that moment on the pressure fluctuations start decaying in all three cases; only to start an exponential growth after some time in Figure 6.8a and Figure 6.9a (for operating points **C**, **D**). Although the initial unstable mode is stabilized for all three (K, τ_5) selections, when the control parameters are selected at points **C**, **D**, secondary dynamic modes of the system are destabilized. This phenomenon exhibits itself as the pressure fluctuations growing in amplitude at relatively higher frequencies. On the other hand, when the controller parameters are set to point **E**, the system stays stable following an explicit exponential decay behavior (see Figure 6.10a).

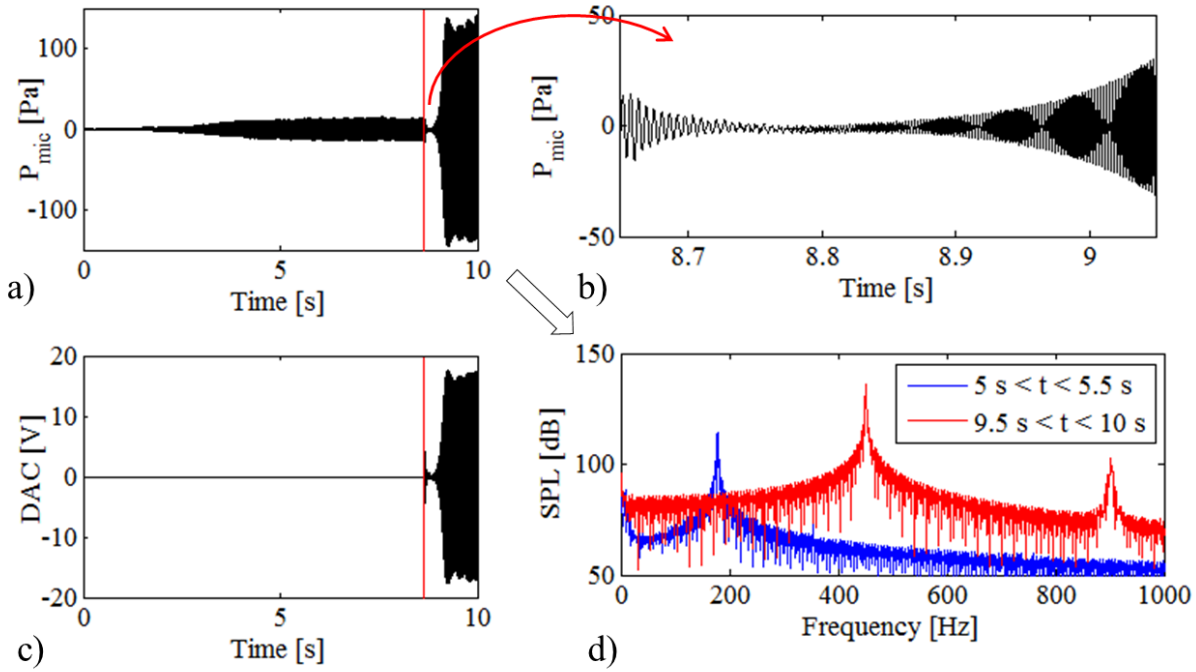

Figure 6.8 (a) Microphone recording from the experiments for point **C** in Figure 6.7a, (b) Zoomed-in view of the pressure time trace after control is turned on, (c) control signal that is sent to the DAC channel, (d) sound pressure level measurements before and after the control is turned on.

In Figure 6.8b, Figure 6.9b and Figure 6.10b, zoomed version of the pressure fluctuations just after the control is turned on are shown. Linear system behavior of exponential growth in the first two, and exponential decay in the last are very clearly observed. In Figure 6.8c, Figure 6.9c and Figure 6.10c, the control signals which are produced at the DAC (D/A conversion) port of the real-time control card are displayed. In Figure 6.8d, Figure 6.9d and Figure 6.10d, the corresponding sound pressure levels of the pressure fluctuations are displayed immediately before and after the controller is triggered. For all three cases, sound pressure levels show a peak at around $178.2\,\mathrm{Hz}$ before control is turned on, which are measured after the first limit cycle sets. This is expectedly very close to $f_{\mathrm{ex}}^{\mathbf{B}} = 175.8\,\mathrm{Hz}$, which was measured at the onset of instability (during the exponential growth without the control). After control is

triggered, Figure 6.8d shows two peaks, which are at $f_{ex}^{\mathbf{C}_1} = 450.4\,\text{Hz}$ and $f_{ex}^{\mathbf{C}_2} = 902.1\,\text{Hz}$. When compared with the imaginary parts of the corresponding characteristic roots for point **C** in Figure 6.7b, $f_{mod}^{\mathbf{C}_1} = 437.9\,\text{Hz}$ and $f_{mod}^{\mathbf{C}_2} = 731.5\,\text{Hz}$, it is observed that the former is very close although the latter is about 18% off. The earlier mentioned modelling mismatch for the sensor-actuator duo (in Figure 6.3), between the fitted transfer function $L(s)$ and the experimental data for frequencies over $600\,\text{Hz}$, are likely to be accountable for this discrepancy. Needless to say, the much earlier assumptions which are made during the creation of the mathematical model may also have an impact on such disagreement.

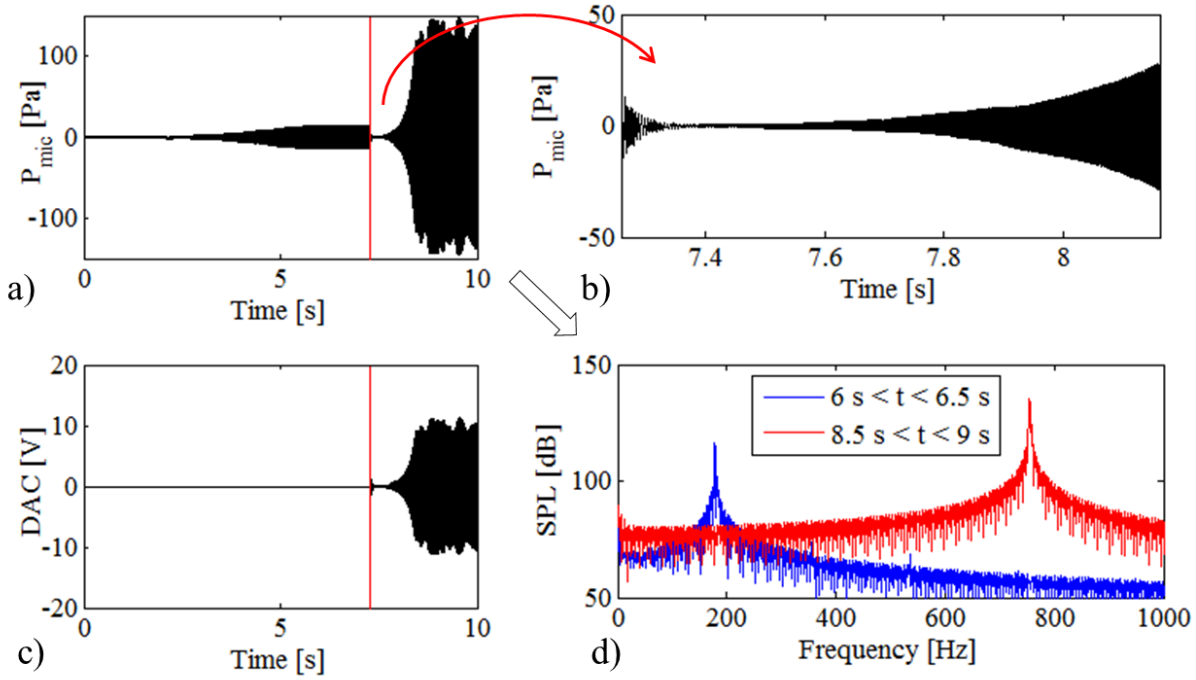

Figure 6.9 (a) Microphone recording from the experiments for point **D** in Figure 6.7a, (b) Zoomed-in view of the pressure time trace after control is turned on, (c) control signal that is sent to the DAC channel, (d) sound pressure level measurements before and after the control is turned on.

A similar comparison is made for point **D**, between Figure 6.9d and Figure 6.7b. In this case turning the control on destabilizes one higher frequency mode at $f_{ex}^{\mathbf{D}} = 754.4\,\text{Hz}$ as shown in Figure 6.9d. The corresponding frequency extracted from the model in Figure 6.7b is $f_{mod}^{\mathbf{D}} = 733.4\,\text{Hz}$. There is a much better match in this case between the experimentally measured and analytically obtained frequencies.

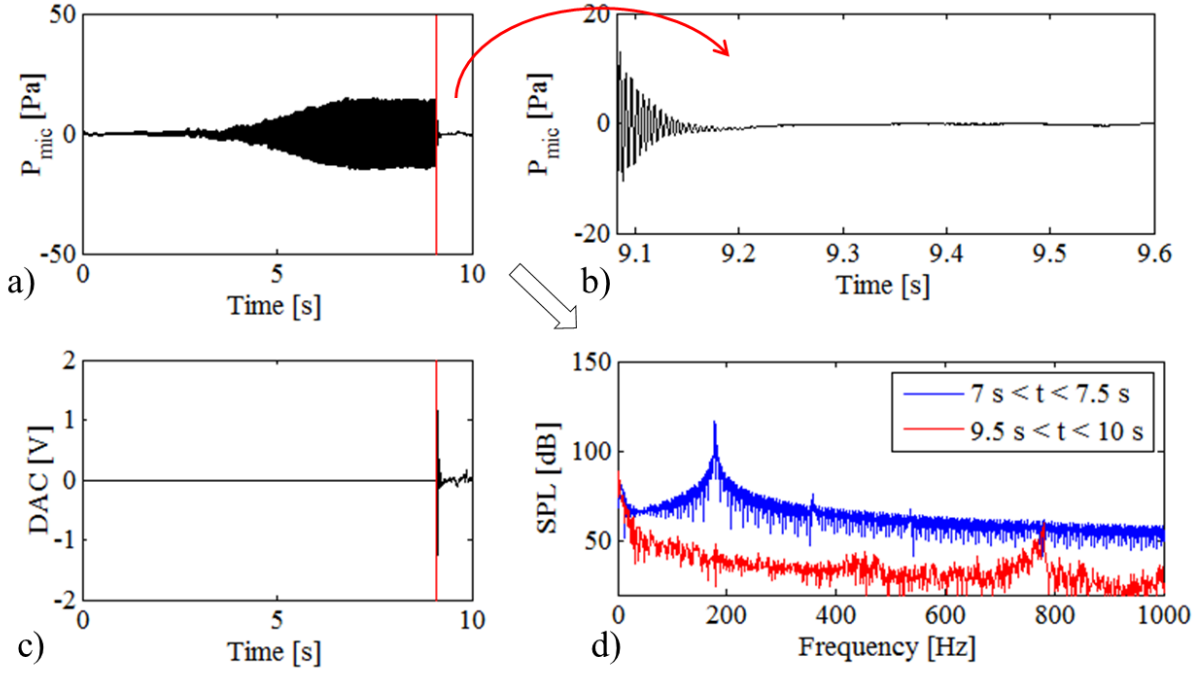

Figure 6.10 (a) Microphone recording from the experiments for point **E** in Figure 6.7a, (b) Zoomed-in view of the pressure time trace after control is turned on, (c) control signal that is sent to the DAC channel, (d) sound pressure level measurements before and after the control is turned on.

And finally at point **E**, the control action is expected to bring complete stability, and it does not excite any other dynamic modes of the system. After the control is triggered and the pressure oscillations decay in amplitude, no exponential growth is detected (see Figure 6.10a). Accordingly, there is no noticeable peak in Figure 6.10d after the control is turned on because the system is stable at all natural modes. This agrees with QPmR tableau in Figure 6.7b that the system has no characteristic roots in the right half plane, when

(K, τ_5) composition is selected at point **E**. It also agrees with the fact that point **E** lies in the region where $NU = 0$ in Figure 6.7a. Therefore this controller configuration renders a stable operation indeed, as predicted by the CTCR-generated stability map in Figure 6.7a.

Chapter 7 Conclusions and Future Work

7.1 Conclusions

This dissertation brings together two seemingly decoupled research topics: thermoacoustic instability and time delay systems. The former is almost a two century old phenomenon which is still not fully understood, whereas the latter has seen an increasing research activity in the past half-century.

A laboratory-scale thermoacoustic device, Rijke tube, is used as the test platform to study this phenomenon. Its mathematical model falls into the linear time-invariant multiple time-delayed systems class of neutral type, under certain conditions. The infinite dimensional nature of this dynamics brings a mathematical challenge to its stability analysis, which calls for the novel perspective that the current work brings.

The cluster treatment of characteristic roots paradigm, which has evolved from the time delay systems stability theory, is utilized as the main facilitating tool to address various issues in thermoacoustic instability. This paradigm's exhaustive and non-conservative stability analysis capability has led to several important contributions as summarized below:

(i) An analytical mechanism is developed to predict thermoacoustic instability in Rijke tube.

(ii) A feedback controller design strategy is proposed to stabilize an unstable operating Rijke tube.

(iii) A guideline to determine the stabilizing placements of a Helmholtz resonator on an unstable Rijke tube is presented.

(iv) A mechanism is proposed to detect control-induced instabilities in Rijke tube caused by secondary modes of the thermoacoustic dynamics.

The first contribution, prediction of thermoacoustic instability in the Rijke tube is covered in Chapter 3. An infinite dimensional mathematical model of the thermoacoustic dynamics is developed following the literature and exact stability conditions are determined in the space of Rijke tube length and heater location.

In Chapter 4, active control of thermoacoustic instability is investigated in the Rijke tube via a feedback control loop. As the second contribution, a state-space representation of the controlled system is developed from a controls perspective and a holistic feedback-controller synthesis methodology is proposed to stabilize an unstable operating Rijke tube.

Chapter 5 presents the Helmholtz resonator dynamics and its influence on thermoacoustic instability. A state space representation of the thermoacoustic dynamics in the Rijke tube with a Helmholtz resonator is derived and the stabilizing placements of the resonator along the Rijke tube are determined as the third contribution.

The final contribution, prediction of control-induced instability caused by secondary thermoacoustic modes, is covered in Chapter 6. The mathematical model of a Rijke tube platform with both a Helmholtz resonator and a feedback control loop is derived. This complex dynamic model is later utilized to detect the instabilities caused by excitation of secondary modes of the system for high controller gain selections.

All aforementioned analytical contributions are verified over an experimental Rijke tube set-up stationed in the Advanced Laboratory for Automation, Robotics and Manufacturing at the University of Connecticut.

The ultimate objective of this work is to aid the preliminary designs of thermal devices where thermoacoustic instability is a concern. The resulting contributions have been shared with the scientific community in several journal publications [52], [56], [57], [71], [73], [74] and conferences [58], [72], [75], [76], [77].

7.2 Future Work

This dissertation focuses on the thermoacoustic instability phenomenon in a Rijke tube. The validation of the proposed theories on more advanced setups; however, is essential to reach the aim of transitioning this work to real-world thermoacoustic systems such as combustors. In this regard, several improvements on the setup may lead to interesting research paths:

(i) An electrical heater is free of particularities related to complex dynamics of flames. Therefore, flame could be used as a heat source to improve the setup. More advanced heat sources can be considered resembling the single or multiple fuel injectors in modern combustors. This would open a new venue to test various active control strategies to eliminate instabilities, using adjustable fuel valves.

(ii) In the setup used, the airflow is driven by natural buoyancy and therefore has negligibly small Mach number. A blower can be used to adjust the airflow, which gives the option to test thermoacoustic instability with different Mach number flows.

(iii) Practical combustor chambers may require multiple Helmholtz resonators with various designs to prevent thermoacoustic instability. Distinct resonators mounted at different locations along the chamber would bring effects of additional multiple time delays to the system dynamics. The proposed methodology would still be applicable if a linearized system representation could be obtained.

(iv) In more advanced combustor chamber geometries, the one dimensional wave propagation assumption that forms the basis of the mathematical models derived in this study would not be valid. When this development is repeated on such structures, system models will have to be identified via either experimental tests in the chamber or computational tools.

It is vital to note that the core assumption throughout this development is that under small perturbations, the system behaves linearly. The practical combustors may be subject to abrupt changes in the pressure amplitudes due to impurities in the fuel combustion process. The thermoacoustic instabilities driven by

such events would skip the linear “onset of instability” period and thus the pressure oscillations will set to a limit cycle suddenly. The linear stability analysis that lies at the core of this study will not be helpful in such instances; instead, nonlinear stability analysis methods should be sought.

References

[1] Annaswamy, A. M., Fleifil, M. , Rumsey, J. W., Prasanth, R., Hathout, J. P. and Ghoniem, A. F., "Thermoacoustic Instability: Model-based Optimal Control Designs and Experimental Validation," IEEE Transactions on Control System Technology, Vol. 8, No. 6, 2000, pp. 905-918.

[2] Balasubramanian, K., and Sujith, R.I., "Thermoacoustic instability in a Rijke tube: Nonnormality and nonlinearity," Physics of Fluids, Vol. 20, 2008, no. 044103.

[3] Banaszuk, A., Ariyur, K. B., Krstić, M., and Jacobson, C. A., "An Adaptive Algorithm for Control of Combustion Instability," Automatica, Vol. 40, No.11, 2004, pp. 1965-1972.

[4] Bellman, R., and Cooke, K., Differential Difference Equations, Academic Press, New York, 1963.

[5] Bellows, B. D., "Characterization of Nonlinear Heat Release-Acoustic Interactions in Gas Turbine Combustors," Ph.D. Dissertation, Georgia Institute of Technology, Atlanta, 2006.

[6] Bellucci, V., Schuermans, B., Nowak, D., Flohr, P., and Paschereit, C., "Thermoacoustic Modeling of A Gas turbine Combustor Equipped with Acoustic Dampers," ASME Journal of Turbomachinery, Vol. 127, No.2, 2005, pp.372-379.

[7] Breda, D., Maset S., and Vermiglio R., "Pseudospectral Differencing Methods for Characteristic Roots of Delay Differential Equations," SIAM Journal on Scientific Computing, Vol. 27, No. 2, 2005, pp. 482-495.

[8] Campos-Delgado, U., Schuermans, B. B., Zhou, K., Paschereit, C. O., Gallestey, E. A., and Poncet, A., "Thermoacoustic Instabilities: Modeling and Control," IEEE Transactions on Control Systems Technology, Vol. 11, No. 4, 2005, pp. 429-447.

[9] Candel, S., "Combustion Dynamics and Control: Progress and Challenges," Proceedings of Combustion Institute, Vol. 29, No. 1, 2002, pp. 1-28.

[10] Cazalens, M. Roux, S. Sensiau C. and Poinsot, T., "Combustion Instability Problems Analysis for High Pressure Jet Engine Cores," Journal of Propulsion and Power, Vol. 24, No. 4, 2008, pp. 770-778.

[11] Cora, R., Martins, C.A., and Lacava, P.T., "Acoustic Instabilities Control Using Helmholtz Resonators," Applied Acoustics, Vol. 77, 2014, pp. 1-10.

[12] Culick, F.E.C., and Yang, V., "Overview of Combustion Instabilities in Liquid-propellant Rocket Engines," Liquid Rocket Engine Combustion Instability, Vol. 169, 1995, pp. 3-37.

[13] Dowling, A. P., "Nonlinear Self-Excited Oscillations of A Ducted Flame," Journal of Fluid Mechanics, Vol. 346, 1997, pp. 271-290.

[14] Dowling, A. P., and Morgans, A. S., "Feedback Control of Combustion Oscillations," Annual Review of Fluid Mechanics, Vol. 37, 2005, pp. 151–182.

[15] Dowling, A. P., and Stow, S. R., "Acoustic Analysis of Gas Turbine Combustors," Journal of Propulsion and Power, Vol. 19, No. 5, 2003, pp. 751–764.

[16] Dunstan, W. J., Bitmead, R. R., and Savaresi, S. M., "Fitting Nonlinear Low-Order Models for Combustion Instability Control," Control Engineering Practice, Vol. 9, No. 12, 2001, pp. 1301-1317.

[17] Dupère, I.D. and Dowling, A.P., "The Use of Helmholtz Resonators in A Practical Combustor," Journal of Engineering for Gas Turbines and Power, Vol. 127, 2005, pp. 268–275.

[18] Engelborghs, K., Luzyanina T., and Roose, D., "Numerical Bifurcation Analysis of Delay Differential Equations Using DDE-BIFTOOL," ACM Transactions on Mathematical Software, Vol. 28, No 1, 2002, pp. 1-21.

[19] Epperlein, J. P., Bamieh, B., and Astrom, KJ., "Thermoacoustics and The Rijke Tube," IEEE Control System Magazine, Vol. 35, No. 2, 2015, pp.57-77.

[20] Ergenc, A. F., Olgac, N., and Fazelinia, H., "Extended Kronecker Summation for Cluster Treatment of LTI Systems with Multiple Delays," SIAM Journal on Control and Optimization, Vol. 46, No. 1, 2007, pp.143-155.

[21] Evesque, S. Dowling A.P. and Annaswamy, A. M., "Self-tuning Regulators for Combustion Oscillations," Proceedings of the Royal Society A: Mathematical, Physical and Engineering Sciences, Vol. 459, 2003, pp. 1709–1749.

[22] Fazelinia, H., Sipahi, R., and Olgac, N., "Stability Robustness Analysis of Multiple Time Delayed Systems Using Building Block Concept," IEEE Transactions on Automatic Control, Vol. 52, 2007, pp. 799–810.

[23] Fleifil, M. Annaswamy, A. M., Ghoneim, Z. A. and Ghoniem, A. F., "Response of A Laminar Premixed Flame to Flow Oscillations: A Kinematic Model and Thermoacoustic Instability Results," Combustion and Flame, Vol. 106, No. 4, 1996, pp. 487-510.

[24] Fleifil, M., Hathout, J.P., Annaswamy, A.M. and Ghoniem, A.F., "The Origin of Secondary Peaks with Active Control of Thermoacoustic Instability," Combustion Science and Technology, Vol. 133, 1998, pp. 227-265.

[25] Gao, Q, Kammer A.S., Zalluhoglu, U., and Olgac, N., "Combination of Sign Inverting and Delay Scheduling Control Concepts for Multiple-Delay Dynamics," Systems and Control Letters, Vol. 77, 2015, pp. 55-62.

[26] Gelbert, G., Moeck, J. P., Paschereit, C. O. and King, R., "Feedback Control of Unstable Thermoacoustic Modes in An Annular Rijke Tube," Control Eng. Practice, Vol.20, No. 8, 2012, pp. 770-782.

[27] Gu, K. and Niculescu, S.I., "Survey on Recent Results in The Stability and Control of Time-Delay Systems," Journal of Dynamic Systems, Measurement, and Control, Vol. 125, No. 2, 2003, pp.158-165.

[28] Gu, K., and Niculescu, S. I., "Stability Analysis of Time-delay Systems: A Lyapunov Approach," Advanced Topics in Control Systems Theory, Springer London, 2006, Ch. 4, pp. 139-170.

[29] Hale J.K., and Lunel S.M.V., "Strong Stabilization of Neutral Functional Differential Equations," IMA Journal of Mathematical Control and Information, Vol. 19, 2002, pp. 5-23.

[30] Hale, J. K., and Verduyn Lunel, S. M., Applied Mathematical Sciences 99: Introduction to Functional Differential Equations, Springer, New York, 1993, pp. 11–13.

[31] Heckl, M. A., "Active Control of The Noise From a Rijke Tube," Journal of Sound and Vibration, Vol. 124, No. 1, 1988, pp. 117-133.

[32] Heckl, M.A., "Non-linear Acoustic Effects in The Rijke Tube," Acta Acustica united with Acustica, Vol. 72, 1990, pp. 63–71.

[33] Higgins, B., "On The Sound Produced by A Current of Hydrogen Passing Through A Tube," Journal of Natural Philosophy and Chemical Arts, Vol. 1, 1802, pp. 129-131.

[34] Inman, D.J., "Engineering Vibration", Upper Saddle River: Prentice Hall, 4th ed., 2013, pp. 455-470.

[35] Juniper, M.P., "Triggering in The Horizontal Rijke Tube: Non-Normality, Transient Growth and Bypass Transition," Journal of Fluid Mechanics, Vol. 667, 2011, pp. 272–308.

[36] Kim H. and Selamet, A., "Acoustic Performance of A Helmholtz Resonator with Flow," International Journal of Vehicle Noise and Vibration, Vol. 7, 2011, pp. 285-305.

[37] Kinsler, L.E., Frey, A.R., Coppens, A.B. and Sanders, J.V., "Fundamentals of Acoustics", 4th ed., John Wiley & Sons, Inc., New York, 2000, pp 284-291.

[38] Kopitz, J. and Polifke, W., "CFD-Based Application of The Nyquist Criterion to Thermo-Acoustic Instabilities," Journal of Computational Physics, Vol. 227, No. 14, 2008, pp.6754-6778.

[39] Li, X.G., Niculescu, S.I., Cela, A., "Analytic Curve Frequency-Sweeping Stability Tests for Systems with Commensurate Delays," Springer, 2015, pp. 92-93.

[40] Lord Rayleigh, J.W.S., "The Explanation of Certain Acoustical Phenomena," Nature, Vol. 18, 1878, pp. 319-321.

[41] Matveev, K. I., Culick, F.E.C., "A Study of The Transition to Instability In A Rijke Tube with Axial Temperature Gradient," Journal of Sound and Vibration, Vol. 264, 2003, pp. 689–706.

[42] McManus, K. R., Poinsot, T., and Candel, S. M., "A Review of Active Control of Combustion Instabilities," Progress in Energy and Combustion Science, Vol. 19, No. 1, 1993, pp. 1–29.

[43] Merk, H. J. "An Analysis of Unstable Combustion of Premixed Gases." In Symposium (International) on Combustion, Vol. 6, No. 1, 1957, pp. 500-512.

[44] Michiels, W., Engelborghs, K., Roose, D. and Dochain D., "Sensitivity to Infinitesimal Delays in Neutral Equations," SIAM Journal on Control and Optimization, Vol. 40, No. 4, 2002, pp. 1134–1158.

[45] Morgans, A.S. and Annaswamy, A.M., "Adaptive Control of Combustion Instabilities for Combustion Systems with Right-Half Plane Zeros," Combustion Science and Technology, Vol. 180, No. 9, 2008, pp.1549-1571.

[46] Nicoud, F., and Poinsot, T., "Thermoacoustic Instabilities: Should the Rayleigh Criterion Be Extended to Include Entropy Changes?," Combustion and Flame, Vol. 142, 2005, pp. 153-159.

[47] Niculescu, S. I., "Delay Effects on Stability: A Robust Control Approach," Berlin, 2001.

[48] Ogata, K., State Space Analysis of Control Systems, Prentice Hall, Englewood Cliffs, New Jersey, 1967, pp. 16-24.

[49] Olgac N., and Sipahi, R. "The Cluster Treatment of Characteristic Roots and the Neutral Type Time-delayed Systems," Journal of Dynamic Systems, Measurement and Control, Vol. 127, No. 1, 2005, pp. 88-97.

[50] Olgac, N. and Holm-Hansen, B.T., "A Novel Active Vibration Absorption Technique: Delayed Resonator," Journal of Sound and Vibration, Vol. 176, No. 1, 1994, pp. 93-104.

[51] Olgac, N., and Hosek, M. "A New Perspective and Analysis for Regenerative Machine Tool Chatter," International Journal of Machine Tools and Manufacture," Vol. 38, No. 7, 1998, pp. 783-798.

[52] Olgac, N., Cepeda-Gomez, R., Zalluhoglu, U., Kammer, A.S., "Parametric Investigation of Thermoacoustic Instability (TAI) in A Rijke Tube: A Time-Delay Perspective," International Journal of Spray and Combustion Dynamics, Vol. 7, No. 1, 2015, pp. 39-68.

[53] Olgac, N., Ergenc, A. F. and Sipahi, R., "Delay Scheduling: A New Concept for Stabilization in Multiple Delay Systems," Journal of Vibration and Control, Vol. 11, No. 9, 2004, pp. 1159-1172.

[54] Olgac, N., Vyhlídal, T., and Sipahi, R., "A New Perspective in The Stability Assessment of Neutral Systems with Multiple and Cross-talking Delays," SIAM Journal on Control and Optimization, Vol. 47, No.1, 2008, pp. 327-344.

[55] Olgac, N., Zalluhoglu, U. and Kammer, A.S., "On Blade/Casing Rub Problems in Turbomachinery: An Efficient Delayed Differential Equation Approach," Journal of Sound and Vibration, Vol. 333, No. 24, 2014, pp.6662-6675.

[56] Olgac, N., Zalluhoglu, U., Kammer, A.S., "A New Perspective in Designing Delayed Feedback Control for Thermoacoustic Instabilities (TAI)," Combustion Science and Technology, Vol. 187, No. 5, 2015, pp. 697-720.

[57] Olgac, N., Zalluhoglu, U., Kammer, A.S., "Predicting Thermoacoustic Instability: A Novel Analytical Approach and Its Experimental Validation," Journal of Propulsion and Power, Vol. 30, No. 4, 2014, pp. 1005-1015.

[58] Olgac, N., Zalluhoglu, U., Kammer, A.S., "Stability and Control of a Thermoacoustic Device: The Rijke's Tube," ASME 2014 Dynamic Systems and Control Conference, (pp. V002T33A001-V002T33A001), American Society of Mechanical Engineers, 2014.

[59] Poinsot, T., and Veynante, D., "Flame/Acoustics Interactions," Theoretical and Numerical Combustion, 2nd ed., R.T. Edwards, Philadelphia, 2005, pp. 327–355.

[60] Raun, R. L., Beckstead, M. W., Finlinson, J. C., and Brooks, K. P.,"A Review of Rijke Tubes, Rijke Burners and Related Devices," Progress in Energy Combustion Science, Vol. 19, No. 4, 1993, pp. 313–364.

[61] Richard, J.P., "Time-Delay Systems: An Overview of Some Recent Advances and Open Problems," Automatica, Vol. 39, 2003, 1667–1694.

[62] Rijke, P. L., "Notiz Uber Eine Neue Art, Die In Einer An Beiden Enden Offenen Röhre Enthaltene Luft In Schwingungen Zu Versetzen (Note Regarding A New Way of Generating Vibrations in The Air Contained in A Tube Open at Both Ends)," Annalen der Physik und Chemie, Vol. 107, 1859, pp. 339-343.

[63] Selimefendigil, F. Sujith R. I. and Polifke, W., “Identification of Heat Transfer Dynamics for Non-Modal Analysis of Thermoacoustic Stability,” Applied Mathematics and Computation, Vol. 217, 2011, pp. 5134–5150.

[64] Sipahi, R., and Olgac, N., “A Unique Methodology for the Stability Robustness of Multiple Time Delay Systems,” Systems and Control Letters, Vol. 55, No. 10, 2006, pp. 819-825.

[65] Subramanian, P. Mariappan, S. Sujith, R.I. Wahi, P., “Bifurcation Analysis of Thermoacoustic Instability in A Horizontal Rijke Tube,” International Journal of Spray and Combustion Dynamics, Vol. 2, 2010, pp. 325–356.

[66] Swift, G. W., “Analysis and Performance of A Large Thermoacoustic Engine,” The Journal of the Acoustical Society of America, Vol. 92, No. 3, 1992, pp. 1551-1563.

[67] Tariq, S., and Annaswamy, A. M., "Control of Combustion Instability,” The Impact of Control Technology, IEEE Control Systems Society, 2011.

[68] Verriest, E.I. Michiels, W., “Inverse Routh Table Construction and Stability Of Delay Equations,” Systems and Control Letters, Vol. 55, No. 9, 2006, pp. 711–718.

[69] Vyhlídal, T., and Zitek, P.,“Mapping Based Algorithm for Large Scale Computation of Quasi-Polynomial Zeros,” IEEE Transactions on Automatic Control, Vol. 54, No. 1, 2009, pp. 171–177.

[70] Wang, X. and Mak, C-M., “Wave Propagation in A Duct With A Periodic Helmholtz Resonators Array,” Journal of Acoustical Society of America, Vol. 131, 2012, pp. 1172-1182.

[71] Zalluhoglu, U., Kammer, A.S., Olgac, N., “Delayed Feedback Control Laws for Rijke Tube Thermo-Acoustic Instability, Synthesis and Experimental Validation,” IEEE Transactions on Control Systems Technology, accessed January 14, 2016 (in press). doi:10.1109/TCST.2015.2512938

[72] Zalluhoglu, U., Kammer, A.S., Olgac, N., “Feedback Stabilization of A Thermoacoustic Device with Experiments,” American Control Conference (ACC), IEEE, 2015.

[73] Zalluhoglu, U., Olgac, N., "A Study of Helmholtz Resonators to Stabilize Thermoacoustically Driven Pressure Oscillations," Journal of the Acoustical Society of America, vol. 139, no. 4, pp. 1962-1973, 2016.

[74] Zalluhoglu, U., Olgac, N., "Deployment of Time-delayed Integral Control for Suppressing Thermoacoustic Instabilities," Journal of Guidance, Control and Dynamics, accessed September 23, 2015 (in press). doi:10.2514/1.G001362

[75] Zalluhoglu, U., Olgac, N., "Passive Suppression of Thermoacoustic Instability in A Rijke Tube," 13th IFAC Workshop on Time Delay Systems, 2016 (to be presented).

[76] Zalluhoglu, U., Olgac, N., "Placement of Helmholtz Resonators in Series for Passive Control of Thermoacoustic Instabilities from a Time-Delay Perspective," American Control Conference (ACC), 2016, IEEE (to be presented).

[77] Zalluhoglu, U., Olgac, N., "Thermo-acoustic Instability: Theory and Experiments," IFAC-PapersOnLine, Vol. 48, No., 12, 2015, pp. 75-80.

[78] Zhao D., Li J., "Feedback Control of Combustion Instabilities Using a Helmholtz Resonator with an Oscillating Volume," Combustion Science and Technology, Vol. 184, No. 5, 2012, pp. 694-716.

[79] Zhao, D., and Li. X.Y., "A Review of Acoustic Dampers Applied to Combustion Chambers in Aerospace Industry," Progress in Aerospace Sciences, Vol. 74, 2015, pp.114-130.

[80] Zhao, D., Morgans, A.S., "Tuned Passive Control of Combustion Instabilities Using Multiple Helmholtz Resonators," Journal of Sound Vibration, Vol. 320, No. 4, 2009, pp. 744-757.

[81] Zinn, B.T., "Combustion Instabilities: Problems, Solutions, and Research Needs," Chemical and Physical Processes in Combustion: 1986 Fall Technical Meeting. Combustion Institute, Pittsburgh, PA, USA, San Juan Bautista, PR, 1987, pp. 1-12.